ABSTRACT

Title of Thesis: TEMPERATURE MAPPING OF AN ACOUSTICALLY FORCED LAMINAR DIFFUSION FLAME USING PLANAR LASER RAYLEIGH SCATTERING

Degree Candidate: Ezra Faith Chen

Degree and year: Master of Science, 2005

Thesis directed by: Assistant Professor Steven G. Buckley
Department of Mechanical Engineering

Excitation of a combusting flow near its preferred mode to increase volumetric energy release has been studied for many years on internal systems. Excitation promotes the production and propagation of large scale vortices, which have been shown to improve combustion. Forcing on external systems is far less documented. Most studies employ chemiluminescence and Schlieren to image the flow, however neither technique provides a true cross sectional measurement.

Planar laser Rayleigh scattering was used to generate temperature maps of an acoustically forced laminar jet. Small scale enhancement was found to increase with frequency, while large scale vortices had competing effects in the range of the preferred mode. While vortices compacted the flame, increased the residence time of reactants, and entrained fresh reactants, straining of the reaction region and cooling from the entrained gases kept the temperature of the flame close to the unforced flame temperature.

TEMPERATURE MAPPING OF AN ACOUSTICALLY FORCED LAMINAR DIFFUSION FLAME USING RAYLEIGH SCATTERING

By

Ezra Faith Chen

Thesis submitted to the Faculty of the Graduate School of the
University of Maryland, College Park in partial fulfillment
of the requirements for the degree of
Master of Science
2005

Advisory Committee

Assistant Professor Steven G. Buckley, Chair/Advisor
Associate Professor Kenneth Yu, Co-Chair
Assistant Professor Christopher Cadou

ACKNOWLEDGEMENTS

I would like to thank my advisor, Dr. Steven G. Buckley, for providing guidance and invaluable knowledge throughout my research. I would like to thank Dr. Ken Yu who generously provided lab space, time, supplies, and equipment as well as advice in Dr. Buckley's absence. Also, thanks to Dr. Christopher Cadou for volunteering his time to sit on this committee.

I am indebted to the Mechanical Engineering graduate office faculty for without whom I would not have been able to complete my research. I must acknowledge the members of the Advanced Propulsion Lab and Fire Engineering and Thermal Sciences Lab for their support through providing their insight and smart-aleck humor, making this research experience an enjoyable one.

I would like to thank my family for their unwavering faith in me. Finally, I would to thank Allice, my source of inspiration and sometimes distraction.

Table of Contents

List of Figures vi

List of Tables viii

List of Equations ix

Table of Nomenclature x

CHAPTER 1 Introduction 1

1.1 Background 1

1.2 Combustion Control 1

1.3 Schlieren and Chemiluminescence 2

1.3.1 Common Laser Diagnostics 4

1.4 Objective 5

CHAPTER 2 Literature Review 7

2.1 Vorticity and Combustion 7

2.2 Flame Acoustic Coupling 12

2.3 Rayleigh Scattering 15

2.3.1 Basic Principle 16

2.3.2 Index of Refraction 18

2.3.3 Advantages of Rayleigh Scattering 19

2.3.4 Disadvantages of Rayleigh Scattering 19

2.4 Rayleigh Imaging 20

CHAPTER 3 Setup and Data Reduction 23

3.1 Combustor 23

3.2 Laser and Camera 25

3.3 Flow Forcing 26

3.4 Flow Control 27
3.5 Calibration Images 28
3.6 Data Reduction 29
3.7 Matlab Program 30
CHAPTER 4 Data and Analysis 33
4.1 Test Conditions 33
4.2 Data 35
4.2.1 General Comments 35
4.3 Flow condition 1&2 Velocity Ratio, V_r=1 39
4.3.1 Flow condition 1, U_{inner} = 1.36 m/s, Velocity Ratio=1 39
4.3.2 Flow Condition 2, Velocity U_{inner}=2.16 m/s, Velocity Ratio=1 48
4.4 Flow Condition 3, Velocity Ratio V_r=2 57
4.5 Flow Condition Four, Velocity Ratio V_r=0.5 64
4.6 Error 71
CHAPTER 5 Conclusion 77

Appendix A- Flame and Rayleigh Scattering Images 80

Appendix B- Temperature Maps 80

Appendix B.1 Flow Condition 1: Vr=1, U_{inner}=1.36 m/s 86

Appendix B.2 Flow Condition 2: Vr=1, Uinner=2.16 m/s 91

Appendix B.3 Flow Condition 3: Vr=2, Uinner=1.36 m/s 96

Appendix B.4 Flow Condition 4: Vr=0.5, Uinner=1.36 m/s 101

Appendix C- MathCad Code 106

Appendix D-Matlab Code 110

Appendix E: Pixel Replacement Percentages 114

References 116

List of Figures

Figure 2-1 Development of vortices[18] 8

Figure 2-2 Vortex growth and pairing. An absence of pairing (I), pairing and entrainment (II &III) and preparation for roll-up (IV) are imaged. Note that f_{mjet} is the mixed jet fluid fraction. [19] 9

Figure 2-3 Self-induced instability mechanism for an external system[36] 14

Figure 3-1 Diagram and picture of the combustor 24

Figure 3-2 Schematic of phase-locking scheme 27

Figure 3-3 PLRS, fifty shot average, of helium jet (left) and air jet (right) 28

Figure 3-4 Dust replacement in ambient condition image 31

Figure 3-5 Dust replacement for all other images 32

Figure 4-1 PLRS in relation to flame 34

Figure 4-2 Unforced temperature maps for flow condition 1 (top left), 2 (top right), 3 (bottom left), and 4 (bottom right) 36

Figure 4-3 Progression of flame shape through forcing range 37

Figure 4-4 Flow condition 1 temperature maps and midline plot, 150 Hz 39

Figure 4-5 Flow condition 1 temperature maps and midline plot, 180 Hz 40

Figure 4-6 Flow condition 1 temperature maps and midline plot, 200 Hz 41

Figure 4-7 Flow condition 1 temperature maps and midline plot, 230 Hz 42

Figure 4-8 Flow condition 1 temperature maps and midline plot, 250 Hz 44

Figure 4-9 Flow condition 1 temperature maps and midline plot, 270 Hz 45

Figure 4-10 Flow condition 1 temperature maps and midline plot, 300 Hz 46

Figure 4-11 Flow condition 1 temperature maps and midline plot, 320 Hz 47

Figure 4-12 Flow condition 1 temperature maps and midline plot, 350 Hz 48
Figure 4-13 Flow condition 2 temperature maps and midline plot, 150 Hz 49
Figure 4-14 Flow condition 2 temperature maps and midline plot, 180 Hz 50
Figure 4-15 Flow condition 2 temperature maps and midline plot, 200 Hz 51
Figure 4-16 Flow condition 2 temperature maps and midline plot, 230 Hz 53
Figure 4-17 Flow condition 2 temperature maps and midline plot, 250 Hz 54
Figure 4-18 Flow condition 2 temperature maps and midline plot, 270 Hz 55
Figure 4-19 Flow condition 2 temperature maps and midline plot, 300 Hz & 320 Hz 56
Figure 4-20 Flow condition 2 temperature maps and midline plot, 350 Hz 57
Figure 4-21 Flow condition 3 temperature maps and midline plot, 150 Hz 58
Figure 4-22 Flow condition 3 temperature maps and midline plot, 180 Hz 59
Figure 4-23 Flow condition 3 temperature maps and midline plot, 200 Hz 60
Figure 4-24 Flow condition 3 temperature maps and midline plot: 230 Hz & 250 Hz 61
Figure 4-25 Flow condition 3 temperature maps and midline plot: 270 Hz & 300 Hz 62
Figure 4-26 Flow condition 3 temperature maps and midline plot, 320 Hz 63
Figure 4-27 Flow condition 3 temperature maps and midline plot, 350 Hz 64
Figure 4-28 Flow condition 4 temperature maps and midline plot, 150 Hz 65
Figure 4-29 Self-induced flame instability for flow condition 4 66
Figure 4-30 Flow condition 4 temperature maps and midline plot, 180 Hz 66
Figure 4-31 Flow condition 4 temperature maps and midline plot, 200 Hz 67
Figure 4-32 Flow condition 4 temperature maps and midline plot, 230 Hz & 250 Hz 68
Figure 4-33 Flow condition 4 temperature maps and midline plot, 270 Hz & 300 Hz 69
Figure 4-34 Flow condition 4 temperature maps and midline plot, 320 Hz & 350 Hz 70

Figure 4-35 Response curve for a pixel with error bounds 74

Figure 4-36 Sample of standard error images 75

List of Tables

Table 3-1 Cross sections of gases used 23

Table 4-1 Flow conditions 33

Table 4-2 Experiment frequency range and Strouhal numbers 33

List of Equations

Equation 2.1 Rayleigh cross section of a gas 16

Equation 2.2 Rayleigh cross section at 90^{o} viewing 17

Equation 2.3 Rayleigh cross section for gas mixture 17

Equation 2.4 Scattering intensity 17

Equation 2.5 Scattering intensity for binary mixture 17

Equation 2.6 Molar refractivity 18

Equation 2.7 Molar refractivity of gas mixture 18

Equation 2.8 Index of refraction as a function of molar refractivity 18

Equation 3.1 Instantaneous total intensity 29

Equation 3.2 Average total intensity 29

Equation 3.3 Average Rayleigh signal to average Rayleigh ambient signal ratio 29

Equation 3.4 Equation 3.3 with the perfect gas law and Rayleigh scattering intensity substituted in 30

Equation 3.5 Temperature as a function of total intensity 30

Equation 4.1 Strouhal number 33

Table of Nomenclature

Symbols

A_o	Avegodro's number
α	Depolarization ratio
C	Calibration constant
D_o	Outer diameter
I	Intensity
λ	Wavelength
n	Index of refraction
N	Molecular number density
N_o	Loschmidt's number
P	Pressure
φ	Equivalence ratio
R	Universal gas constant
ρ	Molar density
R_l	Molar refractivity
σ	Rayleigh cross-section
T	Temperature
θ	Incident angle
u	Velocity
Vr	Velocity ratio
X	Mole fraction

Subscripts

a	Air
amb	Ambient
b	Background
f	Fuel
i	Species
inner	Inner jet
n	Noise
o	Incident
r	Rayleigh
t	Total
outer	Outer jet

CHAPTER 1 Introduction

1.1 Background

Increasing the volumetric energy release and stability of a combustion system is often the main goal of combustion control. There are several benefits of controlling combustion, including reductions in potentially damaging pressure fluctuations and extension of the combustor's operating envelope as the flammability limits and flame stability increases. There are a number of ways to enhance combustion. One method of particular interest is acoustically forcing a combusting flow at its natural, or preferred, frequency, which promotes the production and propagation of vortices. The effects of vortex generation on mixing and combustion have been the topic of many studies.

Groups studying the relationship between heat release and vortical structures typically use Schlieren imaging and chemiluminescence as the flame diagnostic. Schlieren imaging is based on the refraction of light in a flow containing a density gradient and is generally used to study flame structure. Chemiluminescence is based on the emission from the excited products of a reaction. From the intensity of the signal, a heat release rate can be inferred. Although both methods are simple and convenient to implement, both techniques are volume averaged methods, lacking the spatial resolution that is of interest in this research.

1.2 Combustion Control

Combustor control methods can be classified into two categories, active or passive. Passive control mechanisms, which are related to the geometry of the combustor and do not have an actuating or dynamic component, although passive control

components may alter time-dependent flow processes [1]. Passive control methods include flame holders, mixing cavities, and unconventional inlet shapes for the fuel and air [2]. For example, jets from elliptical openings with small aspect ratios will entrain up to eight times more fluid from the surrounding fluid than a circular jet. This increased entrainment is the product of a flow induction process the results from the higher vortex spread the minor axis of an ellipse compared to its major axis [3].

Passive control methods have been shown to be very effective; however, they are limited to specific operating conditions and geometry. To extend the effectiveness of passive control or to enhance mixing where passive control is not useful, such as in some high intensity devices such as gas turbines or rocket engines, active methods may need to be used [3]. Active control requires some sort of actuator as a dynamic component [1]. In the case of the experiment described in this thesis, a trumpet speaker is the actuator. Several previous studies have used a speaker as a means of forcing the flow, and other studies have used a secondary pulsating gas flow controlled with a rotating valve. Another means of active control is injecting a secondary, stabilizing, fuel at specific locations and times, a strategy that is currently an active area of research [4]. A detailed review of active control, including closed loop control, is found in [1].

1.3 Schlieren and Chemiluminescence

Schlieren is a simple method of imaging using the refraction of light through density gradients of the flow and a knife edge placed near the focal point of the lens. The knife-edge blocks some of the light, while preferentially allowing through other portions of light which have been refracted by the density gradient of the flow. This creates a light and dark field that can be recorded with a camera. This imaging technique has been

used to study laminar [5, 6], and turbulent [4, 7-9] flame structure as far back as 1956 [10]. However, it is difficult to determine the contribution of density to refraction since refraction is a volumetric effect. Also, Schlieren imaging requires a density change, otherwise only a gray field is seen. However, Schlieren has been used as a means to determine mean flame area in [11].

Chemiluminescence is the emission of light from the excited products of a reaction. The intensity of the light is a measure of the reaction rate, and in combustion systems, this reflects the amount of heat release. The chemiluminescent intensity as a function of wavelength reveals emission from specific excited flame species. This method can be used for locating reacting regions as certain radicals appear exclusively in these regions, for example, CH, C_2, and OH radicals, commonly imaged in combustion studies [4, 11-14]. However, chemiluminescence is also volume integrated imaging method, cannot capture fine structures, and requires long integration times, on the order of 100 μs [13]. In addition, within the volume, other molecules of the same radical can absorb the emitted light, and such self-absorption limits the ability of chemiluminescence to be quantitative. Furthermore, other radicals may have overlapping wavelengths with species being detected. Chemiluminescence can be a quantitative measure of heat release or equivalence ratio if a calibration experiment is run on the particular burner. Efforts to generate non-specific correlations between chemiluminescence, heat release, and equivalency are being pursued [14, 15].

Laser diagnostic techniques are well-suited for making quantitative measurements and have been implemented in reacting and non-reacting flow analysis for a long time. They share the same non-intrusive advantage as Schlieren and chemiluminescence,

avoiding many of the problems associated with perturbing the flow by the introduction of a sensor probe. Many scattering techniques can acquire data from a planar field, as cylindrical lenses can be used to make a laser sheet that can be imaged by an intensified charge coupled device (ICCD). A planar laser setup can provide true spatially resolved two-dimensional measurements. Such full field measurements can capture fluid structures that point measurements cannot. One drawback is that laser scattering methods do require optical access into the system, which may not always be feasible.

1.3.1 Common Laser Diagnostics

Laser diagnostic techniques include Rayleigh, Raman, laser-induced fluorescence (LIF), and laser induced breakdown spectroscopy (LIBS), among many methods. The focus of this project is to use planar laser Rayleigh scattering to image an acoustically forced flame. The image can be recorded on an ICCD and then be converted in to a temperature map. Rayleigh scattering techniques have been used for some time in flow diagnostics, measuring temperature, density, and composition. The simplicity of implementation and the strength of the signal, in addition to the non-intrusive character of the method, make Rayleigh scattering a strong candidate when considering a method to analyze a flow. Of all the laser diagnostic methods, Rayleigh is the simplest and can provide a high signal to noise ratio. More detail about Rayleigh scattering will be presented later.

In LIBS, a laser is focused to a point creating a plasma spark. Molecules within the spark break down into associated elements, which are thermally excited and emit element-specific spectra when the electrons relax. This method is useful for point-wise elemental composition measurements. However, this method cannot be implemented in a

planar arrangement. LIBS can perturb a flow as the result of the shock wave generated by the spark. The spark could also ignite flammable mixtures of gases.

LIF involves tuning the incident laser to a resonant wavelength corresponding to a particular electron transition of the species being measured. The incident laser light is absorbed by the species and a fraction of the atoms or molecules are excited. Following excitation, either resonant or nonresonant light can be measured as the species relaxes. This method can be implemented in a planar form, which is advantageous. The signal can be difficult to analyze, however, the interpretation of LIF signal is complicated by the effect of quenching which is dependent on the species concentration and temperature field [16].

Raman scattering comes from the inelastic collision of incident photons with the species in the measurement volume. The resulting scattering is species-specific and is resistant to background noise. Raman signal seems ideal for imaging mixed gas flow, however, Raman scattering is very weak; Rayleigh scattering is two to three orders stronger than Raman scattering [17]. Consequently, Raman imaging requires very high powered lasers, operation in the ultraviolet frequency range, or long integration times [16].

1.4 Objective

A planar laser Rayleigh scattering (PLRS) setup was implemented on an acoustically forced annular diffusion flame to quantify the effects of forcing and vorticity on combustion. The arrangement is a coaxial flow of fuel as the center jet and air as the surrounding flow. The fuel has been chosen so the intensity of the Rayleigh signal is directly proportional to the inverse of the temperature. The experiments described

include variation of the frequency of the forcing, variation of the velocity ratio of the inner and outer flow, and variation of the absolute velocity of the jets.

CHAPTER 2 Literature Review

Most combustion studies involving flow forcing and instability analysis are on turbulent enclosed systems. External or unbounded systems are much less well documented, perhaps due to fewer practical applications of such systems. The production and interaction of vortices and their effect on combustion will be discussed in this section. A summary of acoustic flame coupling will follow.

Rayleigh scattering has been used in gas flow studies for some time, so many implementation schemes and data reduction methods have been well documented. Methods of implementation and quantification of Rayleigh scattering will be discussed in detail. The new trend is implementing multiple laser diagnostic techniques to simultaneously measure flow characteristics, allowing detailed analysis of more complicated systems [16].

2.1 Vorticity and Combustion

Forcing the gas flow at specific frequencies is of particular interest as vortex formation can be controlled. If a flow is excited in a certain frequency range, the formation of small vortices, due to hydrodynamic instabilities of the shear layer, is promoted in the initial portions of the shear layer at the frequency of the forcing. The small vortices then coalesce into a larger vortex; quickly reaching a limiting size, maximizing jet spread, which is the ratio of the jet half width to axial distance, and propagate downstream in a highly coherent manner at a frequency equal to the forcing frequency [9, 11]. Since the fluid features of the flow field control vortex formation, it is

expected that the flow is most sensitive to excitation close to the preferred mode of the field [2, 9].

The mechanism for initiation and growth of vortices was proposed by Winant et al [18]. For a mechanically forced flow, ~~a~~ small amplitude waves begin in the early regions of the mixing layer at the same frequency of the forcing. The wave distorts the boundaries of a constant vorticity layer, Figure 2-1a. This distortion causes a cross-stream velocity component, causing the perturbation to grow and the shear layer to distort into thick and thin regions, Figure 2-1b-c. The thick regions pinch off into discrete vortices, propagate downstream, and possibly combine with other vortices, Figure 2-1d. During vortex pairing, irrotational fluid in between the vortices becomes entrained as vortex cores rotate around each other and homogenization of the mixing fluids occurs.

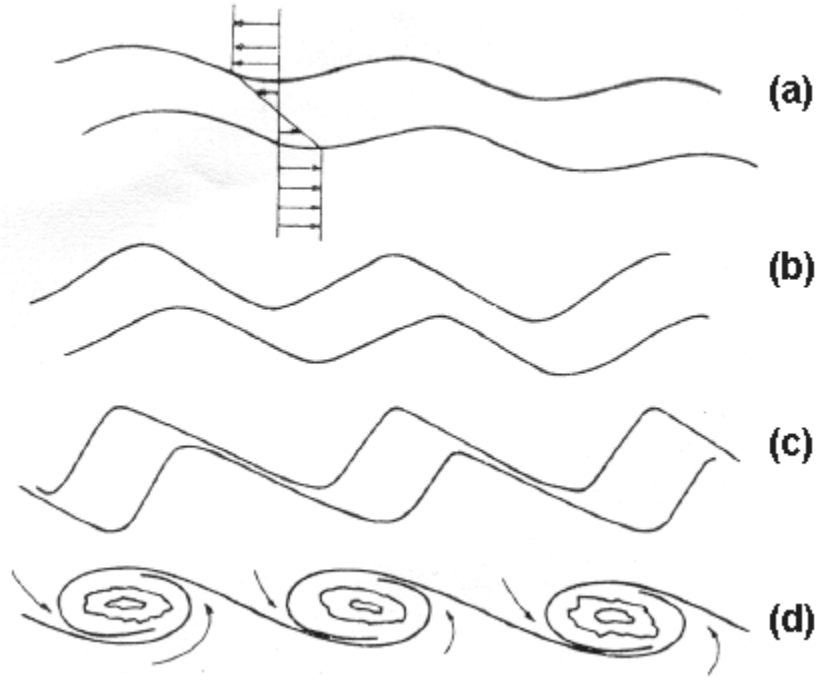

Figure 2-1 Development of vortices[18]

Using a N_2-Air coaxial jet imaged by LIF, detailed images of vortex growth, interaction, entrainment of surrounding fluid, and molecular mixing within the vortices

were taken in high spatial and temporal resolution by Meyer et al. [19] for a coaxial flow responding to a single pulse, shown in Figure 2-2.

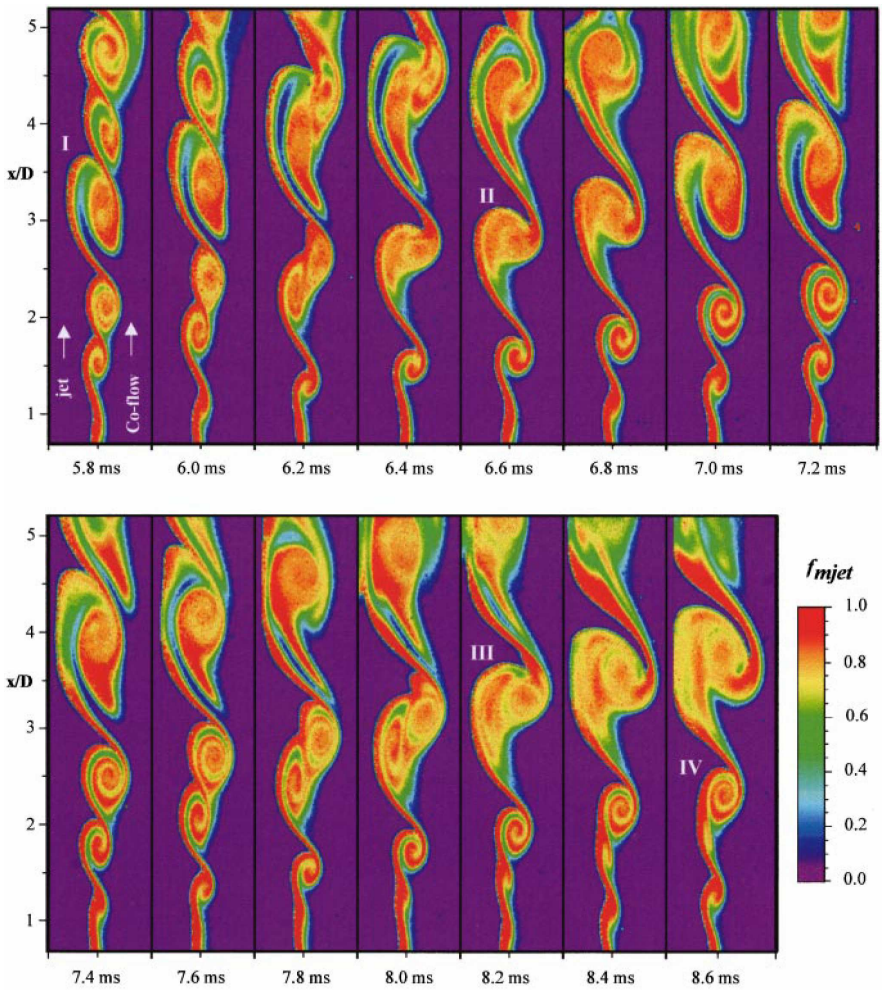

Figure 2-2 Vortex growth and pairing. An absence of pairing (I), pairing and entrainment (II &III) and preparation for roll-up (IV) are imaged. Note that f_{mjet} is the mixed jet fluid fraction. [19]

The data clearly shows the development of a small amplitude disturbance, seen at the very bottom of the frame labeled 5.8 ms, into a vortex that is almost entirely mixed. The rotation of pairing vortices about their mutual center is shown and mixing layers are further homogenized as the vortices move downstream. Further entrainment of the coflow can be seen as vortices interact, from 6.4 ms to 7.2 ms and 8.2 ms to 8.6 ms. The absence of vortex pairing at 5.8 ms was also observed by Winant.

It can be concluded from the above images that for a diffusion flame, flow forcing generates large regions of well-mixed fluid suitable for combustion. Vortices will entrain fuel and air into the reaction products as well [9]. Vortices increase the residence time of the fuel in the flame, as they continue to entrain reactants as they advect downstream. The presence of vortices also convolutes the flame, causing a larger flame area. In light turbulence, when the relative fluctuating velocity, u'/u, is small, this results in a higher fuel consumption rate and hence increased power density. Moreover, the flame length can be significantly reduced and combustion intensity increases as reactants are consumed at a higher rate due to the improved entrainment and larger reaction zone [2]. Baroclinic mechanisms that result from the flame can work to distort the vortex structure [20].

When the amplitude of the forcing is increased, the resulting vortices are stronger and would typically entrain more reactants and enhance combustion [9]. The effect of increasing the frequency is not as straightforward. Increasing the forcing frequency may increase the generation rate of vortices, entrain reactants more frequently, and consequently improve combustion. However, increasing the forcing frequency could cause vortices to stabilize at smaller diameters that do not coalesce in to larger structures [3]. These small vortices may not provide the necessary bulk mixing.

When the velocity of the flow is changed, the propagation speed of the vortex is changed, as well as its wavelength [9]. In addition, the ratio of the velocity fluctuation imposed by the disturbance to the mean flow velocity will change, unless the forcing amplitude is changed accordingly. Data indicates that increasing flow, without changing the forcing amplitude, decreases combustor efficiency.

Numerous experiments have investigated flame-vortex interactions [2, 9, 21-24] and many numerical and analytical studies have been performed as well [24-28]. A review summarizing many of the flame-vortex studies has been written [29].

A parametric study of the effects of changing the Strouhal, Equation 4-1 , and Damköhler number, as well as the Reynolds number, was performed on a turbulent premixed propane air flame at the University of Maryland [4]. The goal of the project was to identify the temporal and spatial location of heat release relative to vortical structures and to determine the timing and location for a secondary injection of fuel for active combustor control. To determine these properties, CH* chemiluminescence images were superimposed onto Schlieren images. Results showed little effect on flame structure or heat release locations due to changing the Reynolds number. Changing the Strouhal number changed the size and strength of the vortices, but not the location of heat release. Changing the Damköhler number had the greatest effect on heat release patterns. At Damköhler numbers Da>6, when the reaction time scale is much smaller then the flow time scale, heat release closely followed the vortex. At Damköhler numbers close to one, heat release no longer coincides with the vortex, possibly from excessive flame stretch by the vortices causing quenching.

An open turbulent coaxial jet of air and fuel, each forced at separate frequencies, was investigated by Gutmark et al [2]. The combustor was a diffusion flame setup using air as the center jet and fuel as the outer jet. The main objective of this study was to improve combustion by forcing the flow such that combustion would take place as near to the flame holder as possible, even possibly delaying vortex coalescence, and producing a wider and more uniform reaction zone while minimizing flame-acoustic coupling. The

air jet was forced using a speaker at Strouhal number St=0.49, Equation 4-1, based on jet diameter, which was found to have the greatest effect on the airflow. The fuel was forced at a higher harmonic to trigger and amplify initial instabilities in order generate fine scale turbulence for enhanced molecular mixing needed for combustion close to the burner. PLIF was employed to image OH concentrations, which was used to find regions of combustion and product gases. Analysis of the OH images revealed that a Strouhal number St=3.91 in the fuel flow generated the greatest uniformity over the reaction zone. It was also found that if the fuel excitation amplitude was decreased to 30% of the St=3.91 case, but forcing frequency was increased to St=5.87, flame height was significantly shortened as the flame was able to fully burn the fuel very quickly.

2.2 Flame Acoustic Coupling

The main instability mechanism in many combustors can be attributed to flame acoustic coupling. Combustion instability is manifested as pressure fluctuations. RMS pressure fluctuations can be easily measured and are used as a measure of combustion instability. [11]. Pressure fluctuations induce velocity fluctuations, which form vortices. In unforced combustion, the vortices form and shed at the acoustic modes of the combustor, which cause local increases in heat release in the vortices due to local enhanced mixing. If a pressure pulse arrives or is present at the location of a local thermal expansion due to the local heat release, the pressure pulse is reflected at a greater amplitude [30]. This is known as the Rayleigh criterion for thermoacoustic instability. When the unsteady heat release is not in phase with the pressure oscillation, a damping effect occurs. Hydrodynamic and intrinsic instabilities are also contributing factors. The

coupling between these instability sources makes the attribution of the source of instability sometimes very difficult [1].

A numerical study of the interaction of a planar premixed flame with an acoustic wave was performed by Lieuwen [31]. The processes that drive or damp acoustic waves citied in the study:

- Wrinkling of the flame due to velocity fluctuations accompanying the acoustic wave
- Fluctuations the flame local consumption rate
- Reflection and refraction of the waves due to sudden temperature changes and acoustic impedance from gasses
- Superposition of incident and scattered acoustic waves
- Vorticity production through the baroclinic mechanism
- Intrinsic flame instabilities

Complex behavior of the superposition of the acoustic wave with the convected vorticity wave was numerically calculated, and it was determined that at certain incident angles of the acoustic wave to the flame front, the acoustic wave is damped as energy is transferred from the acoustic wave to the excitation of vorticity. At other angles, acoustic energy is produced by the acoustic-flame interaction, amplifying the wave. Other theoretical works further detailing flame-acoustic interactions, was performed by Fleiful [32], and Dowling [33, 34] and a review was written by Lieuwen [35].

A mechanism for self-induced instabilities for an external combustion system was proposed by Schuller et al [36]. A methane-air premixed annular burner, with forcing provided by a speaker at the base of the burner, was used to determine a transfer function to predict performance and onset of instability for the setup. The acoustic-flame coupling was studied in detail, specifically citing pressure fluctuations resulting from flame-flame interactions as the driving mechanism. Flame-flame interaction occurred when natural

instabilities of the flame caused flame to fold, bringing flame fronts to close to each other, quickly burning reactants in between them and resulting in an unsteady heat release and a pressure fluctuation.

Following the schematic below, Figure 2-3, self sustained oscillations result from the following interactions. A pressure fluctuation, *p*', results from the flame-flame interaction, and propagates in all directions. The pressure fluctuation generates a fluctuation at the burner outlet, p_1', which induces pressure fluctuation p_0' inside the burner, generating the velocity fluctuation v_1' at the burner outlet.

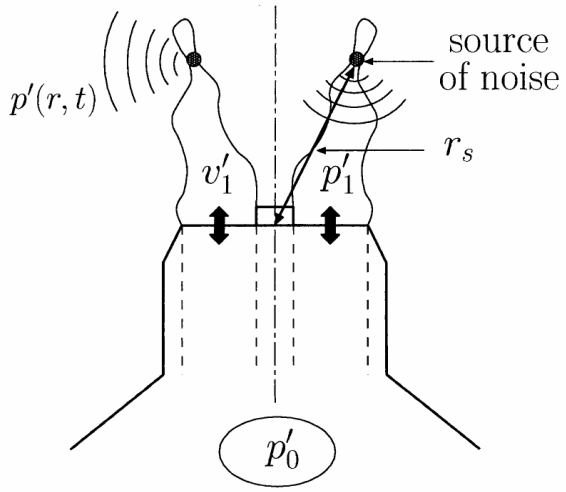

Figure 2-3 Self-induced instability mechanism for an external system[36]

Forcing a combusting flow can provide a means for decoupling vortex generation, and subsequently the combustion, from the acoustic field, since vortex shedding can be locked to the forcing frequency. Heat release from the vortices can be driven out of phase from pressure fluctuations, and reduce flame-acoustic coupling [11]. Conversely, forcing can also increase vortex-acoustic coupling, depending on the desired application. As mentioned before, RMS pressure fluctuations serve as a measure of combustion

stability. Decreased pressure fluctuations represent increased stability. As combustion is decoupled from acoustic modes, pressure fluctuation decreases due to damping effects from heat release. When combustion instabilities, and subsequent pressure fluctuations, are reduced, the flammability limits are extended since combustion near the limits are much more prone to extinction, liftoff, or flashback.

2.3 Rayleigh Scattering

A large amount of literature has been written on Rayleigh scattering. The basic theory has been discussed in combustion diagnostic texts [16, 37], detailed guidelines on its application have been described, [17], and a review with rigorous mathematical treatment of the scattering theory, [38] has been written.

Raleigh scattering is defined as the elastic scattering of electromagnetic radiation, which occurs when the electric field of the radiation interacts with the electric field of molecules [17]. After interaction with the incident light quanta, the molecules return to the same state they were in previously. As a result, there is no net energy exchange between the incident light and the particle, which means the scattered photon wavelength is the same as the incident light, and is not species-specific [37]. In Rayleigh scattering, a small wavelength change can occur, associated with a Doppler shift from scattering off moving particles. For Rayleigh theory to be applicable, the particle diameter must be less than one-tenth the wavelength of the incident light, $d<0.1\lambda$. In fact, Rayleigh theory can also be applied to clusters of molecules, as long as the cluster circumference is much less than the incident wavelength [38]. For particles larger than the size criterion, Mie scattering theory must be used instead.

Although Rayleigh scattering is not species-specific, it is well-suited for making density measurements as the scattered light intensity is directly proportional to laser power, gas density, and the scattering cross section of the gas. Using the ideal gas law, a number of properties of the flow can be determined. Molar concentration, temperature, and density can be determined from the signal. Rayleigh experiments, however, are usually designed to isolate the dependence of scattered light power to just one of these variables [37].

2.3.1 Basic Principle

The differential Rayleigh cross-section, σ_r [sr/cm^3], of a species, i, is used to describe the intensity of the scattered light for each individual molecule. It is the basis of Rayleigh scattering and is defined as a function of the species' index of refraction, n, incident wavelength, λ [cm], to the inverse fourth power, the incident angle, θ, and the depolarization ratio, α. N_o is Loschmidt's number. The equation for the cross section is shown below:

$$\sigma_{ri} = \frac{4\pi(n_i - 1)^2}{\lambda^4 N_o^2} \cdot \sin^2\theta \cdot \frac{3}{3 - 4\alpha}$$

Equation 2-1 Rayleigh cross section of a gas[17]

Typical experimental arrangements have the collecting optics perpendicular to the incident light. In addition, the spatial distribution of the scattered light bears a simple relationship to the direction of observation. An equal amount of light is scattered into the forward and back hemispheres, and the light scattered at 90^o is almost completely polarized, in which case, the depolarization ratio is assumed to be zero [17] and Equation 2-1 reduces to:

$$\sigma_{ri} = \frac{4\pi(n_i - 1)^2}{\lambda^4 N_o^2}$$

Equation 2-2 Rayleigh cross section at 90^o viewing

The effective cross-section of a gas mixture is simply the sum of the individual species' cross-sections weighted by their mole fraction, X:

$$\sigma_r = \sum_{i=1}^{j} X_i \sigma_{ri} .$$

Equation 2-3 Rayleigh cross section for gas mixture

Where the following is true:

$$\sum_{i=1}^{j} X_i = 1 .$$

The intensity of the scattered light is the product of the incident laser intensity, I_o, the total number density of the gas, N, the effective cross-section, and a calibration constant C, which accounts for the optical efficiency of the setup:

$$I_r = CI_o N \sum_{i=1}^{j} X_i \sigma_{ri}$$

Equation 2-4 Scattering intensity

The ideal gas law can replace the number density:

$$N = \frac{PA_o}{RT}$$

For an unreacted binary air/fuel mixture, the scattering Equation 2-4 can be written the following form:

$$I_r = CI_o N(X_f \sigma_{rf} + X_a \sigma_{ra})$$

Equation 2-5 Scattering intensity for binary mixture

2.3.2 Index of Refraction

The index of refraction is important for determining the cross-section of the gas being analyzed. However, the index of refraction of a gas depends on its molecular composition, temperature, pressure, and the wavelength of the incident light. As a result, determining the appropriate value of the refractive index can be difficult. A good method of determining the refractive index is through the molar refractivity, R_L, which does not contain the density dependence. A table of molar refractivity of combustion gases is given in [39]. The molar refractivity is defined by the Lorenz-Lorentz equation:

$$R_{L,i} = \frac{n_i^{\,2} - 1}{n_i^{\,2} + 2} \cdot \frac{1}{\rho},$$

Equation 2-6 Molar refractivity[39]

where ρ is the molar density of the gas (cm^3/mol).

For multi-component gas flows, the molar refractivity is merely the mole fraction weighted sum of the refractivity of the component gases,

$$R_L = \sum_{i=1}^{j} R_{Li} X_i \ .$$

Equation 2-7 Molar refractivity of gas mixture

Solving for n_i in Equation 2-6, the following is obtained:

$$n_i = \left(\frac{1 + 2\rho R_L}{1 - \rho R_L} \right)^{1/2} = \left(\frac{RT/P + 2R_L}{RT/P - R_L} \right)^{1/2},$$

Equation 2-8 Index of refraction as a function of molar refractivity

which can be used in the Rayleigh cross section equation, Equation 2-1.

2.3.3 Advantages of Rayleigh Scattering

There are numerous advantages of using Rayleigh scattering over the other scattering techniques. Rayleigh scattering produces a strong signal, and as a diagnostic, Rayleigh scattering is easy to implement: no tracer particles are needed, visible laser light can be used, and a simple 90^{o} collection arrangement will work. A laser line filter and a polarizer can be used to increase the signal to noise ratio. The scattering intensity is linearly related to the molecular number density, so the interpretation of the signal to obtain quantitative measurements is straightforward, and no complicated system calibrations are necessary [40]. With these strengths, Rayleigh scattering plays dominant roles in concentration, density, temperature, and flame thickness measurements [17]. The strong Rayleigh signal, incident light, and an ICCD to acquire and image of the flow enables planar imaging with high spatial and temporal resolution.

2.3.4 Disadvantages of Rayleigh Scattering

The largest weakness of Rayleigh scattering techniques is the absence of any spectral difference between the incident light and the signal. As a result, the signal is very sensitive to interference from stray light scattered off surfaces and Mie scattering from particles in the flow. The Mie scattering can easily be ten to twenty times stronger then Rayleigh scattering [37]. Mie scattering from particles is the most significant source of interference since not only do particles scatter; particles such as soot will absorb incident and scattered light. Also, the scattering is not species-specific, limiting Rayleigh scattering diagnostic of cold flows to binary mixtures, or requiring predetermination of cross sections for more complicated mixtures. Application to the temperature

measurements in most practical combustion fields is hindered by the variation of the overall scattering cross section of the scattering species through the flame [17], although the cross section for simple hydrocarbon flames has been found to vary by no more than 10%, because nitrogen remains the major species throughout the reaction [41]. Because of these weaknesses, Rayleigh techniques are restricted to only simple systems.

2.4 Rayleigh Imaging

A large number of experiments have used Rayleigh scattering, in either point or planar form, as a combustion diagnostic. Rayleigh imaging has been used in a wide range of studies, including detailed studies of turbulent diffusion flame structure [42] fuel distribution in a diesel engine cylinder [40], temperature distribution in a spark ignition engine cylinder [43] and in a Mach-six wind tunnel [44, 45]. Several studies have implemented multi-laser simultaneous planar diagnostics. Raman-PLRS [46] and PLRS-PLIF [43, 47, 48] are combinations that have been used.

If a gas mixture is selected so that the scattering cross-section does not change much between reactants and products, then the Rayleigh scattering signal is directly proportional to the total number density, and subsequently inversely proportional to temperature through the ideal gas law. Many studies have taken advantage of this relationship. For combustion studies, the fuel must be carefully selected so the products, reactants, and intermediates have a constant cross-section. For premixed cases, the requirement is that the cross-section of the burned and unburned gases needs to be equal. For diffusion flames, the cross-section of the reactants and products needs to be equal to that of air.

One study was done with a fuel mixture of 33.2% H_2, 22.1% CH_4, and 44.7% N_2, by volume, was used in a study by Bergmann et al, [47]. This investigation of turbulent diffusion flames used single point Raman and Rayleigh scattering and 2-D LIF and PLRS. Single point measurements possessing high accuracy were used to build probability density functions to characterize the flames. The simultaneous measurements also allowed the study of the correlations between the various quantities being measured. The 2-D images, far less accurate compared to the point measurements, were used to capture instantaneous spatial structures, distributions, gradients, correlations, and mixing characteristics.

A CH_4, H_2, and air diffusion flame and premixed flame were studied by Marshall Long et al. [46]. The group devised a method of using both Rayleigh and Raman scattering to simultaneously map out CH_4 concentration and temperature of the flow. The selected fuel was a 38% CH_4 and 62% H_2 mixture, where the change of the fuel's Rayleigh cross-section due to combustion is only 2% [41]. The laser sheet was formed using a multi-pass cell created using a pair of cylindrical reflectors. This method generates a very intense light sheet, ~30 times more intense than if the sheet were made with a lens in one pass. The resulting signal was collected at 90^o and passed through a lens, then through a beam splitter. The diverted portion of the signal, ~8% of the signal, was collected as the Rayleigh image, while the non-diverted portion passed through a filter selected for the Raman scattering wavelength specific to the gas being detected.

Also using the CH_4 and H_2 mixture, Everest et al [49] used PLRS to obtain detailed instantaneous temperature fields and temperature gradients in a turbulent diffusion flame. Thermal dissipation was determined, serving as an indicator of thermal

mixing rates. A pulsed dye laser at 511 nm and a cylindrical lens was used to make the light sheet. Homogeneous temperature regions with small thermal gradients and thin thermal mixing layers with large thermal gradients were found. Flame-vortex interaction was also observed, causing thin thermal mixing layers and local flame extinction or quenching.

Simultaneous NO concentration, OH concentration, and temperature mapping of a swirl burner was performed by Böckle et al using two KrF excimer lasers and three ICCDs [50]. A lean r ϕ=0.83 mixture of CH_4 and air was studied. The Rayleigh cross section was experimentally determined using point Raman measurements of majority species concentrations. In regions of sufficient mixing near the burner exit and in the recirculation zones, the overall Rayleigh cross section of the reacting gases were found to have a standard deviation of less then 1.5%, allowing the constant cross section assumption.

CHAPTER 3 Setup and Data Reduction

The combustor in this study is the same one used in [4], although it has been modified for a fuel flow with a surrounding coflow of air, supplied by a filtered pressurized air line in the room, for a diffusion flame. The fuel flow is a combination of 38% CH_4 (99.97% pure) and 62% H_2 (99.995% pure), supplied from Airgas. The Rayleigh cross-section of the fuel mixture, and its combustion intermediaries and products, are close to that of air, within 2%. A table of cross-sections, as calculated, of the relevant gases is shown.

Gas	σ_r (cm^2/sr)
H_2	1.32E-28
CH_4	1.34E-27
H_2-CH_4	5.91E-28
Air	5.86E-28

Table 3-1 Cross sections of gases used

A diffusion flame mode was selected due to concerns of flashback into the combustor, given the high flame speed of a hydrogen-methane premixture. A coaxial configuration with a sheath flow was used to reduce the influence of cross-breezes in the room.

3.1 Combustor

The combustor is composed of two major parts. The main portion is a long tube, with an inner diameter of 1 inch, threaded so 7.83-inch diameter round plates with center holes can screw on to each end, making a dumbbell shape with an overall length of 9.8 inches. There are two 1/8 NPT threaded holes on the side of the tube for the introduction of air. A flame holder is secured to the top plate. The second portion of the combustor is a smaller tube, with an outer diameter of 0.75 inches and a 1/8 inch wall

thickness for the center flow, welded to a disk made to mate to the bottom plate of the main portion. The center tube has an inside and outside taper at the top, which is flush with the burner exit, meeting at an included angle of 40^{o}. This taper was made to eliminate a recirculation zone over the wall of the center tube, although interesting instabilities still can result from the collision of the fuel and air streams, which have a small radial component resulting from the taper. The disk to which the center tube is welded has two holes drilled through the side for fuel to be introduced into the center tube. Means for the trumpet speaker to screw into this disk for direct excitation of the center flow is provided. A diagram and a picture of the combustor is shown below, Figure 3-1.

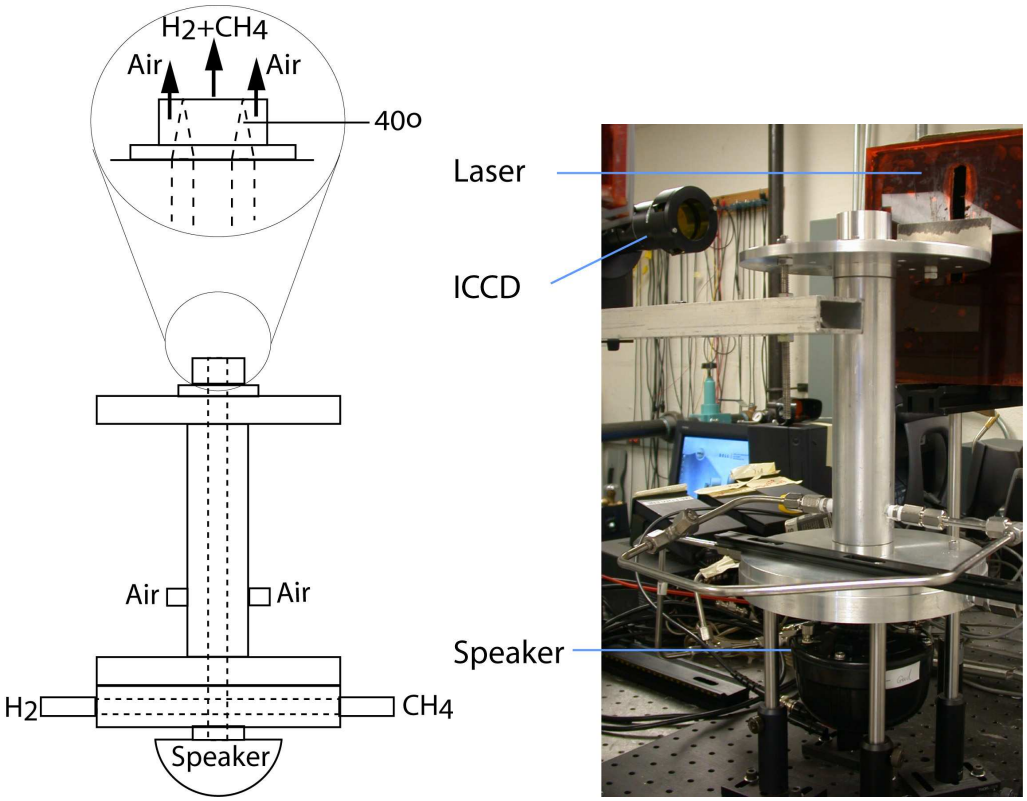

Figure 3-1 Diagram and picture of the combustor

3.2 Laser and Camera

The laser used for the Rayleigh scattering is a New Wave Research Solo PIV Nd-YAG operating at 532 nm. The laser is intended for particle image velocimetry, so it contains two laser heads, but only one was turned on. The laser system contains beam-shaping optics at the emitter to generate a laser sheet, but the focal length of these optics was far too long given space constraints in the lab. The system beam shaping optics were removed and a plano-concave lens to spread the beam vertically, followed by a plano-convex lens to converge the beam into a thin sheet over the burner, were placed in front of the laser. The laser pulse power was set to the maximum, 500 mJ at 5 ns, for the strongest possible signal. The resulting light sheet produced a half-inch high area of usable laser light sheet. A high resolution (1280 by 1024) PCO-DiCam Pro ICCD is placed at 90^{o} relative to the laser sheet for imaging. A 532 nm filter is incorporated into the camera optics to isolate the desired Rayleigh signal, and the camera is triggered by the laser flashlamp. The exposure time of the camera was minimized to only capture the laser pulse, diminishing interference from chemiluminescence [17]. Images were recorded using the PCO software provided with the camera. Since the laser sheet occupied a fairly small area on the chip and since the camera lens employed was not well optimized for the camera, the region of interest is limited to a rectangle of 576 by 544 pixels, which is further trimmed down to an area of 351 by 131 pixels by the calculation program.

Because Rayleigh scattering is so sensitive to interference, care was taken to reduce reflection from specular surfaces. The laser emitter and shaping optics were placed under a box, lined with black felt, with a slot for the laser light to come out. A

beam dump, also lined with black felt, was made to catch the beam after it passed over the burner. The laser sheet was positioned a third of an inch above the burner to reduce interference from scattering off the burner surface, but close enough to the burner to image the more interesting parts of the flame.

3.3 Flow Forcing

A Sanming Electronics Trumpet Horn Unit model S-75A, now discontinued, provided the forcing for this setup. A sinusoidal wave from a Wavetek Universal Waveform Generator, model 195, was fed into the microphone input of a Bogen Classic Series C-100 amplifier. The output was then wired into the terminals of the speaker. A Tektronix TDS 3014 oscilloscope was used to monitor the signal going from the signal generator to the amplifier and from the amplifier to the speaker. The forcing amplitude was maintained at 10 V pulse to pulse.

To phase lock the camera, in order to image the flame a specific times during forcing, the SYNC out of the Wavetek was connected to trigger input of the laser system's IO box. The laser output signal from IO box was connected to the flashlamp fire on the laser. The laser system controlled the triggering of the laser, which subsequently triggered the camera, according to user inputs. The camera is the limiting factor in the image acquisition rate. The fastest the camera could be run in this configuration is about 10 Hz, compared to the forcing, which occurs at frequencies between 150 Hz to 350 Hz. A schematic of the setup is provided in Figure 3-2.

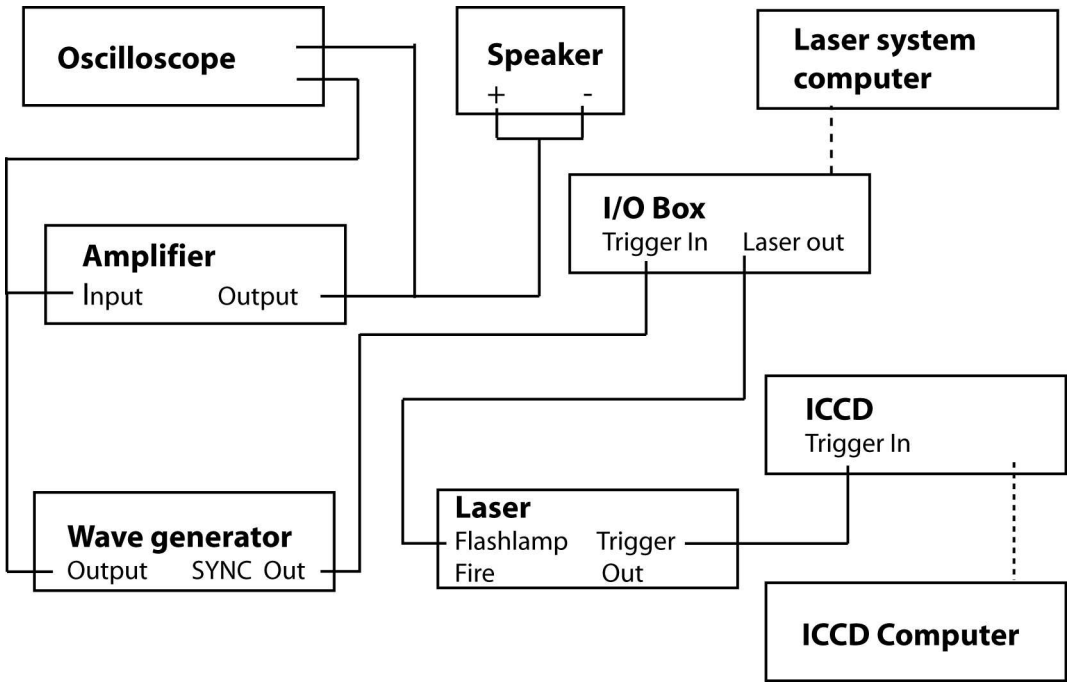

Figure 3-2 Schematic of phase-locking scheme

3.4 Flow Control

The flow rates of the H_2, CH_4, and air are controlled with O'Keefe Controls choked orifices. The flow rate is a function of the pressure upstream of the orifice, assuming an isentropic flow. The orifice was kept small so that the area contraction between the orifice and the gas line diameter was enough to ensure a choked condition and that the static pressure, measured by pressure transducers, in the line was almost equal to the stagnation pressure. The required upstream pressures were calculated using a program written in Mathcad (Appendix C). The pressure in each supply line was controlled using the regulators on the gas bottles on the air supply line. Pressures are monitored using Setra pressure transducers wired to Setra Datum 2000 readouts. Parker solenoid valves are plumbed into the gas lines to turn the gas flows on and off and were controlled from a remote switch box.

3.5 Calibration Images

Two calibration images are needed for the data reduction. One image is needed to quantify the background scattering and the other image is needed as standard condition. The significance of each will be discussed later. To quantify background scattering, a helium jet was used, and air was used as the standard, or ambient, condition. The widest gas jets that could be achieved were needed to make the widest possible diagnostic region. To accomplish this, the center tube of the burner was removed and the flame holder was replaced with a similarly shaped nozzle, to preserve spatial scattering characteristics, but with a wider opening. Since taking out the center tube essentially involved disassembling the burner, it was critical to realign the burner with the camera exactly. Using a grid placed at the burner nozzle, a height gauge attached to the burner, and the ICCD, realignment was performed by matching the pixel locations of the grid lines to a picture of the grid taken before adjusting the burner. The helium and air calibration images (fifty shot averages) are shown in Figure 3-3.

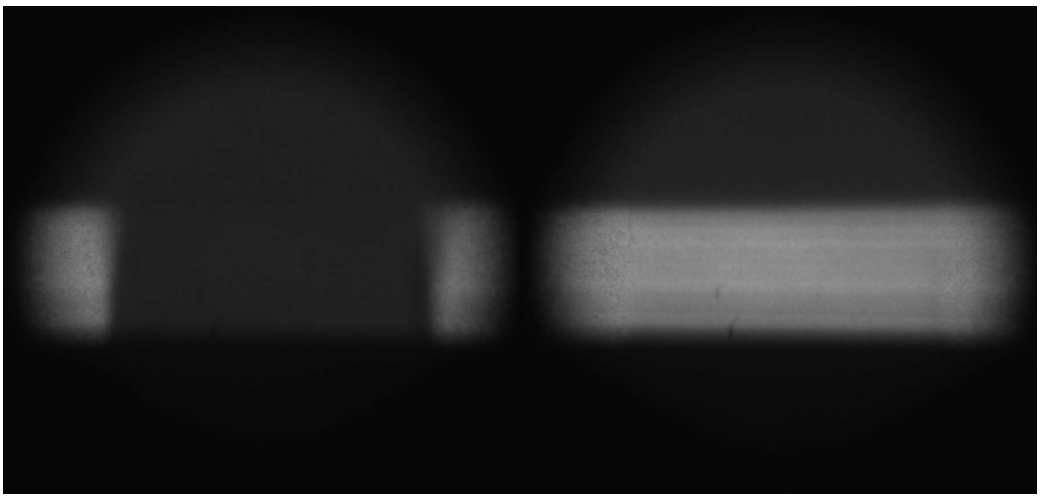

Figure 3-3 PLRS, fifty shot average, of helium jet (left) and air jet (right)

3.6 Data Reduction

The total detected intensity can be assumed to contain Rayleigh scattering, background scattering, and shot noise, Equation 3-1 [17].

$$I_t = I_r + I_b + I_n .$$

t= Total intensity
r = Rayleigh Intensity
b = Background Intensity
n = Shot noise

Equation 3-1 Instantaneous total intensity

The acquired temperature maps of the flames are averaged over fifty temperature maps, so contributions to the temperature from the shot noise is assumed to average out. The background intensity can be assumed constant as well, since any possible scattering surfaces are stationary. The mean signal becomes the following:

$$\overline{I_t} = \overline{I_r} + \overline{I_b} .$$

Equation 3-2 Average total intensity

$\overline{I_b}$ is set equal to the helium calibration image. The cross-section of helium was calculated to be less then 2% that of air. Therefore, it is assumed that the helium intensity is negligible, so the image is considered an image of solely the background scattering. Subtracting the helium image from the image of the flame, and dividing the difference by the ambient temperature image, $\overline{I_{r,amb}}$, also with the helium image subtracted, Equation 3-3 is attained:

$$\frac{\overline{I_r}}{\overline{I_{r,amb}}} = \frac{\overline{I_t} - \overline{I_{He}}}{\overline{I_{t,amb}} - \overline{I_{He}}} .$$

Equation 3-3 Average Rayleigh signal to average Rayleigh ambient signal ratio

Replacing $\overline{I_r}$ and $\overline{I_{amb}}$ with Equation 2-4 and substituting the perfect gas law in place of N, Equation 3-3 becomes

$$\frac{CI_o \frac{PA}{RT}\sigma_r}{CI_o \frac{PA}{RT_{r,amb}}\sigma_{r,amb}} = \frac{\overline{I_t} - \overline{I_{He}}}{\overline{I_{t,amb}} - \overline{I_{He}}}.$$

Equation 3-4 The perfect gas law and Rayleigh intensity definition substituted in to Equation 3-3

Assuming that CI_o is constant shot to shot for each pixel, that the pressure is constant, and that the cross-section remains close to that of the air, then equation reduces to Equation 3-5, used in [49]. The ambient image, here, is used as a method to avoid having to determine CI_o for each pixel. Also, it allows for spatial non-uniformities in the light sheet, the horizontal stripes in the ambient image, without affecting calculations. This equation, however, assumes that the non-uniformities are temporally constant.

$$\frac{T}{T_{amb}} = \frac{\overline{I_{t,amb}} - \overline{I_{He}}}{\overline{I_t} - \overline{I_{He}}}$$

Equation 3-5 Temperature as a function of total intensity

Each image is converted from the camera software's proprietary format into a bitmap image. Image averaging and temperature calculation are performed using a Matlab program. A grid was imaged to correlate pixel locations to real locations.

3.7 Matlab Program

The Matlab program written for this experiment is included in Appendix D. When an image is read into Matlab, the program converts it from an indexed image, where each pixel value is between one and two hundred fifty five, to an intensity image,

where each pixel value is between one and zero. Before averaging, the dust captured in the images need to be removed. For the most part, dust is only present in the air surrounding the flame or the gas jets in the calibration images because the gases are filtered, so error in the temperature calculations from the removal of the dust should be minimal. For the ambient calibration image, a histogram, shown in Figure 3-4, is generated for each of the fifty images. A median value, without considering the lower and higher intensity bins, is determined. Values over 0.7 in the ambient calibration image are considered dust and replaced with the median value. The fifty calibration shots for the ambient and noise are then averaged.

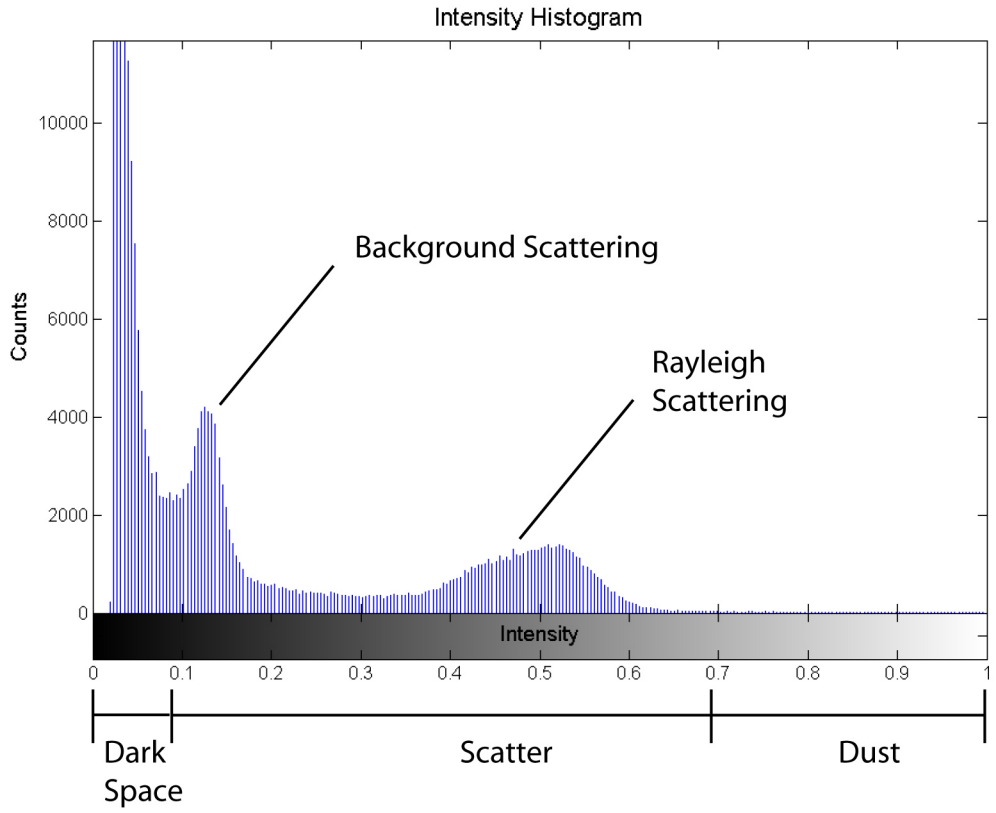

Figure 3-4 Dust replacement in ambient condition image

Dust in the data images, pixels with values greater than 0.7, is removed and is replaced using values from corresponding pixels from the ambient calibration image. The result of this replacement scheme is shown in Figure 3-5.

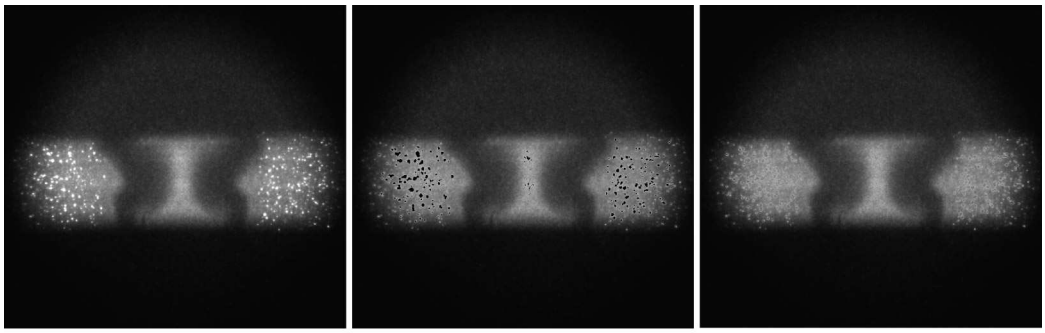

Figure 3-5 Dust replacement for all other images

The calibration images and the data images then are trimmed to the usable area, about two inches by half inch. The temperature field is calculated using Equation 3-5. This scheme generates fifty temperature maps of each phase angle of each frequency. The fifty temperature maps are averaged together and a standard error field, Equation 3-6, can be generated.

$$s_e = \frac{\sigma}{\sqrt{n}}$$

Equation 3-6 Standard error equation. Note: σ is the standard deviation and *n*=50

At high temperatures when the Rayleigh signal is very low, the signal to noise ratio decreases, and shot noise becomes a significant problem. The shot noise can cause the denominator for Equation 3-5 to drop to zero, making the temperature approach infinity, or become negative. In this case the program does not allow the denominator to become negative and limits the maximum value of the temperature calculation to a value of 2350 K, closely corresponding to the adiabatic flame temperature, which is 2290 K

CHAPTER 4 Data and Analysis

4.1 Test Conditions

Rayleigh scattering images were gathered for four flow conditions. For three conditions, the center jet was kept at a mean velocity of $\bar{u}_{inner}$=1.36 m/s while the mean velocity of the outer flow were $\bar{u}_{outer}$= 1.36 m/s, 2.72 m/s, or 0.68 m/s. This leads to a velocity ratio, V_r, of $\bar{u}_{outer}/\bar{u}_{inner}$= 1, 2, and 0.5 respectively. For one of the four conditions, the velocity ratio was kept at V_r=1 but the mean velocity of the jets was increased to 2.16 m/s. The flow conditions are summarized in Table 4-1.

Flow Condition	$\bar{u}_{inner}$ (m/s)	$\bar{u}_{outer}$ (m/s)	Velocity Ratio(V_r)	Re_{inner}	Re_{outter}
1	1.36	1.36	1	513.45	540.91
2	2.16	2.16	1	816.23	859.89
3	1.36	2.72	2	513.45	1081.82
4	1.36	0.68	0.5	513.45	270.46

Table 4-1 Flow conditions

At each condition, an unforced image of the flame is taken and then the effects of nine forcing frequencies are characterized. The frequencies and equivalent Strouhal numbers, defined by Equation 4-1, are listed in Table 4-2.

$$St = \frac{f(D_{outer} - D_{inner})}{\overline{u_{inner}}}$$

Equation 4-1 Strouhal number

$\bar{u}_{inner}$ (m/s)	Frequency Hz									
	150	180	200	230	250	270	300	330	350	St
1.36	0.70	0.84	0.93	1.07	1.17	1.26	1.40	1.54	1.63	
2.16	0.44	0.53	0.59	0.68	0.73	0.79	0.88	0.97	1.03	

Table 4-2 Experiment frequency range and Strouhal numbers

For each frequency at each flow condition, phase-locked images were acquired from 0^o to 330^o in 30^o increments. At each 30^o increment, fifty images were recorded, resulting in twelve sets of fifty images for each frequency. Each of the fifty images is the accumulation of ten laser shots. The frequencies were selected to be less than 400 Hz since it has been noted that for small velocity fluctuations, flames only respond to low frequencies [51].

The entire flame itself was imaged, after acquiring all of the Rayleigh images, for a few frequencies for flow condition #1. The flame images were qualitatively paired with the corresponding Rayleigh scattering images. Since the phase of the passing fluid structures had changed somewhat, the flame images were matched to the Rayleigh images by matching the features of each image, particularly where the ambient air is entrained into the flame. This became more difficult in the higher frequencies where features of the flame became less distinguishable. The comparison of the flame image to the Rayleigh scattering image serves to orient the reader to the location of the measurement area in relation to the flame structure, about a third of an inch from the burner exit. Figure 4-1 shows an example of a flame paired with the corresponding Rayleigh image.

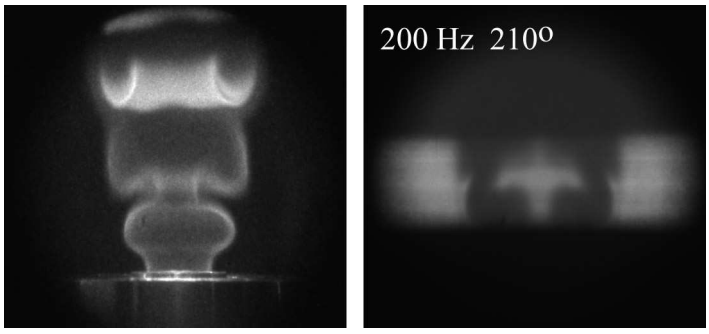

Figure 4-1 PLRS in relation to flame

More images were intended, but degradation of the speaker caused repeatability problems. Ideally, images of the flame would have been taken while gathering all of the the Rayleigh images. Images for 150 Hz, 180 Hz, 200 Hz, 230 Hz, 320 Hz, and 350 Hz forcing frequencies were gathered.

4.2 Data

4.2.1 General Comments

Some general comments can be made about the effects of forcing on each flow condition. The temperature distributions for the unforced conditions are as expected, two almost vertical bands, although sloping slightly outwards from the center, of higher temperature. The majority of the fuel jet is at the ambient temperature, increasing in temperature away from the center to the location of the flame. After the flame region, the temperature drops back to the ambient value. The temperature maps of the unforced cases are shown in Figure 4-2.

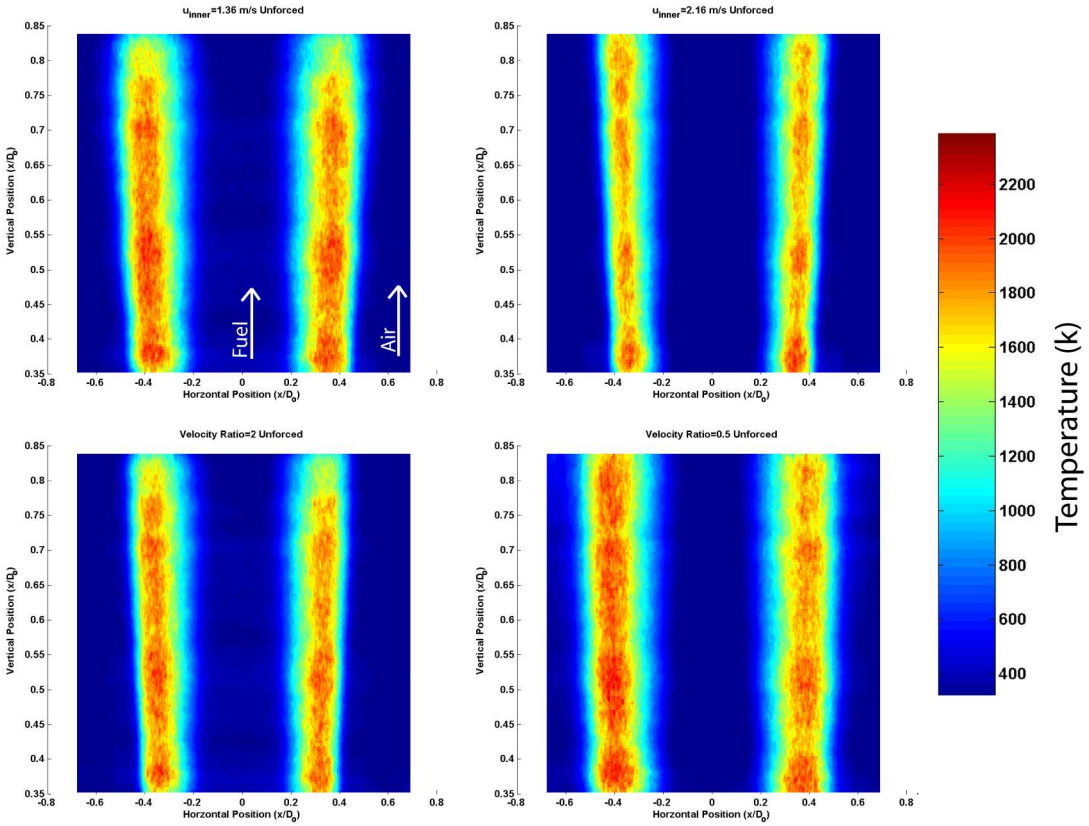

Figure 4-2 Unforced temperature maps for flow condition 1 (top left), 2 (top right), 3 (bottom left), and 4 (bottom right)

When forcing is applied, the flame sheet becomes progressively wavier, as does the temperature distribution, as forcing frequency goes from 150 Hz to 180 Hz. In the 200Hz to 300 Hz range, significant entrainment of the fuel and air from cooler regions into the higher temperature regions occurs. In this forcing range, the flame increases in brightness and wrinkles significantly, occupying an area that spans about an inch above the burner before the sooty region of the flame begins. Jet spread also increases in this frequency range. For the unforced cases and for forcing frequencies with weaker influence, the reaction region stretches several inches above the flame. For higher frequencies, 300 Hz and greater, the entrainment levels drop off and the temperature distribution becomes wavy again as jet-spread decreases until the flame appears unforced.

A few images of the flame are shown in Figure 4-3 to illustrate the development of the flame, the remaining images are in Appendix A.

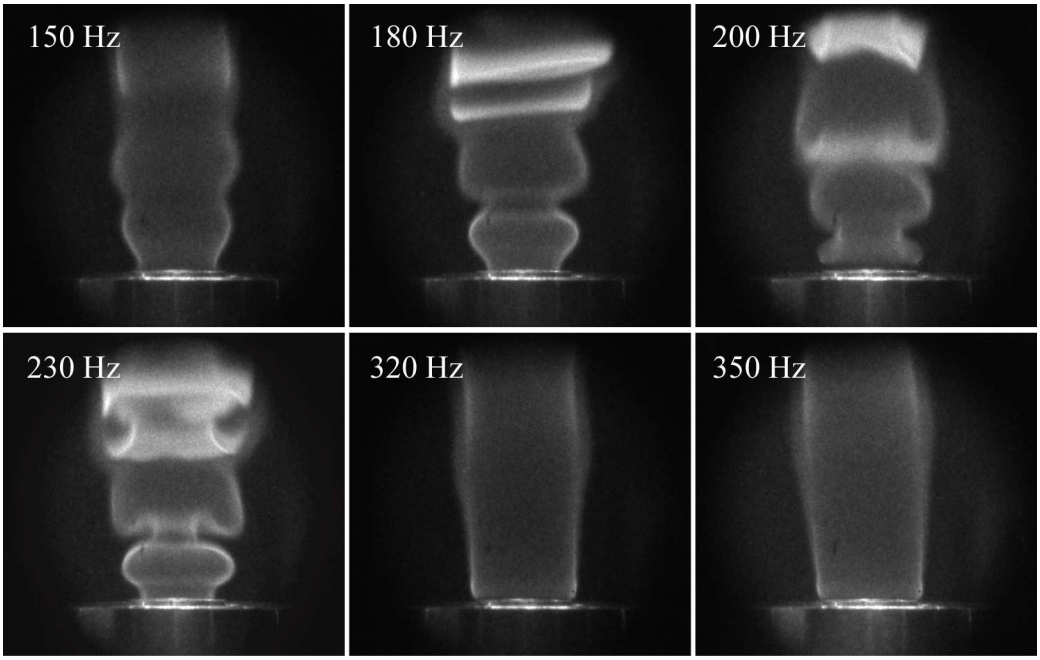

Figure 4-3 Progression of flame shape through forcing range

Forcing also tends to decrease the flame's sensitivity to cross breezes. When the flame is unforced, there was mild lateral movement of the flame, but as forcing was applied, the movement decreased. As the preferred mode was approached, the flame became very stable, unless an unstable mode is reached. The onset of an unstable mode will be discussed later. At higher frequencies, the flame became less stable as forcing effects on the system decreased.

For some frequencies, asymmetry in the temperature distribution can be seen. This asymmetry is due to the lack of flow straighteners in the burner. Since air is fed into the outer jet through two ports, and H_2 and CH_4 are fed into the center jet through two separate lines, a swirling component was unintentionally added to the velocity. Furthermore, a larger volumetric rate of H_2 was required than the CH_4, also generating

asymmetry. Asymmetry can also be attributed to eccentricity between the inner jet tube and outer tube due to fabrication errors.

For each flow condition, a temperature slice is taken at the midline, at $y/D_o=0.6$, of the image area, for all the forcing frequencies at 0^o, 90^o, 180^o, and 270^o phase angles, to summarize the data and facilitate discussion and comparison of the effects of forcing. The unforced condition for the particular flow condition is also plotted as a baseline. All temperature maps, including the 0^o, 90^o, 180^o, and 270^o phase angles, are included in Appendix B, and are at times are referred to.

There appear to be several competing factors affecting the flame temperature. There are large-scale effects, large vortices and entrainment, and there are small-scale effects, diffusion and small scale mixing enhancements. Large-scale vortices have a mixture of influences. Fresh reactants are entrained by the vortices, and the residence time in the high temperature regions is increased as the path of the reactants becomes contorted by the fluid dynamics. This allows more time for interdiffusion of fuel and air to occur. Mixing can also be enhanced through shearing and straining of the flow. In general, these effects lead to more intense combustion until a critical shear is reached, beyond which local extinction could conceivably occur. However, cool pockets of gas that become entrained can also cool down the flame. In addition, as cooler gases become entrained, and the vortex becomes stronger, shear and strain effects on the flame can cause the reaction region to stretch and thin, causing quenching. Jet spread and the penetration depth of entrained gases are a measure of the vorticity strength. Small scale mixing is expected to increase monotonically with frequency as the wavelength of the disturbances from the speaker decrease.

4.3 Flow condition 1&2 Velocity Ratio, V_r=1

4.3.1 Flow condition 1, U_{inner} = 1.36 m/s, Velocity Ratio=1

This flow condition is the baseline for comparison for the other flow conditions. The unforced temperature curve for this flow condition begins to increase from the ambient temperature at $x/D_o \approx \pm 0.55$ and peaks at ±0.40, at about $T/T_{amb} \approx 6$. The temperature more gradually drops back to ambient temperature towards the center of the jet, not as suddenly as the temperature rise at the outside of the flame.

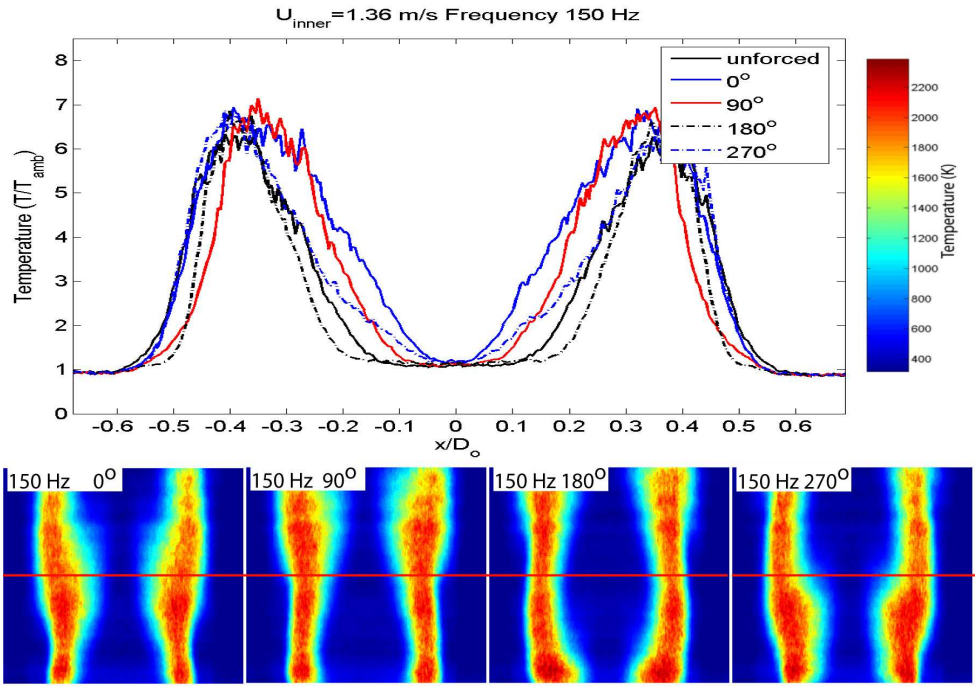

Figure 4-4 Flow condition 1 temperature maps and midline plot, 150 Hz

The 150 Hz forcing condition, Figure 4-4, does not cause a very large rise in the temperature over the unforced case. This forcing frequency generates passing thick and thin reaction regions that result from the coalescing of vortices. The passing thick and thin regions can be seen in the midline temperature plot. From 0^o to 90^o a thick region of slightly higher than ambient temperature gas passes through the middle of the flow,

followed by a high temperature region thinner than the ambient case at 180°. The midline temperature at 270° indicates the beginning of the passing of another thick region. The temperature maps at 90° and 180° hint at the beginning of entrainment of air. The outer edge of the high temperature regions for these phase angles are slightly closer to the axis of the jet compared to the unforced case. The temperature in the middle of the fuel jet remains close to ambient. Using the location where the temperature curve drops back to the ambient temperature as an indicator of jet spread, then the jet spread for this case is the same as the unforced case.

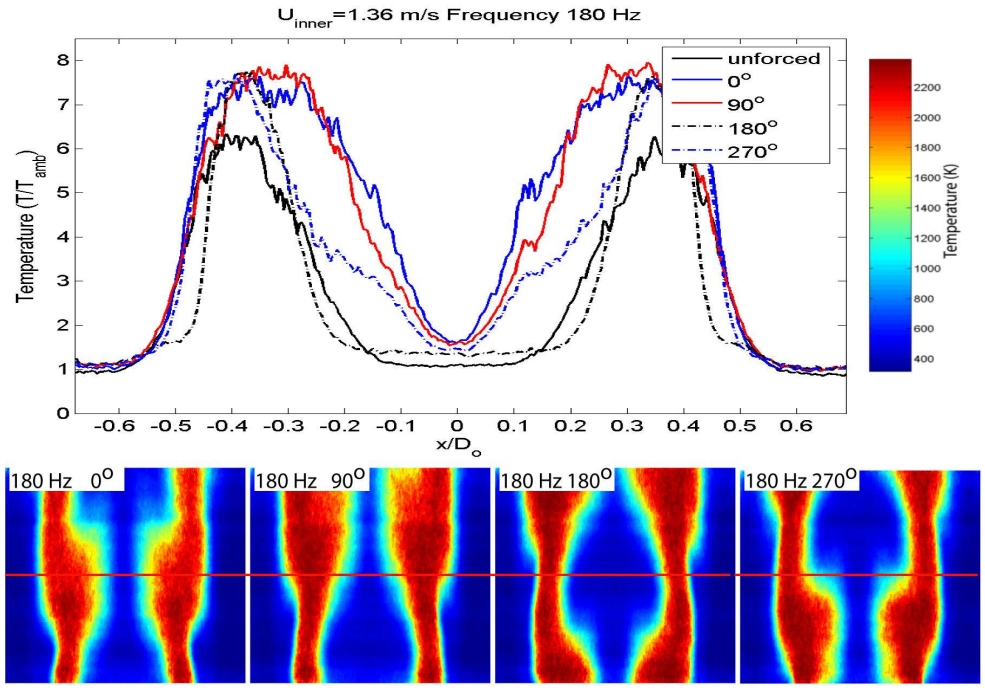

Figure 4-5 Flow condition 1 temperature maps and midline plot, 180 Hz

In the 180 Hz forcing frequency case, Figure 4-5, there is a sharp increase in the temperature over the unforced case for all times in the forcing, and the temperature in the very center of the fuel flow begins to increase over the ambient temperature. The higher temperatures in this regime indicates more intense small scale mixing from the forcing

and longer residence time of the reactants from the growing vortex, providing for greater volumetric heat release and therefore an increase in local temperature. The temperature map at 0^o, and at 30^o to 60^o in Appendix B.1 shows a slight temperature drop at these phases in the forcing. The lower temperatures can be attributed to the beginning of entrainment of cooler gas from the fuel and surrounding air. The width of the flame temperature peaks indicated on the midline temperature curve at 180^o is thin, spanning from ±0.25 to 0.45±, compared to the unforced case which spans from ±0.15 to ±0.50. The thin peak widths for 180^o curve show the bulging of the fuel jet and the encroachment of air from the surrounding flow.

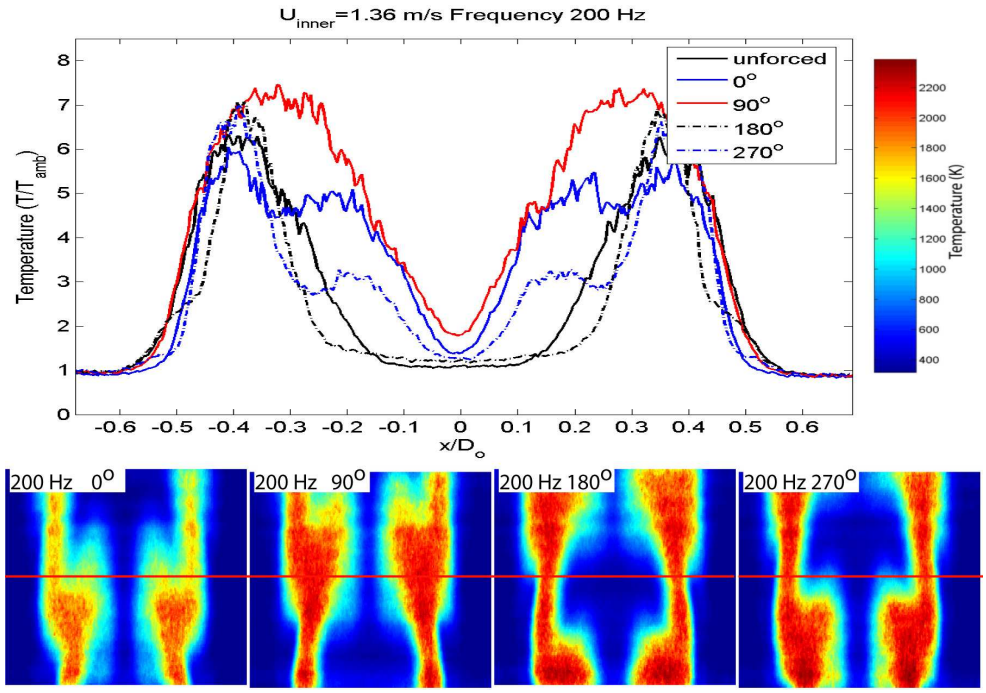

Figure 4-6 Flow condition 1 temperature maps and midline plot, 200 Hz

Temperature maps of the 200 Hz forcing case, and the centerline plot, shows an overall decrease in peak temperature compared to the 180 Hz forcing case. The entrainment of the cooler gasses in this case becomes significant, causing the temperature

to drop, especially at 0° where the temperature drops below the unforced case at the midline. Dips in the temperature plot at ±0.25 and ±0.3 for 0° and 270° curves illustrate the penetration of cool fuel into higher temperature regions. Cool coflowing air can be seen pushing in from the sides of the 180° plot. Peak temperature values approach the peak values of the unforced case, except for 90° phase, which has higher peak temperatures.

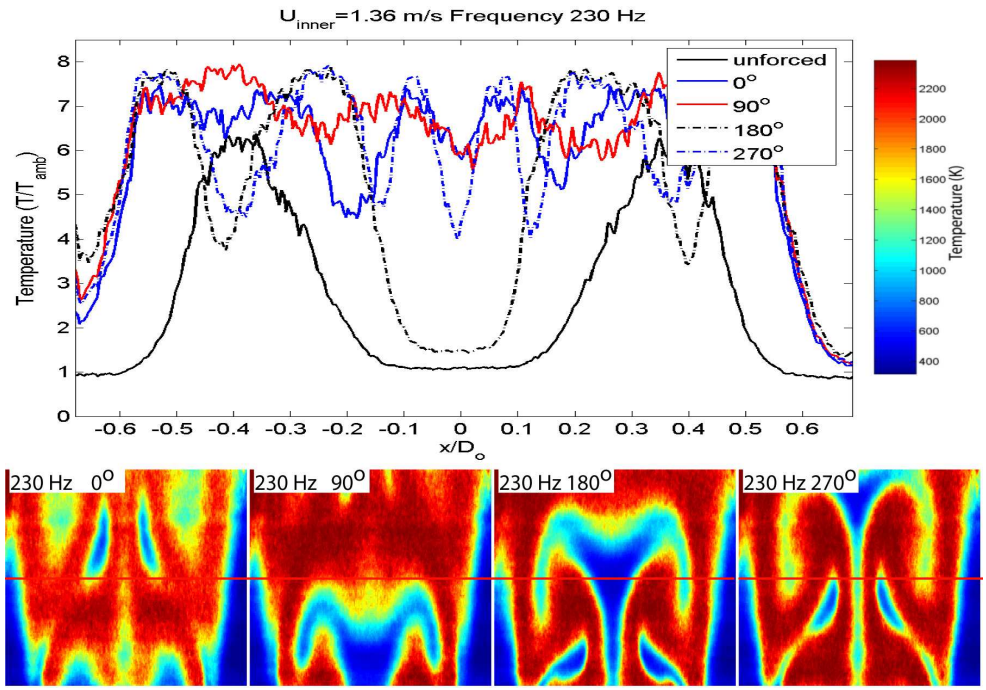

Figure 4-7 Flow condition 1 temperature maps and midline plot, 230 Hz

At 230 Hz some very interesting features are observed. The cool air and fuel are entrained deeply into the high temperature regions. The temperature distribution here looks very similar to the entrainment in Figure 2-2. The vortex pairing observed by Meyer, [19], may be the specific mechanism for the entrainment in this forcing case. Furthermore, the flame pinches off pockets of cold air, which heat up as they move downstream. These pockets are shown in the top half of the temperature plots at 0°, 30°,

and 60^o (Appendix B.1). A pocket of fuel can be seen being pinched off in the temperature map at 90^o. The overall temperature of the flame, again, drops off at 0^o due to the enveloped cool gases, but temperature for the majority of the images, from 60^o to 330^o, is largely saturated at 2350 K. The temperature map at 270^o shows air extending far into the jet. The corresponding temperature midline curve so the entrained air reaching to ±0.10, where $T/T_{amb} \approx 4.0$, from the center of the flow. The fuel in the 180^o temperature map can be seen reaching out to ±0.40, concluded from the 180^o midline temperature curve. The midline temperature curves for each degree increment from ±0.50 to ±0.60 are much higher than the unforced case. In fact, the temperature of the unforced flame drops back to ambient temperature at the radial position ±0.55, while the temperature remains $T/T_{amb} > 7.0$ for the forcing at 230 Hz. The high temperature indicates a large jet spread for this forcing. The high temperatures calculated for this case can be credited to enhance small scale mixing from the increased forcing frequency and a longer residence time allowing for more diffusion of the mixing layers, and possibly from the shearing and straining of the flow.

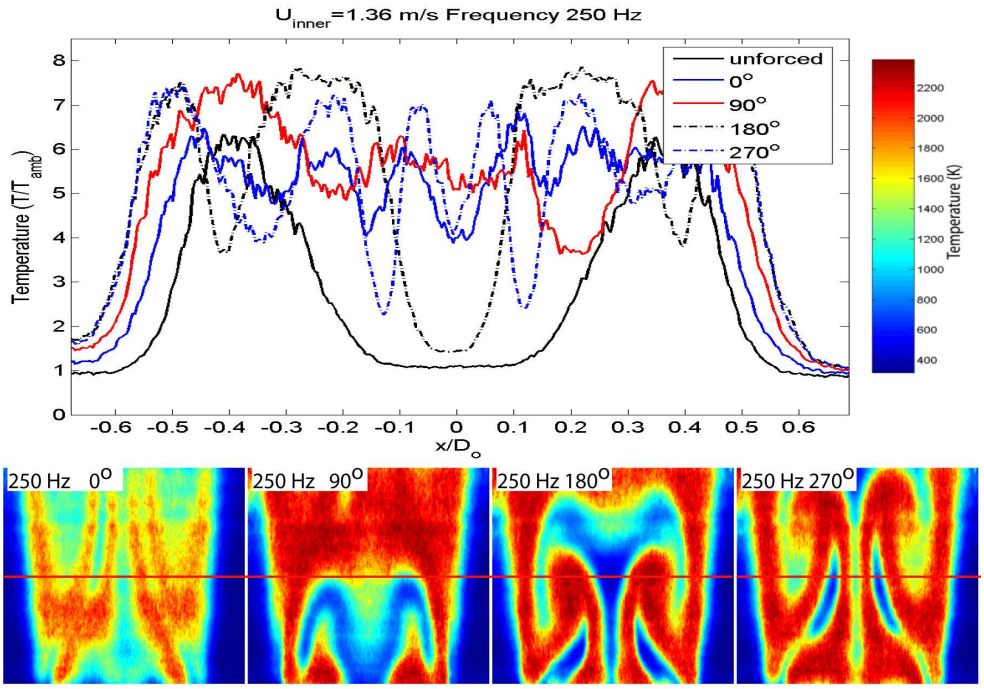

Figure 4-8 Flow condition 1 temperature maps and midline plot, 250 Hz

The characteristics of the 250 Hz forcing case are similar to the 230 Hz forcing, except that the temperature distribution is generally lower. Compared to the 230 Hz case, the high temperature regions of the 250 Hz case are stretched out longitudinally and thinner in the spanwise direction as even more air and fuel become entrained, especially at 0^o. The two dips in the temperature curve at ±0.10 for 270^o show how far into the jet the air becomes entrained, clearly visible in the full field plot. The dips in the 270^o plot, visible in the full-field image, at ±0.35 illustrate how far out the fuel jet reaches. Looking at the temperature map, the air pockets in the 270^o temperature map are thinner and more stretched out than the ones observed in the 230 Hz 270^o image. This suggests a higher vorticity strength for the 270 Hz forcing. The reaction region of the flame becomes strained and thin, and with the entrained air, the temperature of the flame decreases compared to the 230 Hz forcing case.

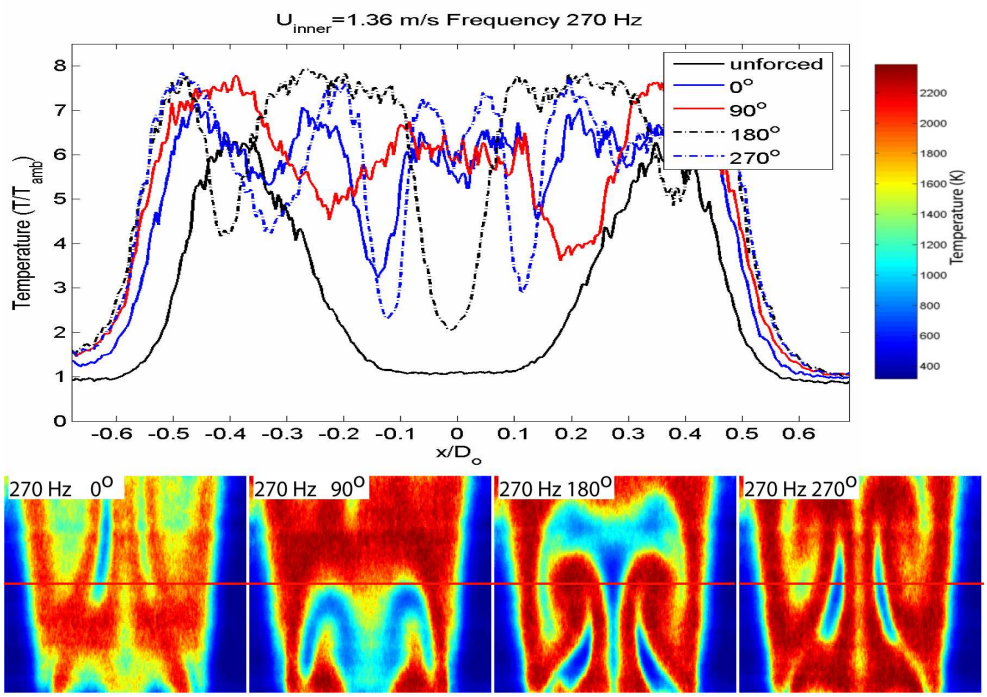

Figure 4-9 Flow condition 1 temperature maps and midline plot, 270 Hz

Forcing at 270 Hz, again, is very similar to the 230 Hz and 250 Hz cases, although the temperature tends to be a little higher then the 250 Hz case, especially at 0^{o}. The increase in temperature over the 250 Hz forcing can be attributed to either more vigorous small scale mixing or decreased entrainment of the cooler temperature air and fuel. The conclusion can be made from the midline temperature curves and the images that the maximum jet spread and the preferred modes of the combustor occur in the frequency range of 230 Hz to 270 Hz. This is also the range where if the amplitude of the forcing is increased by a small amount, the flame collapses into an unsteady regime. The turbulent flame is discussed later, in Section 4.5.

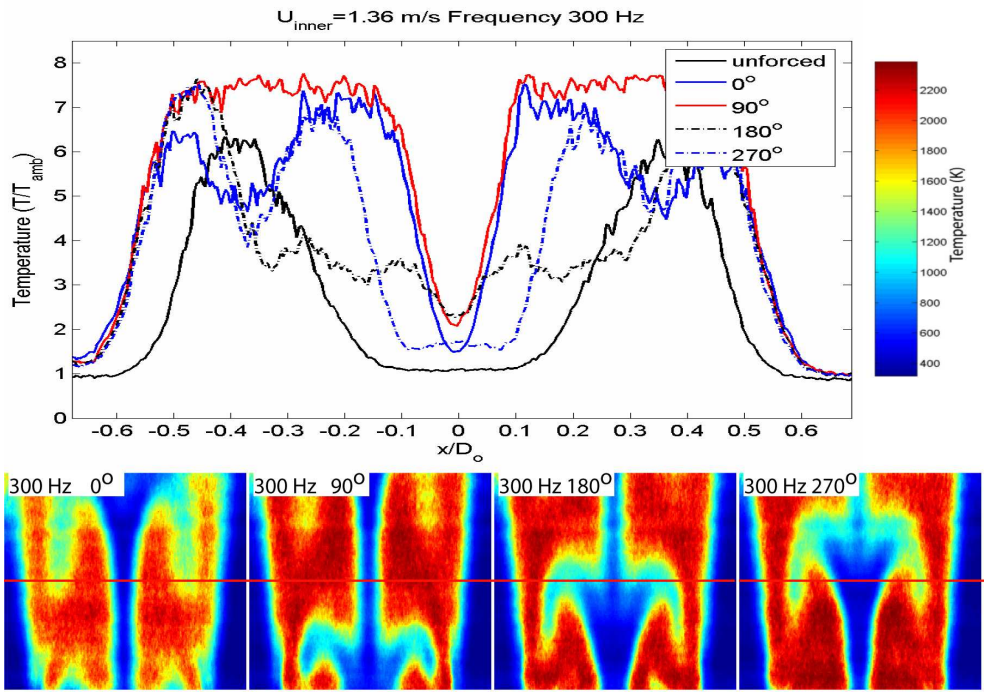

Figure 4-10 Flow condition 1 temperature maps and midline plot, 300 Hz

The entrainment of the coflowing air drops off dramatically at 300 Hz. The drop off in entrainment is illustrated in the centerline temperature plot. The midline temperature for each phase curve on the outer edges of the plot, from ±0.50 to ±0.60, collapses into one line, showing that bulk mixing of the air no longer occurs. The temperature is still higher at these outer points, and in general, than the unforced case, so there is still enhanced mixing at these positions and greater jet spread than the unforced case. Deep entrainment of the fuel, interestingly, still occurs, but no fuel pockets are pinched off as in 230-270 Hz forcing cases. This indicates that the forcing is moving away from the preferred mode of the outer jet, but still in the range for the center jet. In addition, forcing is only acting on the center jet, so effects from forcing from the speaker on the coflowing air are damped. The temperature is still generally higher than the unforced case, especially at 90^{o} phase. Decreased bulk mixing, increased small scale mixing, and longer residence time are thought to play a role in the higher temperatures.

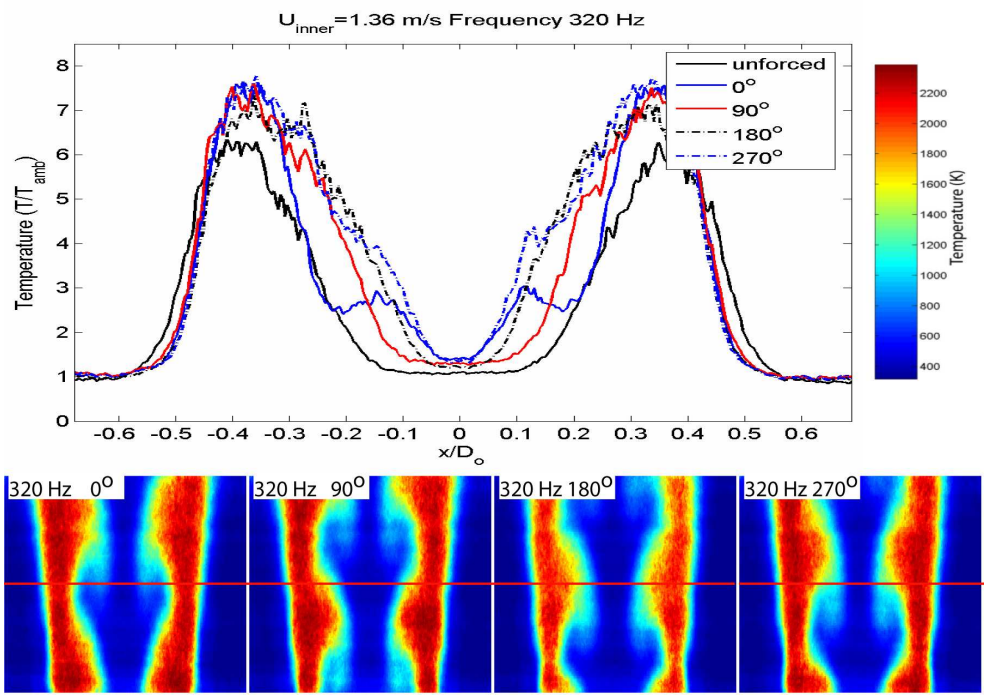

Figure 4-11 Flow condition 1 temperature maps and midline plot, 320 Hz

At 320 Hz, entrainment of the fuel jet into the high temperature region has decreased significantly, which indicates that the forcing has moved away from the preferred mode of the center jet. The plot of the temperature at the midline shows the temperature for all points in the forcing is near the unforced case from ±0.40 to ±0.50, although temperatures from ±0.40 and inward have a significantly higher temperature than the unforced condition.

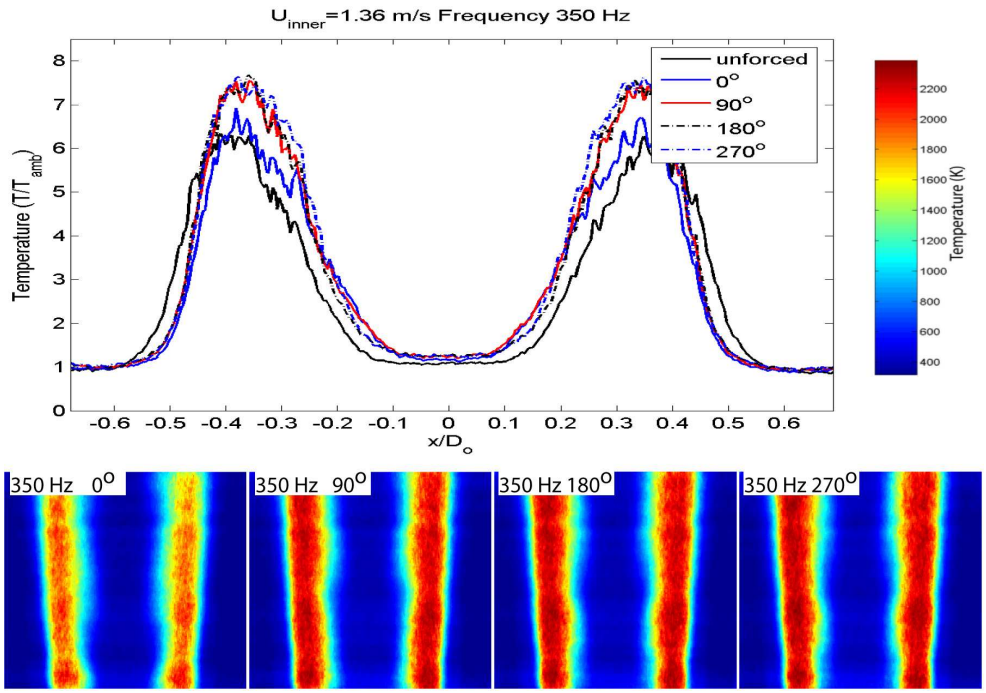

Figure 4-12 Flow condition 1 temperature maps and midline plot, 350 Hz

Bulk mixing at 350 Hz does not occur. The high temperature regions have nearly the same width as the unforced case. The peak temperature, however, is still higher than the unforced case, indicating that enhanced small scale mixing takes place. At 300 Hz, the vortices generated by the forcing may have started to stabilize at smaller diameters, resulting in decrease in the bulk mixing as concluded by Schadow in [3]. From 320 Hz to 350 Hz, the vortices also may have stabilized at the smaller diameters, keeping the width of the high temperature regions the same as the unforced case, but still enhancing mixing. The sudden decreases in temperature for 320 Hz at 150^o and at 350 Hz at 0^o cannot be explained. It is possible that a large particle had plugged up one of the orifices in the gas line, changing the gas composition

4.3.2 Flow Condition 2, Velocity U_{inner}=2.16 m/s, Velocity Ratio=1

The overall temperature of the unforced case for this condition is lower than flow condition #1, and the high temperature region is thinner, which is expected for a faster flow as molecular diffusion has less time to occur. Starting at the outside of the jet, the temperature of the unforced case begins to increase over ambient at ±0.50 and peaks at ±0.35 where $T/T_{amb} \approx 6.0$ before dropping to ambient near the center of the jet at ±0.15. Over most of the forcing conditions, the temperature distribution is lower than the corresponding frequency for the previous flow condition due to the apparently more intense vorticity generated, which was concluded from the more defined swirling observed in the high temperature region. At frequencies in the 300 Hz range the temperature distributions are similar to flow condition #1. Forcing overall is expected to be less effective since the amplitude of the forcing was not increased to accommodate the decrease in the fluctuating velocity to mean velocity ratio, but interestingly, fluid effects from forcing do occur and taper off earlier in the frequency range.

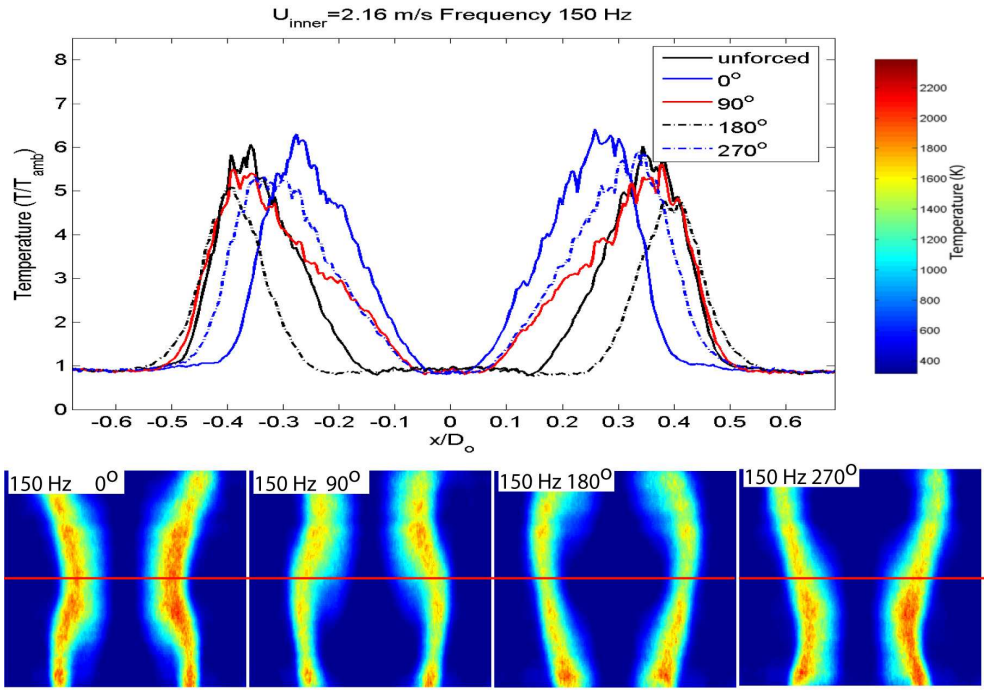

Figure 4-13 Flow condition 2 temperature maps and midline plot, 150 Hz

At 150 Hz forcing, there is essentially no change in temperature compared with the unforced case, as with the previous flow condition. Similarly, thick and thin high temperature regions are produced, shown on the midline plot at 90° and 180° respectively. The peak temperature for the 180° curve is lower than the peak for the unforced case, and the width of the high temperature peak is much thinner, showing the region is being strained or cooled. The other temperature curves have the same peak temperature as the unforced flame.

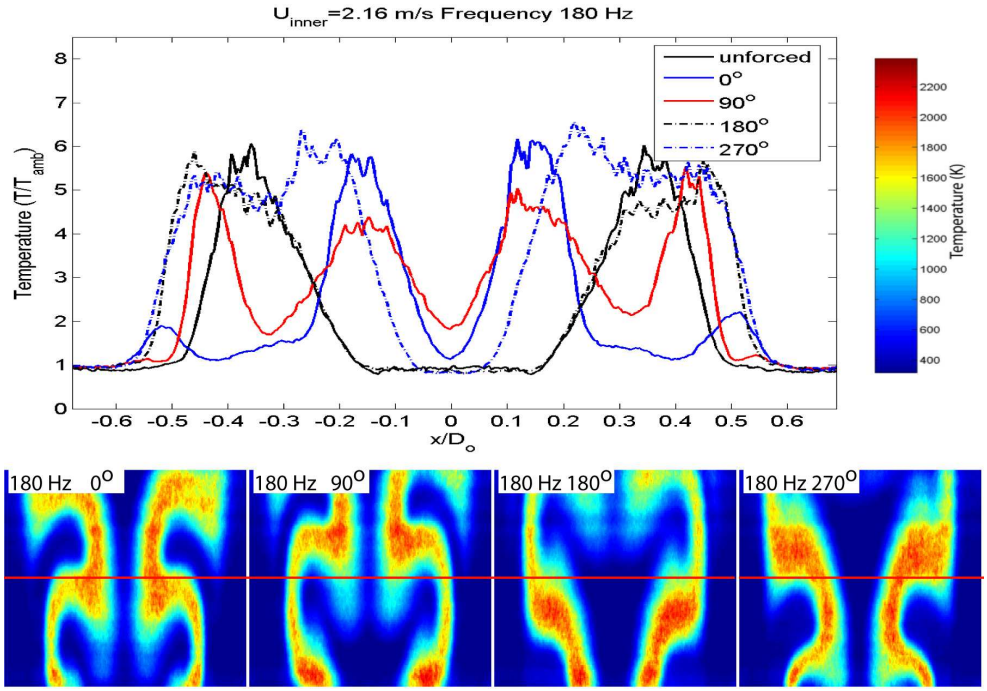

Figure 4-14 Flow condition 2 temperature maps and midline plot, 180 Hz

At 180 Hz , there is still no significant increase in temperature over the unforced case. Significant influence of the forcing over the large-scale fluid dynamics is observed, compared to the much weaker effects seen at this frequency for flow condition #1. The 270° image and 270° midline temperature shows much wider high temperature regions. These wide regions indicate improved mixing, probably from the longer residence time

allowing more intermixing of air and fuel. The broad high temperature region cools down as it moves upstream and entrains cooler gases, shown in the temperature maps from 270° to 0° (Appendix B.2). The entrainment of cool reactants reaches in much further into to the center jet than the previous flow condition, visible on the temperature maps and further illustrated by the deep decreases in temperature for 0° and 90°. Cool air is seen reaching in from ±0.40 to ±0.25 for the 0° curve and the fuel, now warmer, reaches out to ±0.30 on the 90° curve. Jet spread has also increased for this forcing as the jet temperature drops back to ambient at ±0.55. The vortices are seen already shearing and straining the reaction region, shown by the thin high temperature region at ±0.40 on the 90° temperature plot. On the temperature map, the thin region stretches out and thins from 90° to 180° as it moves downstream.

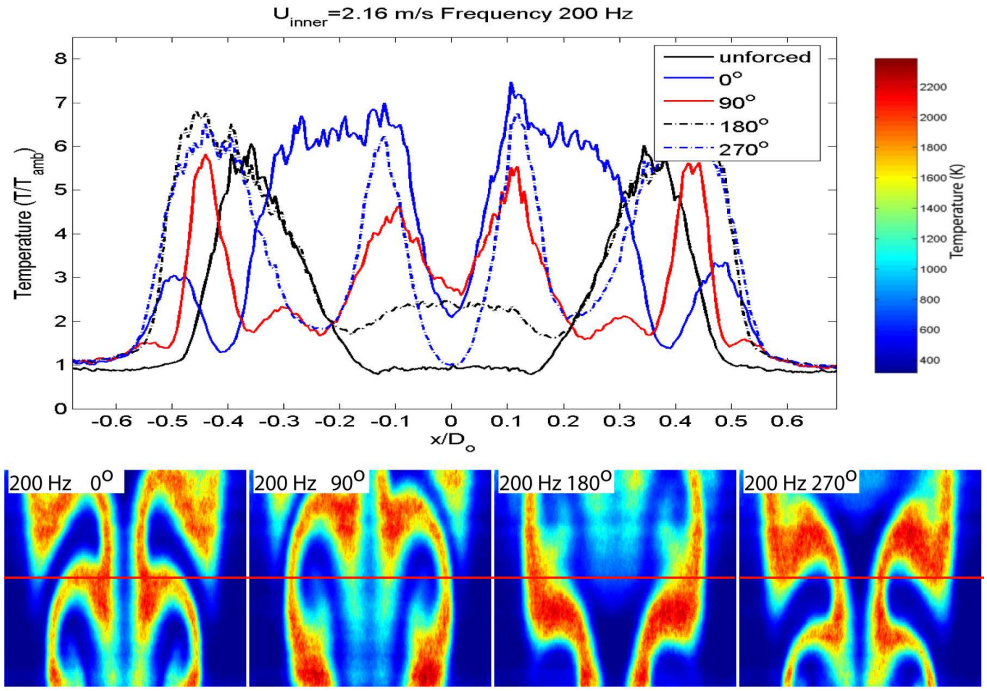

Figure 4-15 Flow condition 2 temperature maps and midline plot, 200 Hz

For forcing at 200 Hz, there are thick regions that have moderately higher temperatures than the unforced case. The 270^{o} phase temperature map also shows thick 'shoulders' of higher temperature, due to less straining and shearing in this region, presumably because it is between two large vortices, allowing diffusion and small scale mixing to enhance combustion. This region cools as it moves down stream, shown at the top half of the 0^{o} temperature map. An air pocket, seen at the bottom half of the 180^{o} map, is being entrained. As the air pocket moves upward, it begins to reach in further towards the center, thins and elongates more than the previous forcing case, indicating more intense vorticity. Unlike the previous flow condition, however, the pocket of air and fuel does not pinch off. The hot region of the flame between the outer edge of the entrained fuel and the inner edge of the entrained air becomes especially thin and cool. This thinning is observed, for example, by the narrowness of the peaks at ±0.45 in the 90^{o} midline temperature curve. Some interesting features in the 90^{o} temperature curve are observed. There are temperature dips at ±0.25 and ±0.35 and a small peak at ±0.30. This phenomenon is the swirling of cooler fuel into the hot region, clearly seen in the corresponding temperature map. Swirling is also observed in the 270^{o} curve where the temperature dip at ±0.20 is air moving up into the hotter region. Forcing at 230 Hz produces very similar effects and the 270^{o} curve shows a wide region of temperature that is significantly higher than the unforced case.

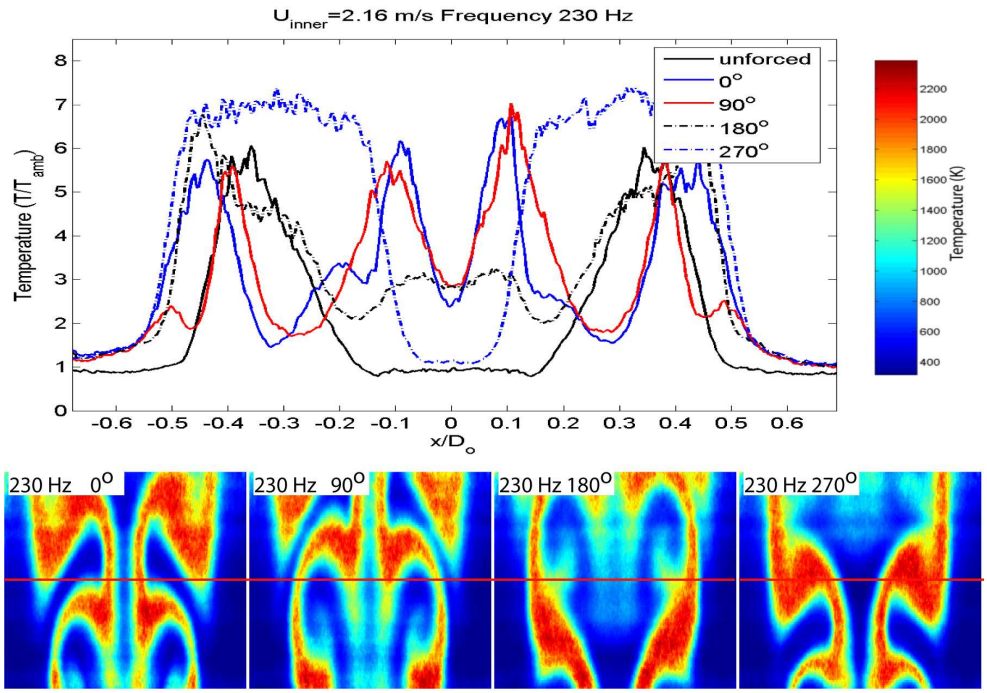

Figure 4-16 Flow condition 2 temperature maps and midline plot, 230 Hz

Overall, flame temperature appears to increase at 250 Hz. This temperature increase is due to two reasons. Both the entrainment of the cooler gases into the hot regions and the vorticity strength has decreased; the branches of cool air and fuel do not reach as far into the hot regions as before. Small scale mixing may have increased due to the increased frequency as well. Jet spread from 200 Hz to 250Hz is nearly equal, about 20% wider than the unforced case. However, the temperature drop of the jet is steepest and occurs the furthest out from the center for the 250 Hz forcing.

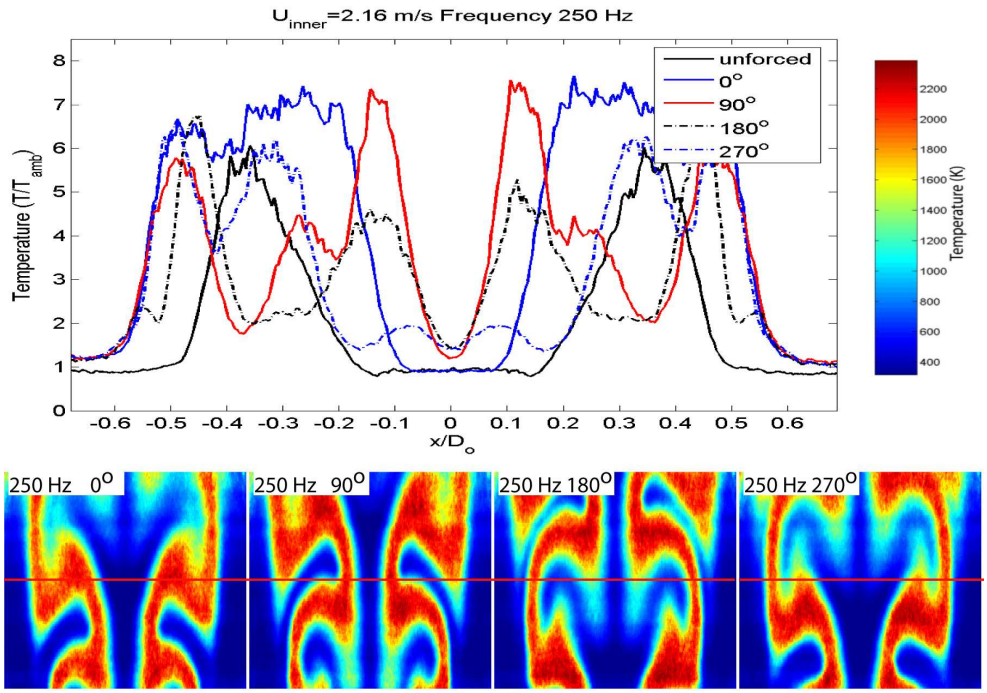

Figure 4-17 Flow condition 2 temperature maps and midline plot, 250 Hz

Bulk effects drop off considerably at 270 Hz, although at this frequency, entrainment of air is still easy to see, unlike in flow condition #1. The entrained fuel here only reaches out to ±0.25 and the jet spread for this forcing case is approaching the width of the unforced case. Therefore the preferred mode of the jet is somewhere between 180 Hz to 250 Hz. The temperature for this forcing is significantly higher than the unforced condition. The increase in temperature can be attributed to decreased entrainment of the cooler gases competing with the small scale mixing enhancement.

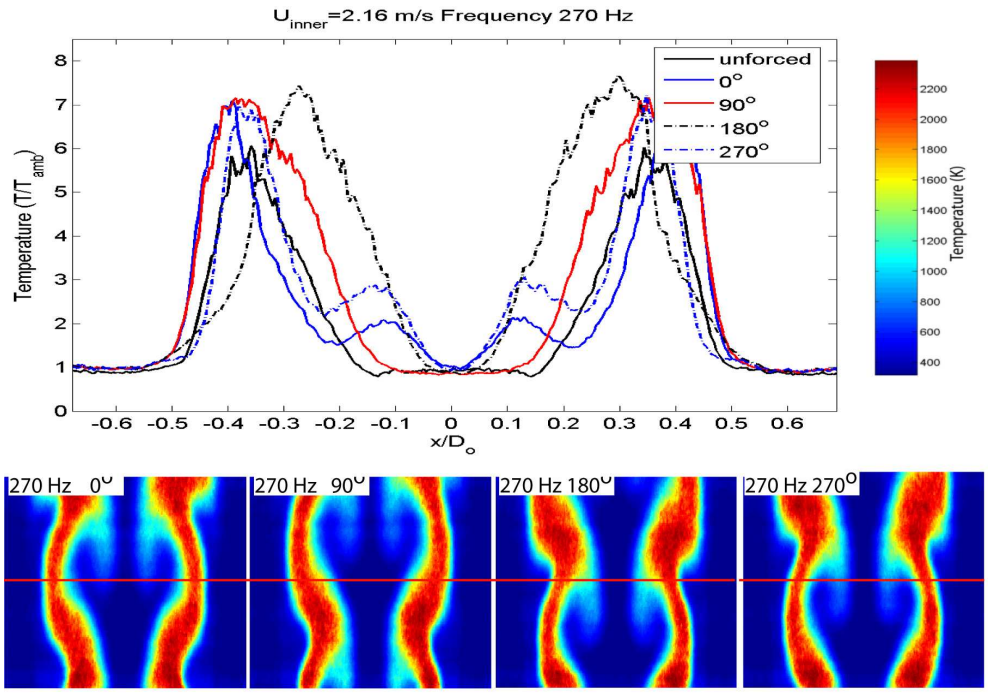

Figure 4-18 Flow condition 2 temperature maps and midline plot, 270 Hz

At 300 Hz, the shape of high temperature regions looks simply wavy. There is still a small amount of vortical entrainment of fuel, shown by small swell in the 90° phase temperature curve at ±0.20. The width of the peaks of the temperature curves are equal to the unforced case for 320 Hz and 350 Hz forcing. The temperature distribution at 320 Hz and 350 Hz appear identical, and as if without any forcing, since bulk effects do not occur. The peak temperatures of the 300 Hz to 350 Hz forced flame are all 30% greater than the unforced case, suggesting that small scale mixing is the primary mechanism for combustion enhancement for these forcing frequencies.

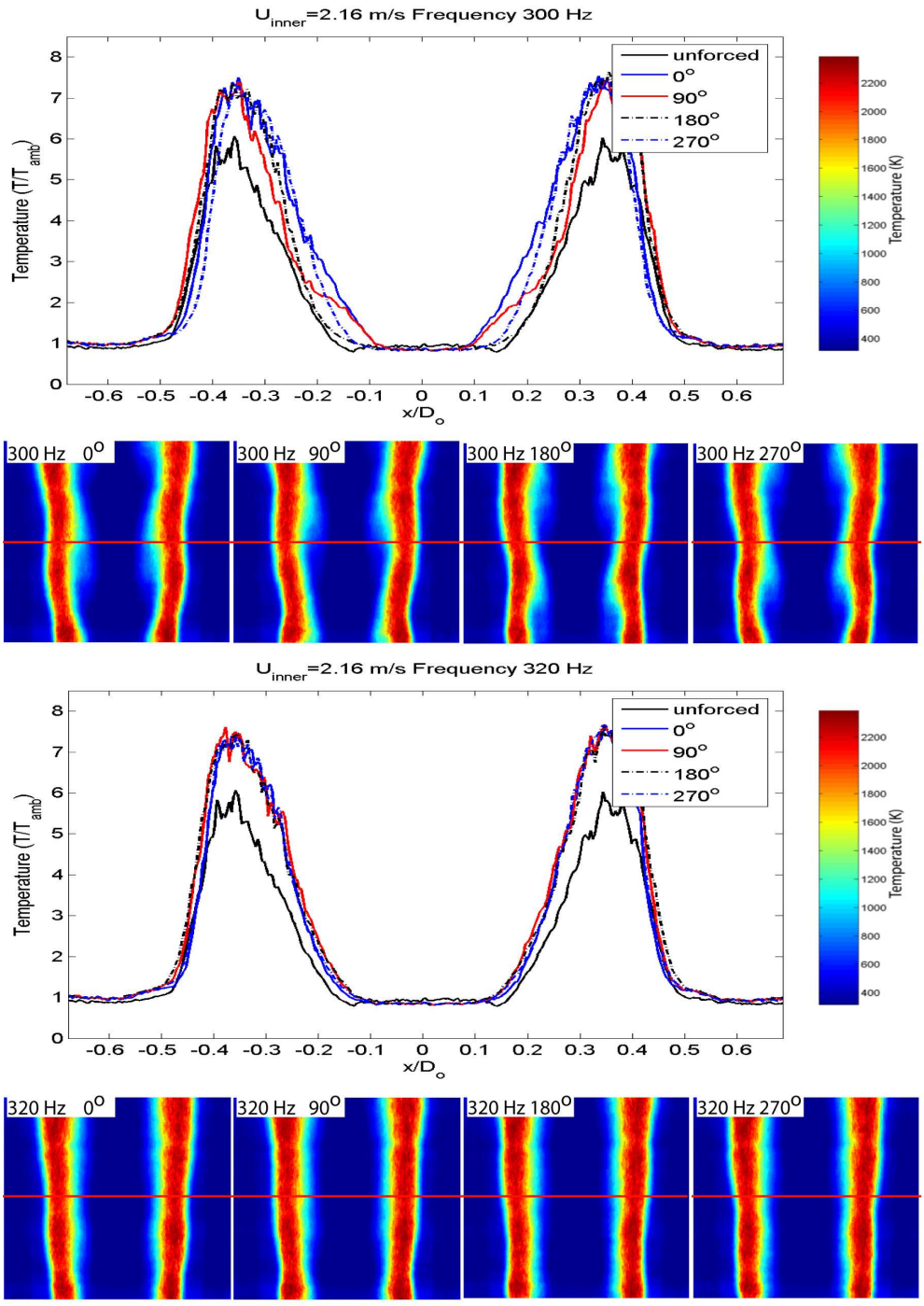

Figure 4-19 Flow condition 2 temperature maps and midline plot, 300 Hz & 320 Hz

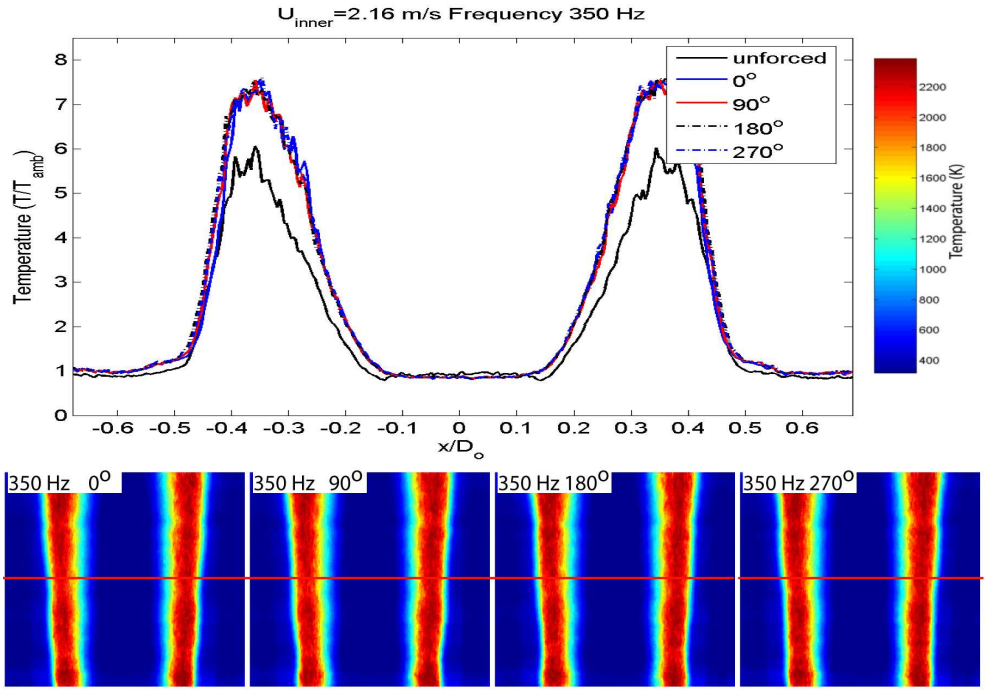

Figure 4-20 Flow condition 2 temperature maps and midline plot, 350 Hz

4.4 Flow Condition 3, Velocity Ratio V_r=2

This condition introduces a shear component to the flow. The unforced temperature distribution is similar to flow condition #1. From the air stream moving inward toward the jet, the temperature increase starts at ±0.45, peaking at ±0.30 where $T/T_{amb}\approx6.0$, and decreasing to ambient at ±0.10. Similar to earlier cases, forcing at 150 Hz produced passing thick and thin hot regions. There was no increase in flame temperature or in jet spread over the unforced condition. Qualitatively though, features on the air side of the flame appear more angular, because of the shear flow, than the previous two flows.

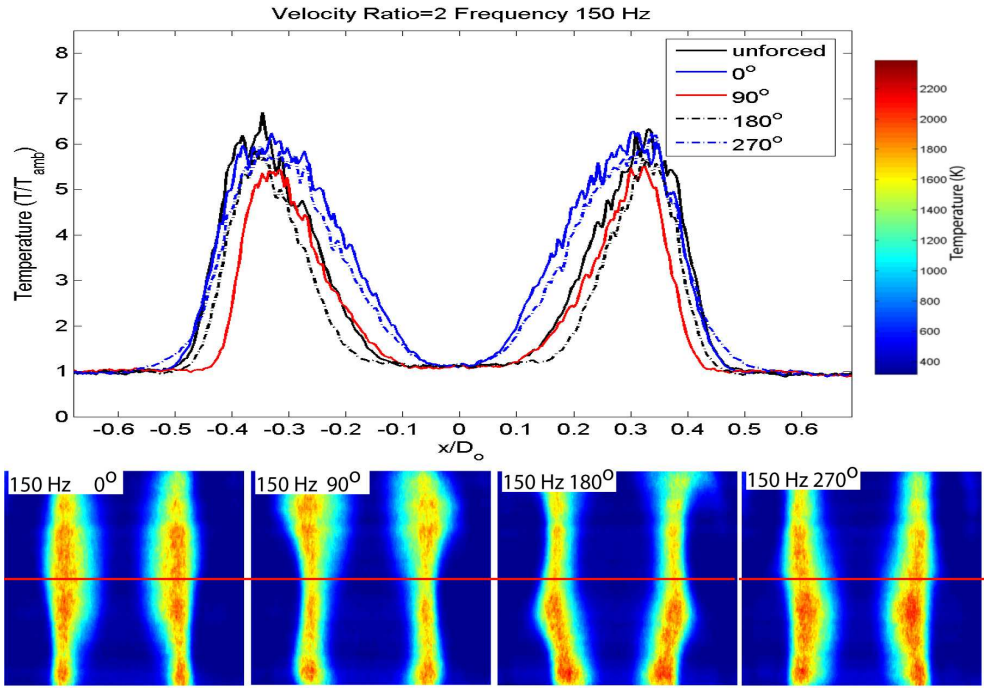

Figure 4-21 Flow condition 3 temperature maps and midline plot, 150 Hz

Forcing at 180 Hz does generate higher and wider temperature peaks then the unforced case, shown by the 0^o and 90^o curve on the midline plot. A thin region of the flame is shown by the 180^o curve, where the peak width is thinner than the unforced peaks but is still approximately the same temperature. At this frequency in flow condition #1, the peak temperature was 30% greater than the unforced condition. The shear flow is interfering with the small-scale mixing enhancement, by mixing in the cooler air into the flame or inhibiting mixing. The shear flow also appears to be interfering with the formation of the fluid structure seen in flow condition #1. The 180^o and 270^o curve show cool air pushing into ±0.40, where air was only reaching ±0.55 for the first flow condition.

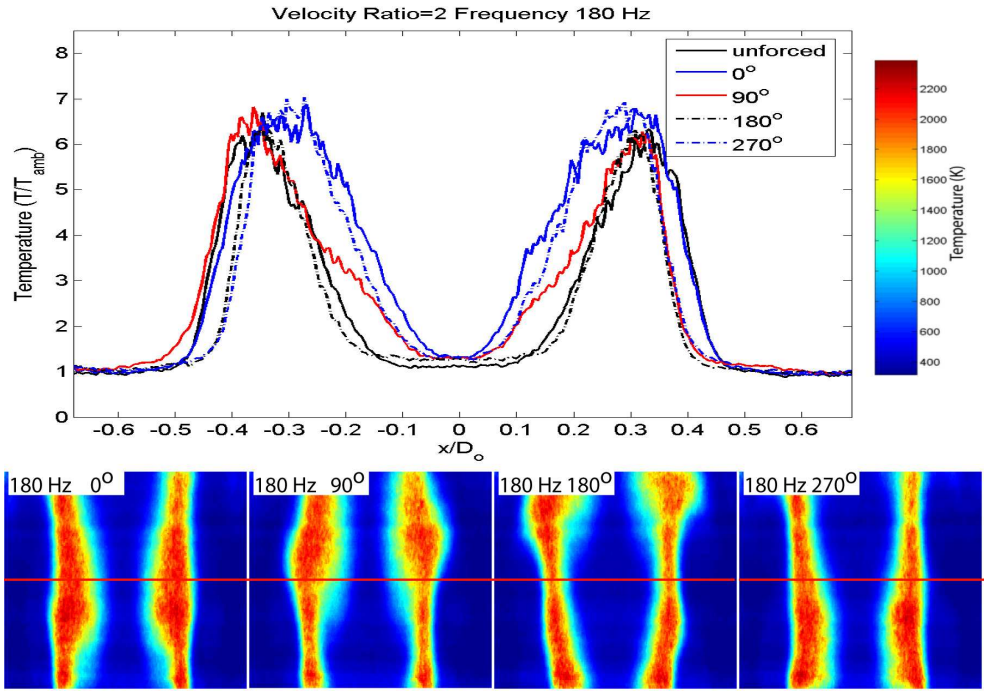

Figure 4-22 Flow condition 3 temperature maps and midline plot, 180 Hz

Influence from increased entrainment of cooler gases is seen at 200 Hz. Temperature remains close to the unforced condition, though the 270° phase shows a small increase. The dips in the 90° curve at ±0.25 show cool fuel being drawn outward into the high temperature region. The high temperature region progressing through 180° to 330° (See Appendix B.3) on the temperature maps cool down as they move upstream, images form 0° to 150° due to the continued entrainment of cool air. The temperature map for this case looks like an upside-down, and cooler, version of the temperature map for flow condition #1 at 200 Hz.

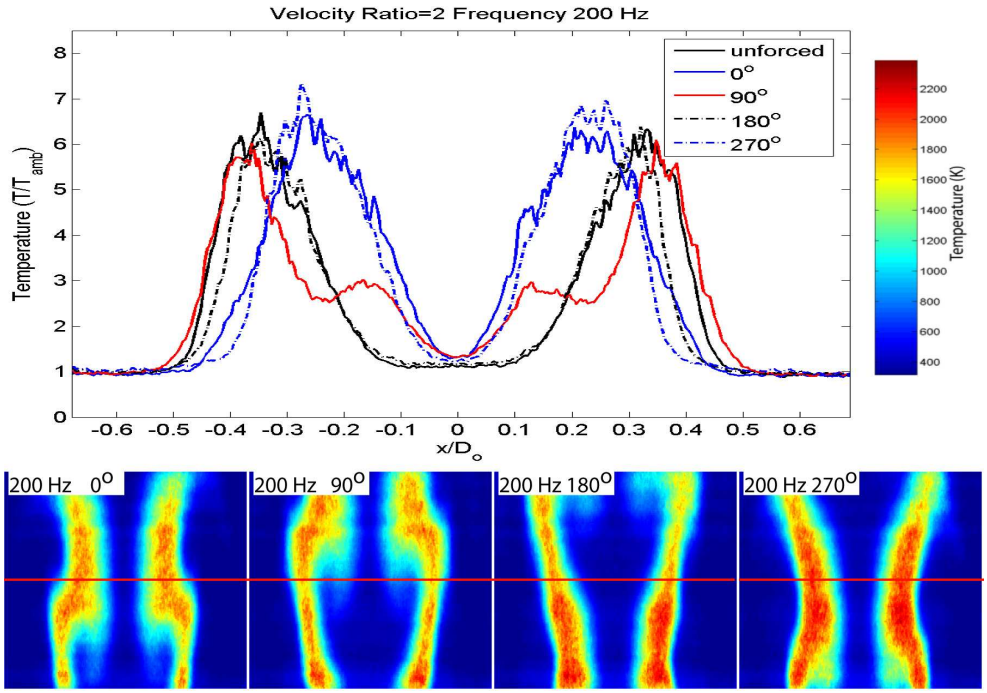

Figure 4-23 Flow condition 3 temperature maps and midline plot, 200 Hz

The preferred mode of this flow lies between 230 Hz and 300 Hz, a range similar to flow condition #1. The shape of the temperature maps, however, looks closer to flow condition #2, with the same swirling, straining, and shearing influences from the vortices, although not to such a high degree. The wide 'shoulder' regions associated with temperatures higher than the unforced case are observed as well. At 230 Hz, a deep entrainment of air is observed, corresponding to the 270° phase curve, where near ambient temperature air reaches into the jet as far as ±0.3. Dips in the 90° curve at the same location represent fuel being entrained and heated up. 0° and 180° phase midline plots show thick high temperature regions. For this flow and forcing condition, a distinct asymmetry in the jet is imaged. At x/D_o=–0.2, a depression in the 0° temperature curve illustrates air being swirled in, but this is not observed at x/D_o=+0.2. 250 Hz forcing shows even further entrainment of ambient temperature air, stretching to ±0.20, shown by the 270° phase curve and visible in the temperature maps. The 0° temperature curve

illustrates an unburned fuel pocket pinching off. 270 Hz forcing produces generally the same result, but with much less symmetry.

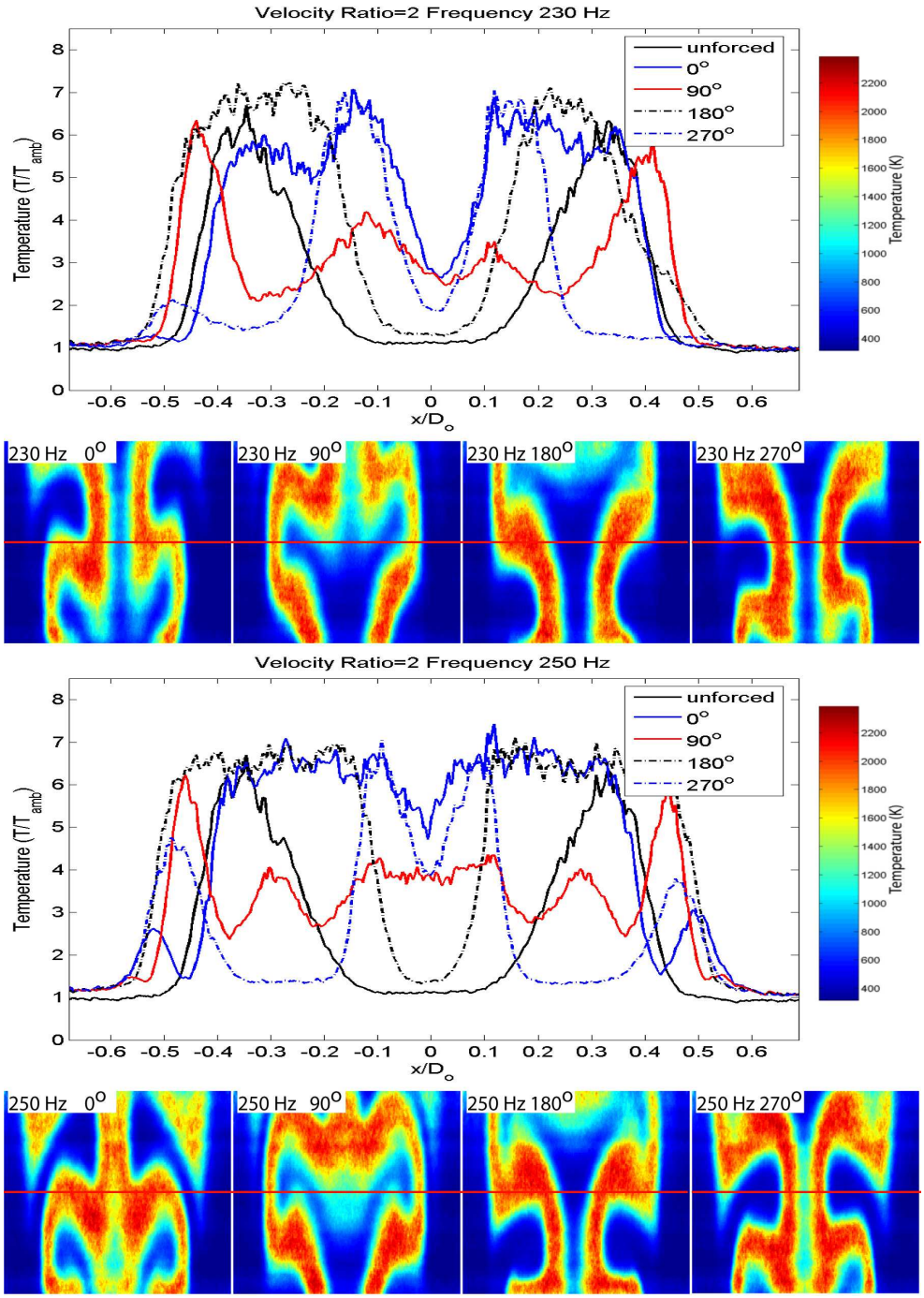

Figure 4-24 Flow condition 3 temperature maps and midline plot: 230 Hz & 250 Hz

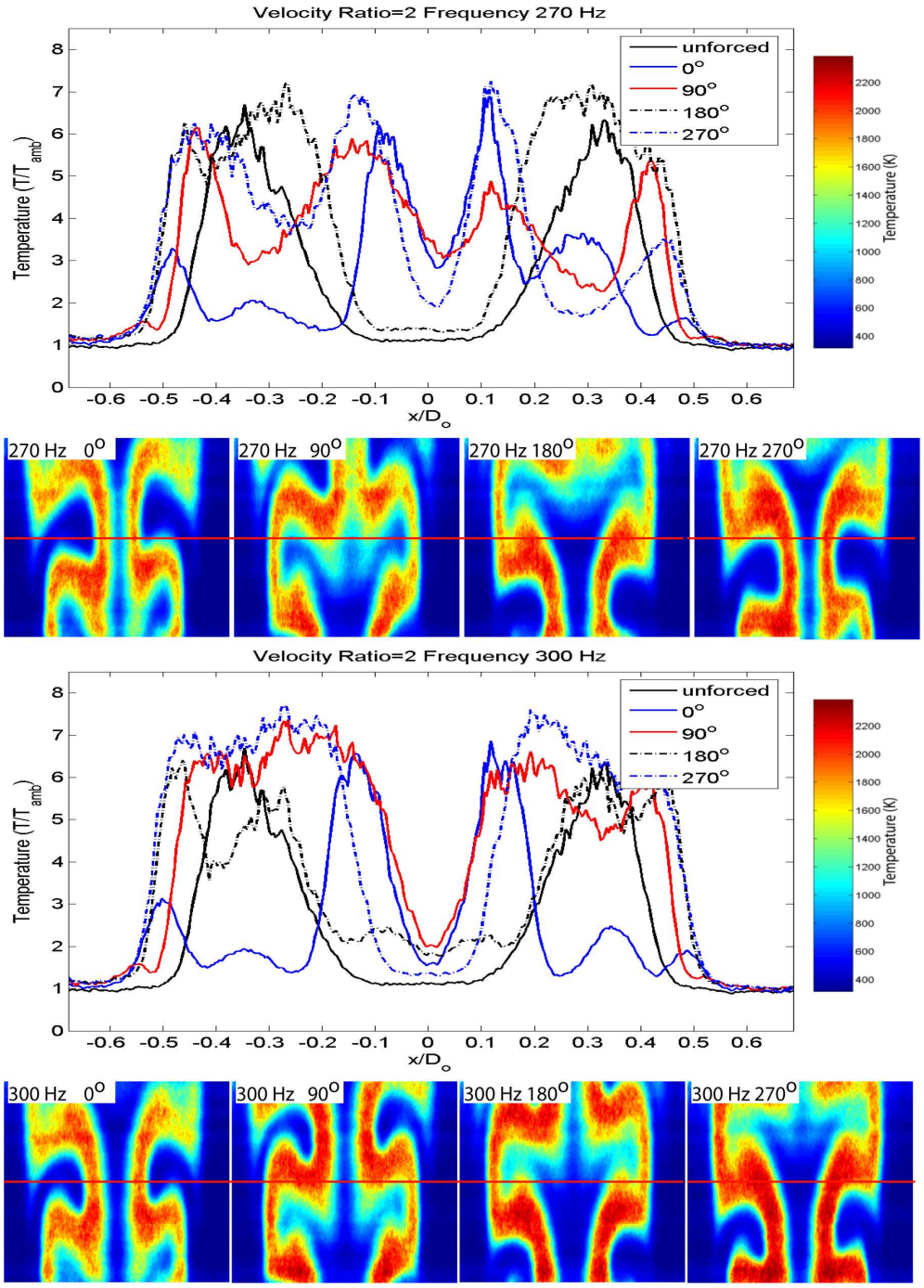

Figure 4-25 Flow condition 3 temperature maps and midline plot: 270 Hz & 300 Hz

300 Hz forcing is the first and only forcing frequency in flow condition #3, which produces a significant increase in flame temperature. The two dips in the 0^o curve, at ±0.25 and ±0.40 reflect how the cold air pocket swirls into the hot regions and shows a

decrease in entrainment for the air. Fuel entrainment, however, is highest at this forcing, reaching to ±0.40 x/D_o.

The air pockets that are entrained into the flame at 230 Hz to 300 Hz have some interesting characteristics. The cold air that is entrained for the same frequencies in flow condition #1 reaches inward, and the tip of the pocket is pointed. In flow condition #2, the end of the cold air pocket resembles a bulb. In this flow condition, the air pocket the air pocket resembles a bulb, but is much wider, as it reaches into the high temperature region. For flow condition #2 and #3, the air pockets are wide enough to be pulled in different directions by neighboring large scale vortices, where for flow condition #1, the air pocket may only wrap itself around one vortex.

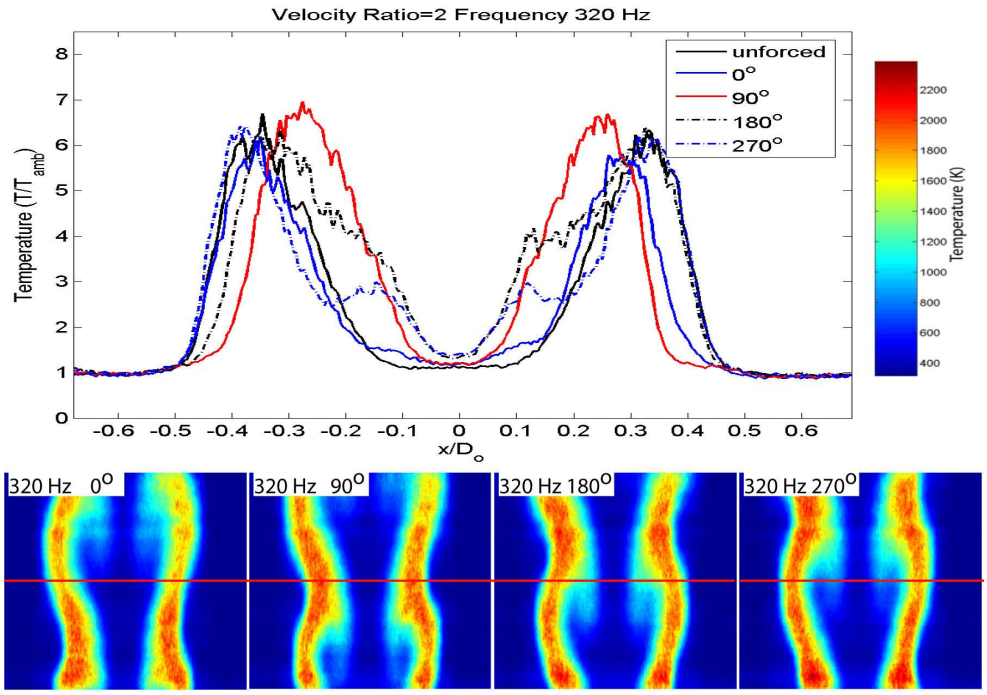

Figure 4-26 Flow condition 3 temperature maps and midline plot, 320 Hz

At 320 Hz, forcing is no longer in the preferred mode of the jet. There is little increase in temperature and the flame mostly just becomes wavy. At 350 Hz, the

temperature distribution appears as if no forcing was occurring, even the temperature remains the same as the unforced case. For the first two flow conditions, the flame temperature was significantly increased at these high frequencies, but this does not occur in flow condition #3. The shearing of the coflow is competing with the small-scale mixing enhancement from the speaker, either by mixing in cool air, or preventing the roll up of small vorticies.

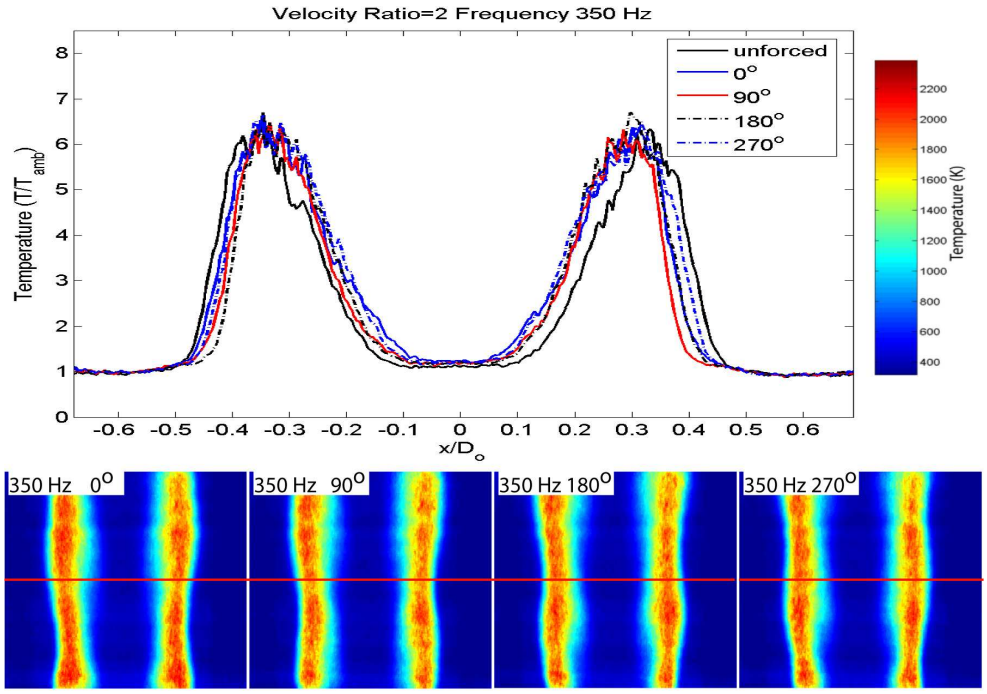

Figure 4-27 Flow condition 3 temperature maps and midline plot, 350 Hz

4.5 Flow Condition Four, Velocity Ratio V_r=0.5

At this flow condition, the flame became very sensitive to cross breezes in the room, even despite acoustic forcing. It became very difficult to take fifty images without substantial bulk motion of the flame. The unforced temperature distribution is very similar to flow condition #1. At 150 Hz forcing, the effects are similar to the other flow conditions at this forcing frequency as well. Forcing from 300 Hz to 350 Hz showed a

small increase temperature over the unforced case. The midline temperature curves for each frequency at each degree increment do show a slight increase in jet spread. This indicates that the shearing from the slower outer flow decreases the effectiveness of the forcing.

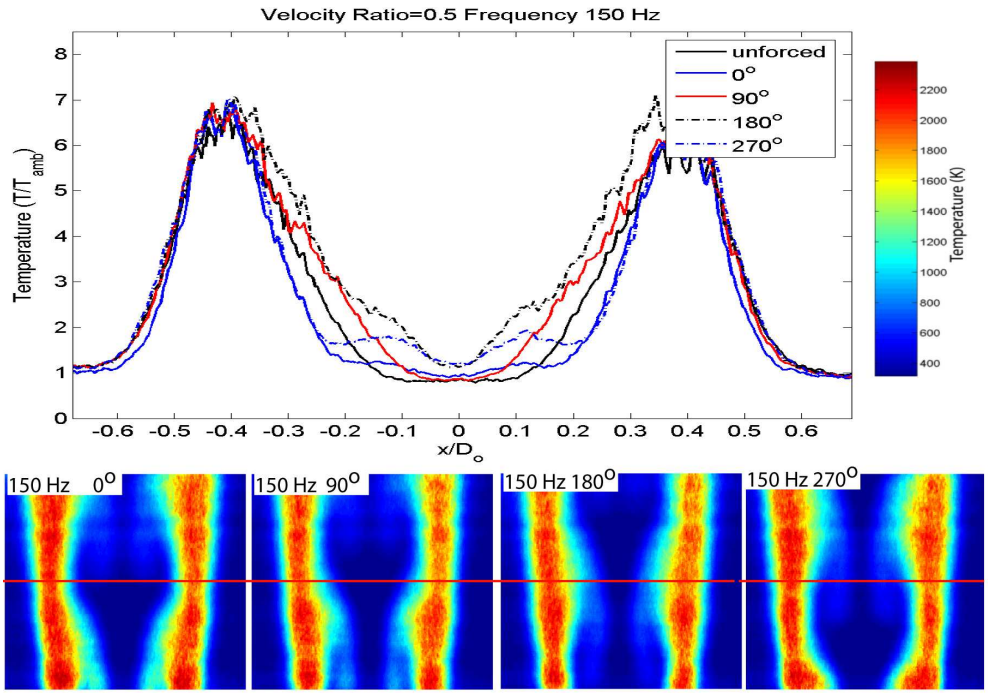

Figure 4-28 Flow condition 4 temperature maps and midline plot, 150 Hz

For frequencies between 180 Hz and 270 Hz, the flame collapses into a turbulent mode. The flame shape became largely independent of the forcing as evidenced by the lack of structure in the temperature maps. The flame also became much noisier, louder than the sound produced by the speaker, and prone to lift off. A few images of the flame in the turbulent mode is shown below, Figure 4-29. The onset of turbulence can be traced to flame-acoustic coupling. The temperature distributions of the corresponding forcing frequencies compared with the baseline case show fresh reactants being drawn deep into and surrounded by the flame. For this flow condition the flame quickly consumed the

enveloped reactants, creating a pressure fluctuation that coupled with the burner acoustics, leading to self sustained pressure fluctuations. It can be assumed that the preferred mode of the jet is in this frequency range, similar to the preferred mode frequency range for flow condition #2.

Figure 4-29 Self-induced flame instability for flow condition 4

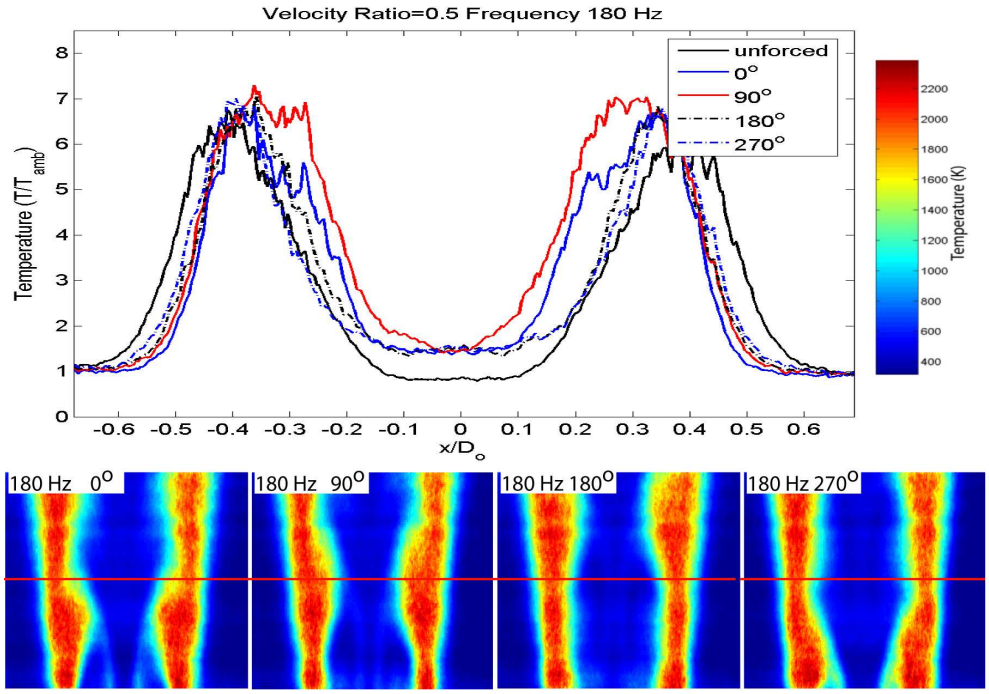

Figure 4-30 Flow condition 4 temperature maps and midline plot, 180 Hz

Conclusions can still be drawn from the midline temperature plots and the temperature maps even though the flame was unsteady. At 200 Hz and 230 Hz, there

appears to be entrainment of products into the core of the fuel jet. The midline temperature curves for the 200 Hz and 230 Hz forcing conditions shows an increase in temperature over the ambient temperature at the centerline of the jet, x/Do=0. For 180 Hz and 250 Hz forcing conditions, there is less entrainment of cooler gases, indicated by the midline temperature curves, where the center jet temperature is lower than in the 200 Hz and 230 Hz forcing cases. The temperature curves for 180 Hz and 250 Hz show marginally higher temperature then the unforced case, which suggests less entertainment of surrounding gases to cool the flame. The midline temperature plot for the 270 Hz case shows the forcing frequency is moving way from the preferred mode of the burner as the temperature curves begin to closely resemble the unforced temperature distribution.

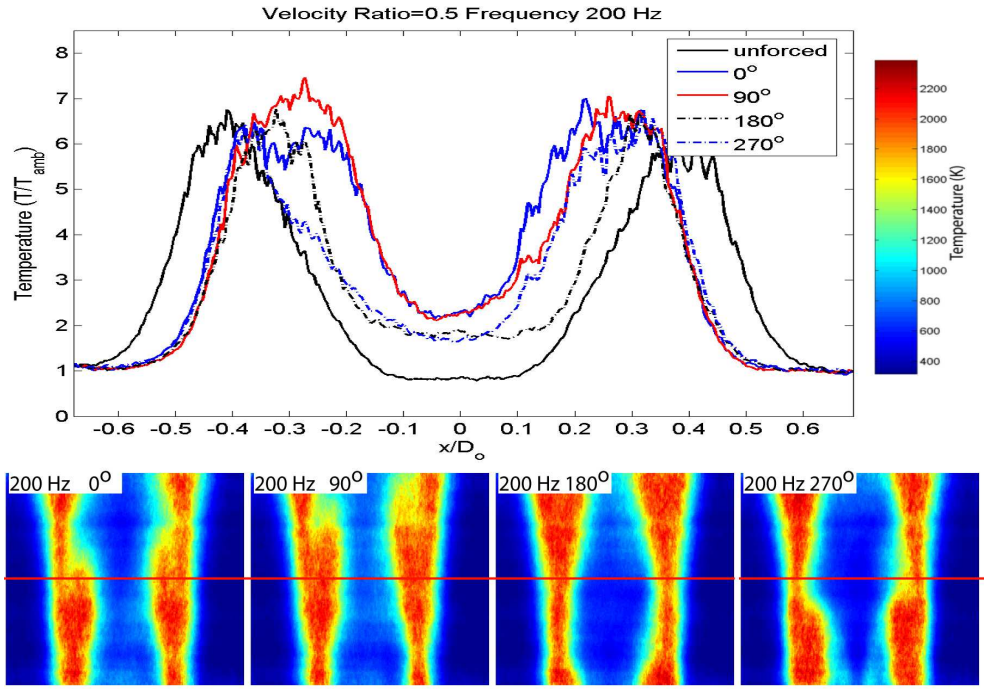

Figure 4-31 Flow condition 4 temperature maps and midline plot, 200 Hz

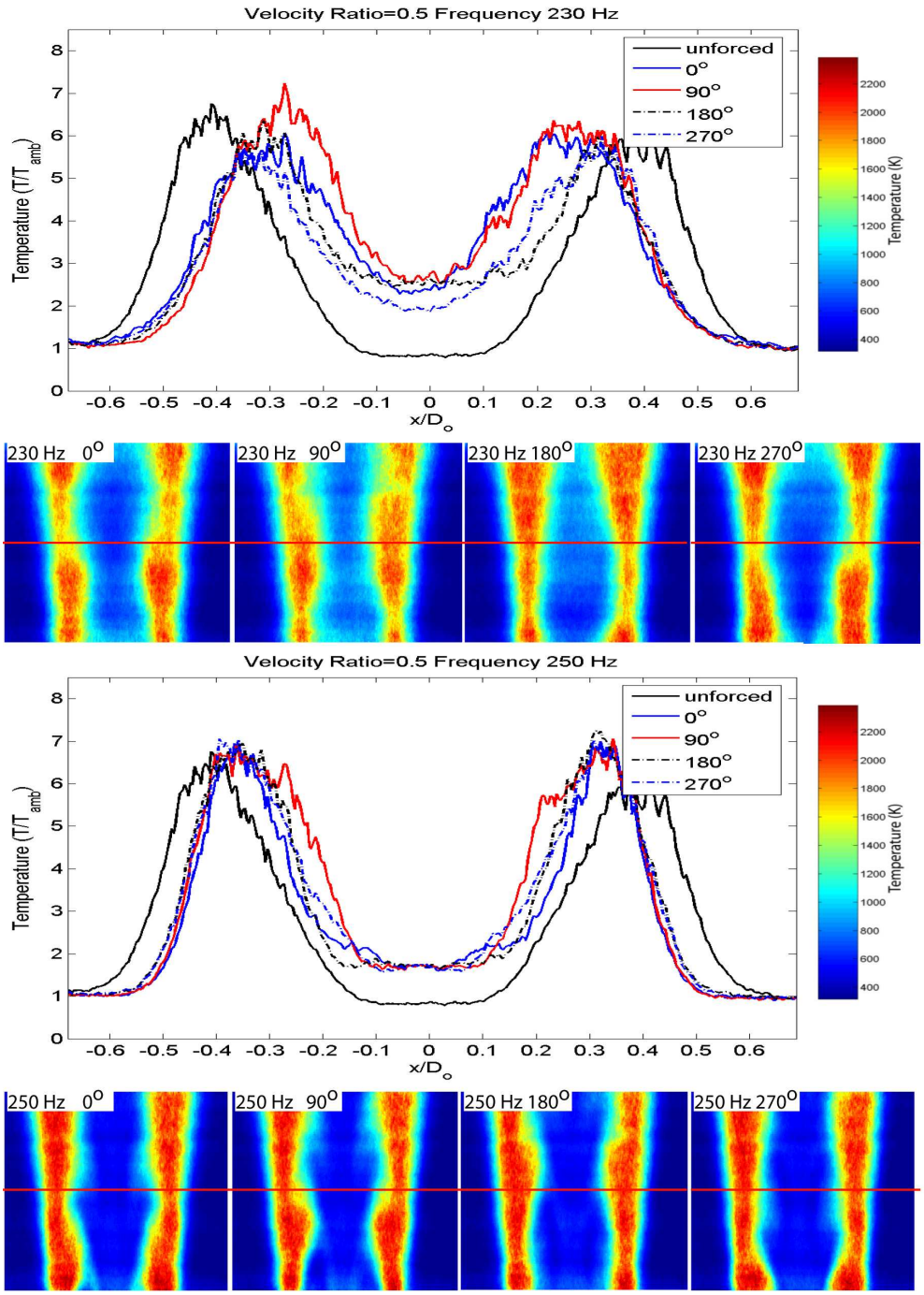

Figure 4-32 Flow condition 4 temperature maps and midline plot, 230 Hz & 250 Hz

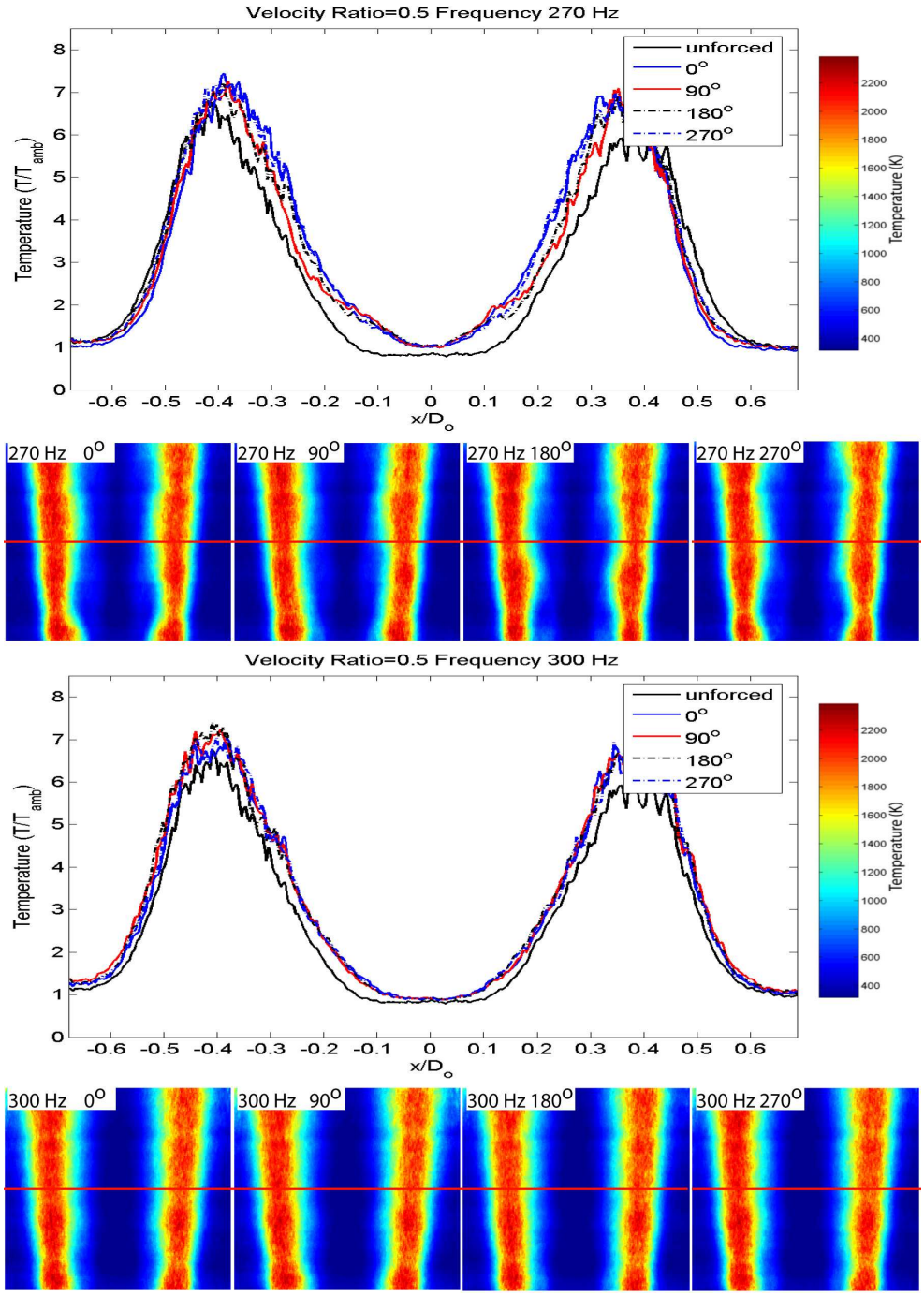

Figure 4-33 Flow condition 4 temperature maps and midline plot, 270 Hz & 300 Hz

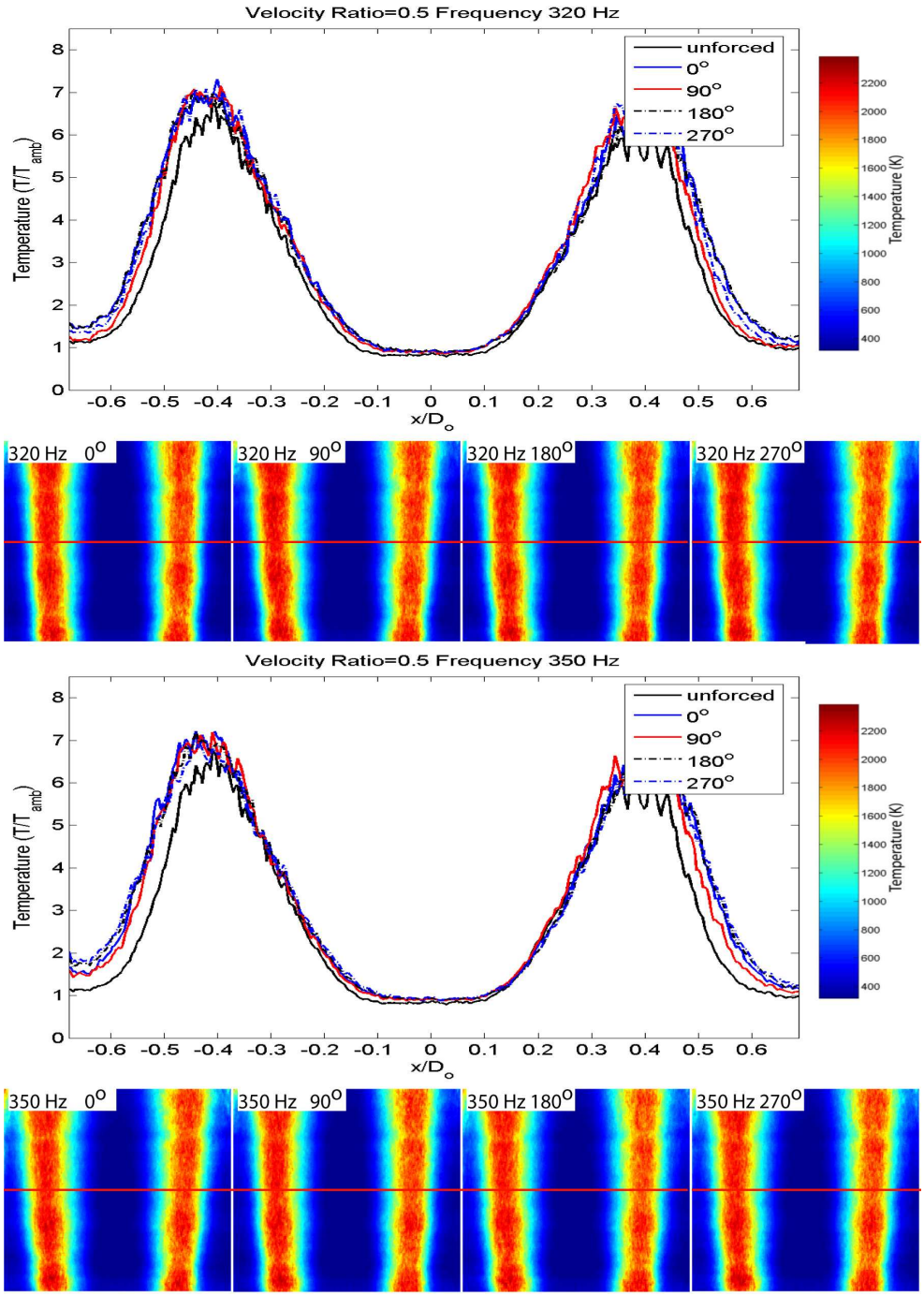

Figure 4-34 Flow condition 4 temperature maps and midline plot, 320 Hz & 350 Hz

4.6 Error

There are a few sources of error that need to be quantified to assess the accuracy of this imaging technique. Errors due to a change in the Rayleigh cross-section of the gas and errors due to misalignment of the calibration images are two major contributors to the uncertainty. These errors generally result in changes in intensity of the signal, as do other errors.

It is well known that the cross-section of the gas mixture changes a small amount during combustion. Other changes in the cross-section result from errors in the delivery of the gases, changing the composition of the flow. The methane and hydrogen are both zero grade, so for the most part they are pure. The air supply line is dried and filtered, however at one point, oil was found in the supply line as a result of a clogged filter and flooded compressor. This may have introduced some impurities into the flame. Maintaining the pressure was also difficult. Gas bottle regulators cannot finely control the pressure; consequently, a small turn in the knob can change the pressure significantly. Pressure fluctuations from adjusting the regulator also take time to propagate through the system and can change the flow composition. Careful observation, adjustment, and a dose of patience can keep the pressure, as read by the Setra transducers, with in 0.2psi. The effect of the error in the pressure on the cross section was determined to be at most 2%, determined by varying the pressure inputs in the MathCad program by a small amount. However, the H_2 and CH_4 are introduced into the burner through two different lines, giving only the length of the center tube to mix. The mixing between the two gases may not have been sufficient.

The alignment of the burner with the camera and laser can be a source of error. Obtaining the calibration images involved disassembling the burner and moving the camera. Although care was taking into reassembly, changes in position of the burner, laser sheet, and camera will result in scattering noise being recorded in the wrong locations on the ICCD chip or apparent change the scattering geometry. To estimate the error as a result of misalignment, the standard deviation of the $\overline{I_{amb}} - \overline{I_{He}}$ term was divided by the mean value, yielding an estimated error of 5.1%

The recorded intensity can vary as well. Shot to shot variations in the laser sheet intensity, uniformity, and electronic noise associated with the ICCD are sources of these variations. Assuming a random or normal distribution in intensity fluctuations, these errors should average out. Changes in the cross-section due to composition fluctuations will also manifest themselves as deviations from the theoretical intensity.

Errors in the intensity will preferentially cause the temperature to be calculated too high. As the $\overline{I_t} - \overline{I_{He}}$ term in the denominator of Equation 3-5 approaches zero, the calculated temperature asymptotically increases. As errors accumulate, for example if for a particular pixel, the $\overline{I_t}$ is particularly low and the corresponding $\overline{I_{He}}$ pixel is particularly high, the difference can drop to zero or become negative, making the calculation approach infinity or produce a negative number, a non-physical value. Pixels where $\overline{I_t} - \overline{I_{He}}$ is negative are assigned a small positive value. Pixels where $\overline{I_t} - \overline{I_{He}}$ are very small the calculated temperature is limited to the physically realistic value of 2350K or below. This approximation is reasonable since in a diffusion flame, fuel and oxidizer diffuse together in stoichiometric proportions, resulting in flame temperatures

approaching the stoichiometric adiabatic flame temperature [52]. The adiabatic flame temperature for this mixture was calculated to be 2290 K by Gaseq, a thermal equilibrium program, with reactants starting at 300 K. 2350 K was selected to allow for locally higher flame temperature due to reactant heating. The percentage of pixels that are replaced is a concern in some cases. In most cases, pixel replacements do not exceed 12% and are generally restricted to the upper and lower edges of the high temperature regions of the measurement area, where laser intensity much less or where there was dust on the collecting optics. The extreme case is in flow condition #1 at 230 Hz at 330^{o} phase where 46.2% of the pixels were replaced; in this condition there was an aberrantly low signal. For flow condition #1, 230 Hz -300 Hz forcing cases replacement higher than 20%, also representing unusually low signal. The condition which sees the least amount of pixel replacement is flow condition #2, with 0.5% replacement. Tables containing the percent of pixels that are replaced for each frequency and phase angle are given in Appendix E.

The ambient temperature was always assumed to be 300K and the atmospheric pressure was also assumed constant, also introducing small errors. The lowest barometric pressure recorded for the days during the testing was 29.86 inches Hg and the highest was 30.48 inches Hg. The pressures corresponded to a difference of at most 1.8% from the pressure recorded on the day the ambient images were taken, 29.95 inches Hg to 30.16 inches of Hg [53]. Canceling out the gas constant and Avagodro's number and solving for T, Equation 3-4 reduces to the following.

$$T = T_{amb} \frac{(CI_o)}{(CI_o)_{amb}} \frac{P}{P_{amb}} \frac{\sigma_r}{\sigma_{amb}} \frac{\overline{I_{t,amb}} - \overline{I_{He}}}{\overline{I_t} - \overline{I_{He}}}$$

Equation 4-2 Temperature as a function of recorded intensity and other factors

The incident light and calibration constant ratio, pressure ratio, and cross-section ratio can be varied according to their contributing error along with the ambient temperature to obtain an upper and lower bound to the total error. Assuming the ambient temperature, then, is 300 K±5 K, a response curve for a pixel is shown in Figure 4-35. The upper bound was determined using $(CI_o)/(CI_o)_{amb} = 1.05$, $(P)/(P_{amb}) = 1.02$, $(\sigma)/(\sigma_{amb}) = 1.02$, and T_{amb}=305 K, which corresponds to an error of 12.1% . Using $(CI_o)/(CI_o)_{amb} = 0.95$, $(P)/(P_{amb}) = 0.98$, $(\sigma)/(\sigma_{amb}) = 0.98$, and T_{amb}=295 K an upper error limit of 11.3% is calculated

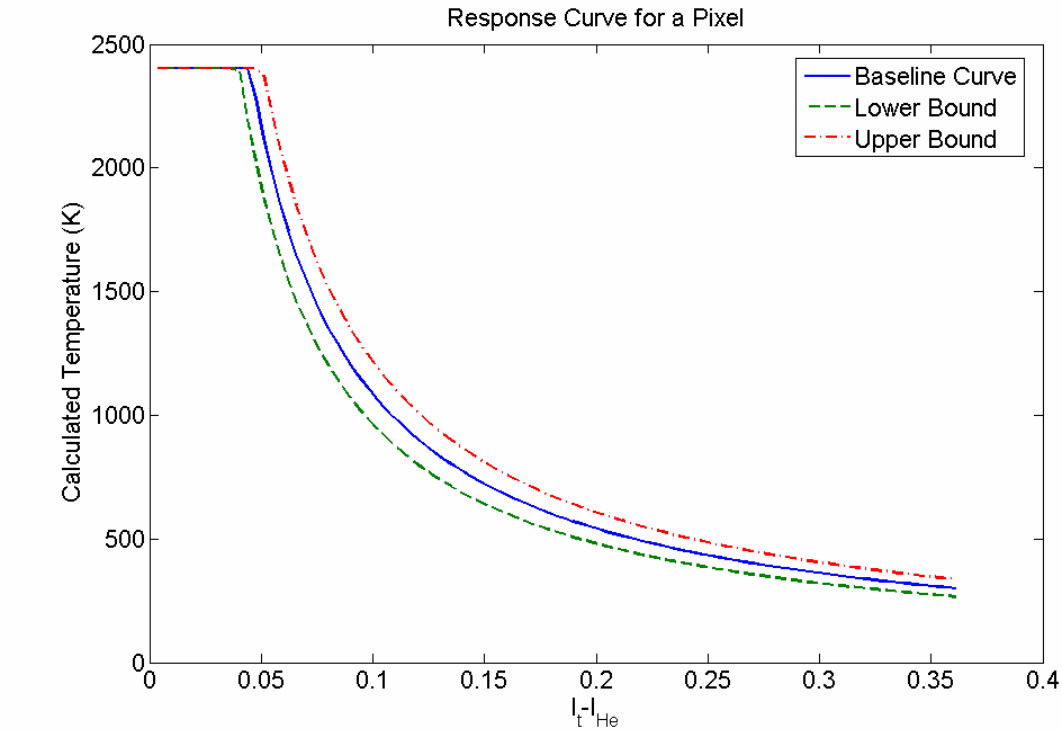

Figure 4-35 Response curve for a pixel with error bounds

There are a few other potentially significant sources of error, such as fluctuations in the phase of the passing fluid structures. Between fifteen and thirty-five oscillations occur between each camera shot. This gives ample time for the phase to change, either

from degradation in the speaker, changes in the gas properties, or other random perturbations. These deviations are averaged in to the images used in the data processing, which in unsteady portions of the structure are washed out. The standard error of each image is and indicator of the certainty in the average. A few of the standard error maps are shown in Figure 4-36.

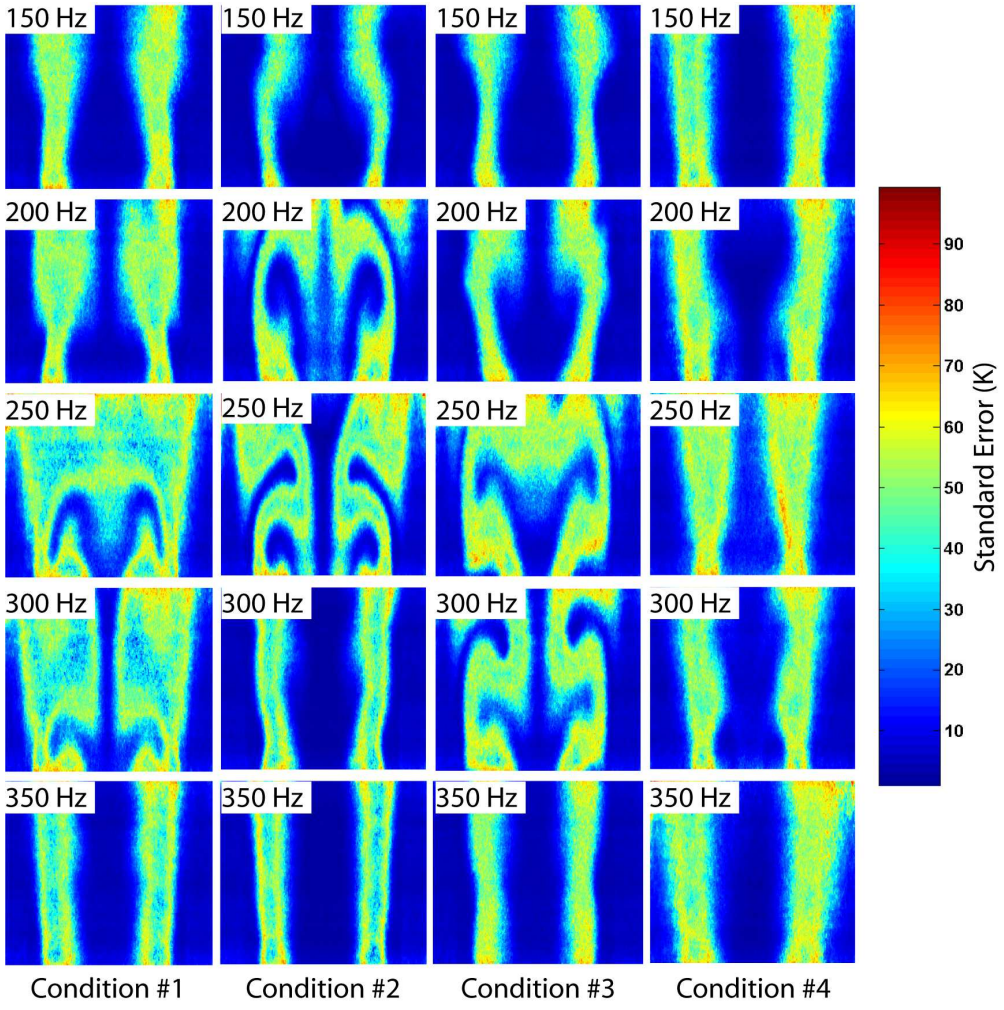

Figure 4-36 Sample of standard error images

Most of the standard error is in the 50-60 K range. The error is larger at the top and bottom edges of the images, which is expected since laser intensity is lower and these

regions are subsequently more sensitive to noise. The standard error for flow condition #4 is washed out compared to the other condition since the flame was in the unsteady mode or simply responding to cross breezes in the room.

CHAPTER 5 Conclusion

This project focused on a new application of planar Rayleigh scattering for quantitative temperature measurement in an externally-forced diffusion flame. Using this diagnostic technique, fluid / vortex interactions with a flame were observed and the affects of large versus small scale mixing were inferred. Planar laser Rayleigh scattering was used to study in high spatial detail a cross-sectional slice of the temperature distribution of an acoustically forced coaxial diffusion flame at four different flow conditions. The temporal evolution of the transient temperature field due to the forcing was detailed in this study and the temperature increase associated with forced flames was verified. This study provides a unique experimental database that could be useful for computational fluid dynamic validation.

Rayleigh scattering was selected as the diagnostic due to the ease of implementation, high signal to noise ratio, and ease of data reduction. Rayleigh scattering is useful for quantitatively characterizing a flow. Schlieren and chemiluminescence are commonly used as diagnostics for combusting flow, however both are volume integrated effects.

Unfortunately, due to the lack of spectral difference between the signal and the incident light, Rayleigh techniques are extremely prone to interference. Due to its non-species specific nature, only binary gas mixtures can be studies. For reacting flow, special considerations about the fuel need to be made. As a result, Rayleigh scattering methods are limited to only simple systems.

Using this diagnostic technique, several conclusions can be made on the effects of forcing on a reacting flow. The limiting factor in a diffusion flame is the diffusion rate

between the fuel and the air, so the main goal of combustion enhancement is to overcome this limitation. Forcing the flow was observed to enhance combustion on both small and large scale. Small scale mixing increases with forcing until near adiabatic flame temperature is reached. This was concluded from flow conditions #1 and #2, as the flame temperatures were significantly higher than the unforced cases at high frequencies, even after the production of large-scale vortices ceased. Increasing the absolute velocity of the flow delays the onset of small scale mixing enhancements. Small scale enhancement occurs when the wavelength of the small amplitude disturbances decreases to an effective value. Introducing a shearing component to the flow seemed to negate contributions from small scale mixing, surmised from the lack of increase in temperature at the high frequencies for flow conditions #3 and #4.

At the preferred mode of the burner, large-scale vortices roll up, entraining large amounts of cooler reactants. The formation of the large-scale vortices increases the residence time of fuel and air, allowing more time for diffusion to occur. The bulk mixing of the reactants brings fresh fuel and air to the reaction region as well. Vortices of significant strength, though, cause reaction regions to thin and cool from the strain, observed for the first three flow conditions. The entrained reactants cool the flame as well. Due to the competition between these factors, large-scale vortices increase volumetric energy release primarily by changing the shape of the flame so it occupies less space above the burner. Forcing the flow, on the other hand, brings the system closer to a turbulent mode as pockets of reactants are quickly consumed by adjacent flame fronts

The measurement technique implemented in this study was able to effectively image regularly occurring flow structures. However, the ability of the system to ascertain

the temperature, especially at high temperatures, needs to be improved. A higher signal to noise ratio could help improve the rates of data rejection, which are at times were quite high in this study. Clever noise reduction, laser pulse stretching, and a higher laser frequency due to the wavelength to the minus fourth dependency of the cross section, as well as better collecting optics to fully use the ICCD are possible improvements.

There are a number of possibilities for further extension of this study. Using this diagnostic method in conjunction with Schlieren, chemiluminescence, or another laser diagnostic technique would further elucidate fluid interaction with flames. Combined diagnostic methods could increase the variety of fuels and setups that could be studied. Further study of flame stretch versus the concentration gradient of the reactants as a consequence of flame vortex interaction should be carried out. Also, there is a great deal of interest in instantaneous measurements to understand the unsteady component to forced reacting flows. Most combustion studies are also performed on enclosed systems, as they are more common. Applying Rayleigh scattering to an enclosed forced system is potential future work.

Appendix A- Flame and Rayleigh Scattering Images

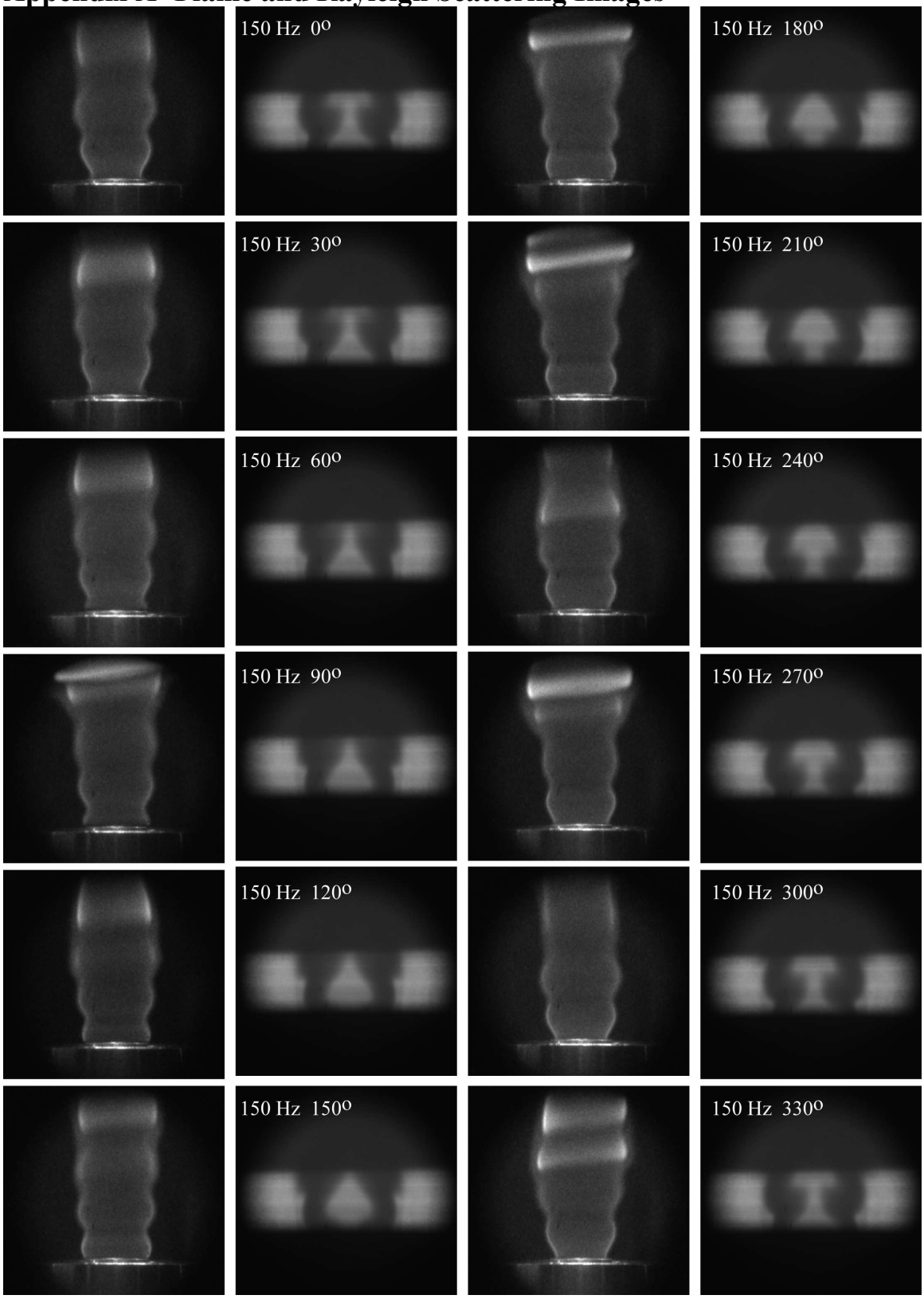

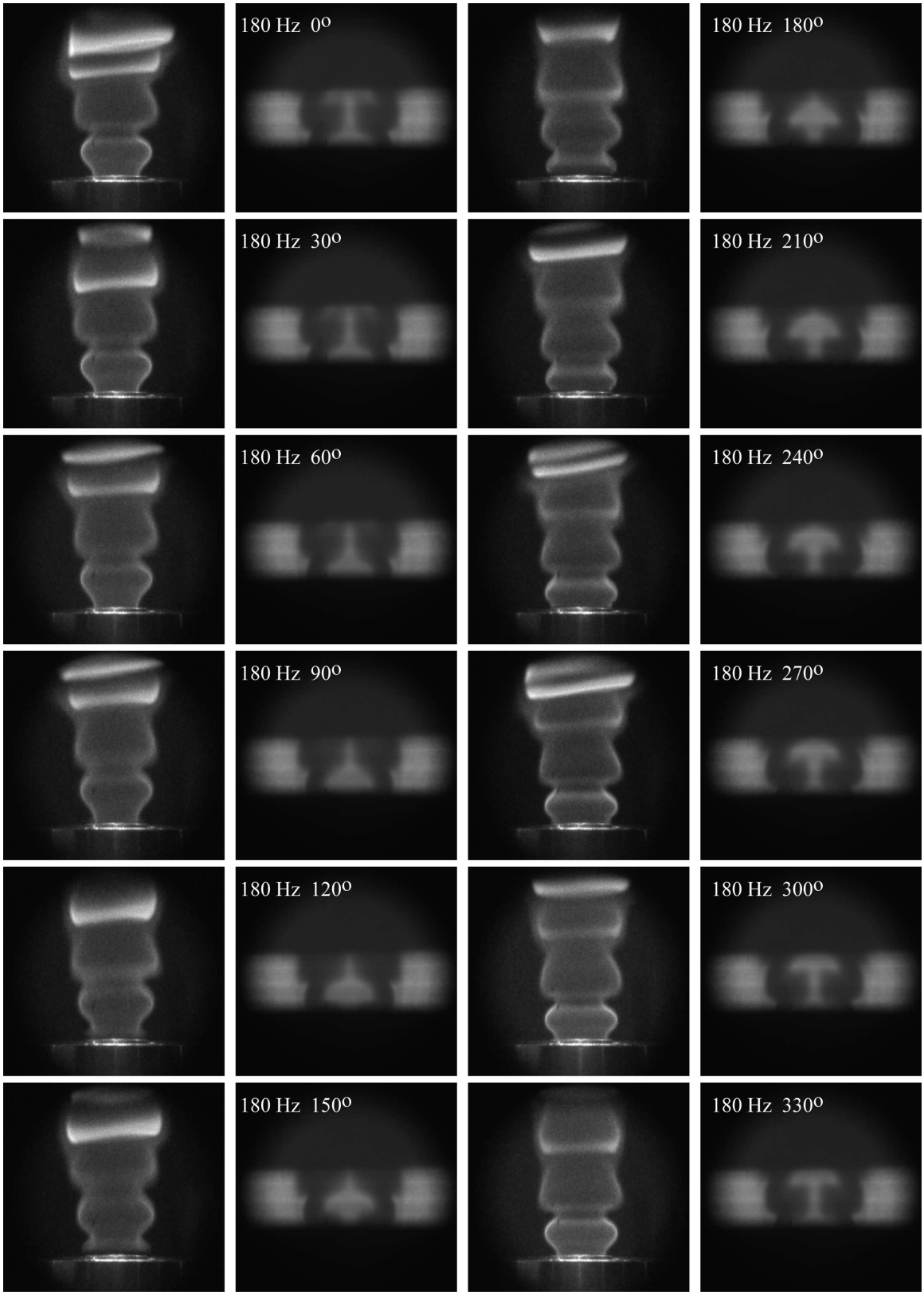
180 Hz 0°
180 Hz 180°
180 Hz 30°
180 Hz 210°
180 Hz 60°
180 Hz 240°
180 Hz 90°
180 Hz 270°
180 Hz 120°
180 Hz 300°
180 Hz 150°
180 Hz 330°

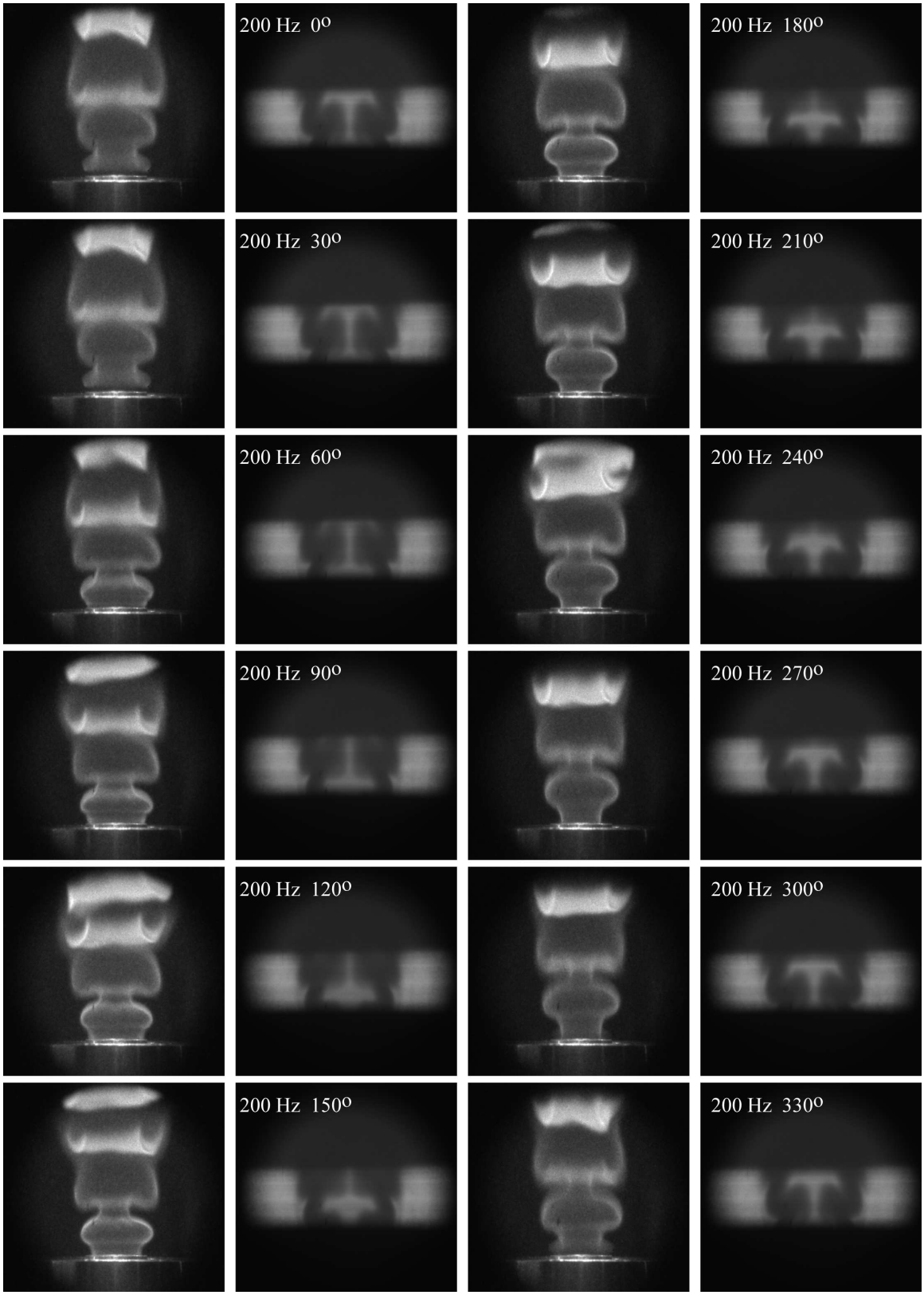
200 Hz 0°
200 Hz 180°
200 Hz 30°
200 Hz 210°
200 Hz 60°
200 Hz 240°
200 Hz 90°
200 Hz 270°
200 Hz 120°
200 Hz 300°
200 Hz 150°
200 Hz 330°

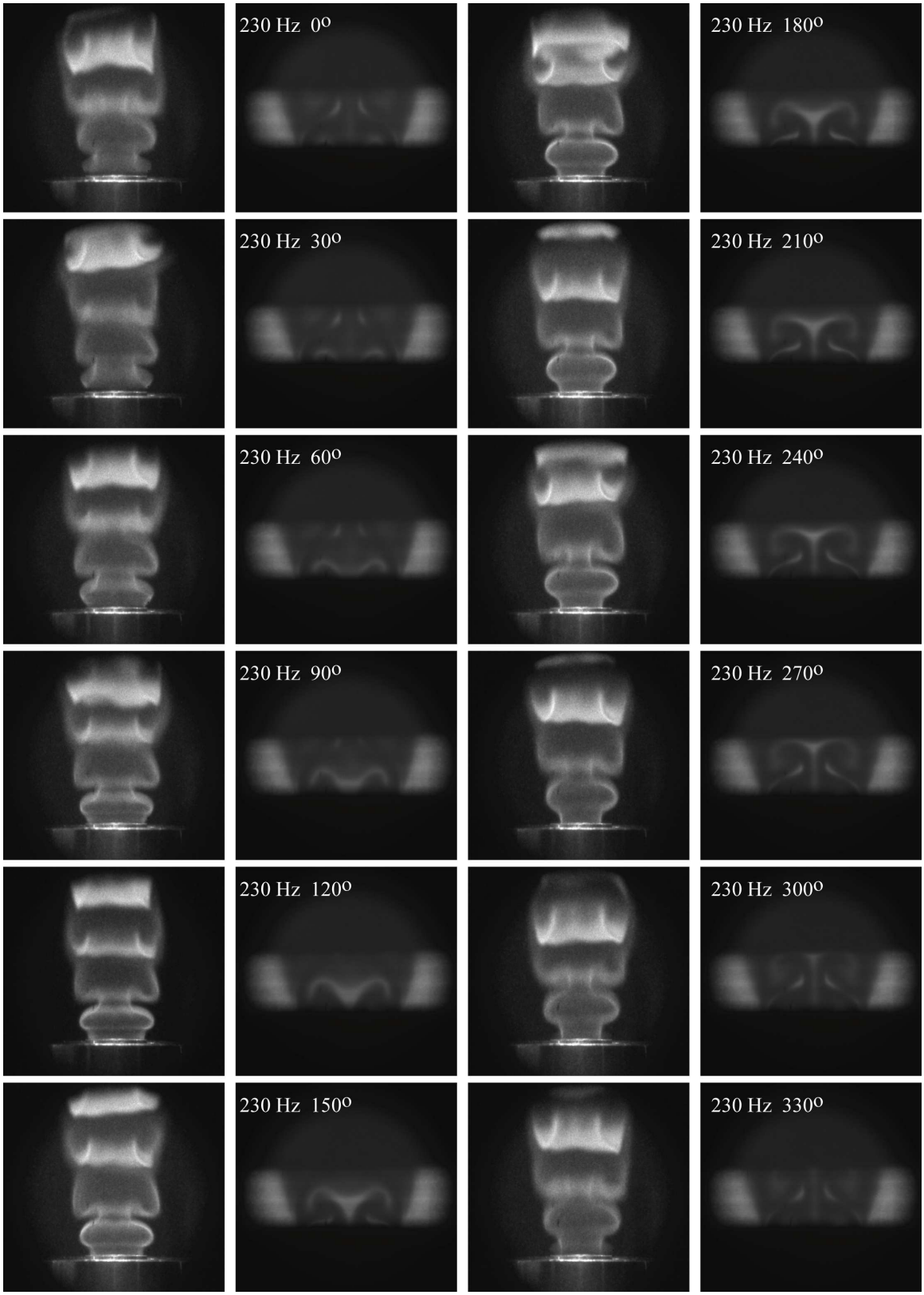
230 Hz 0°
230 Hz 180°
230 Hz 30°
230 Hz 210°
230 Hz 60°
230 Hz 240°
230 Hz 90°
230 Hz 270°
230 Hz 120°
230 Hz 300°
230 Hz 150°
230 Hz 330°

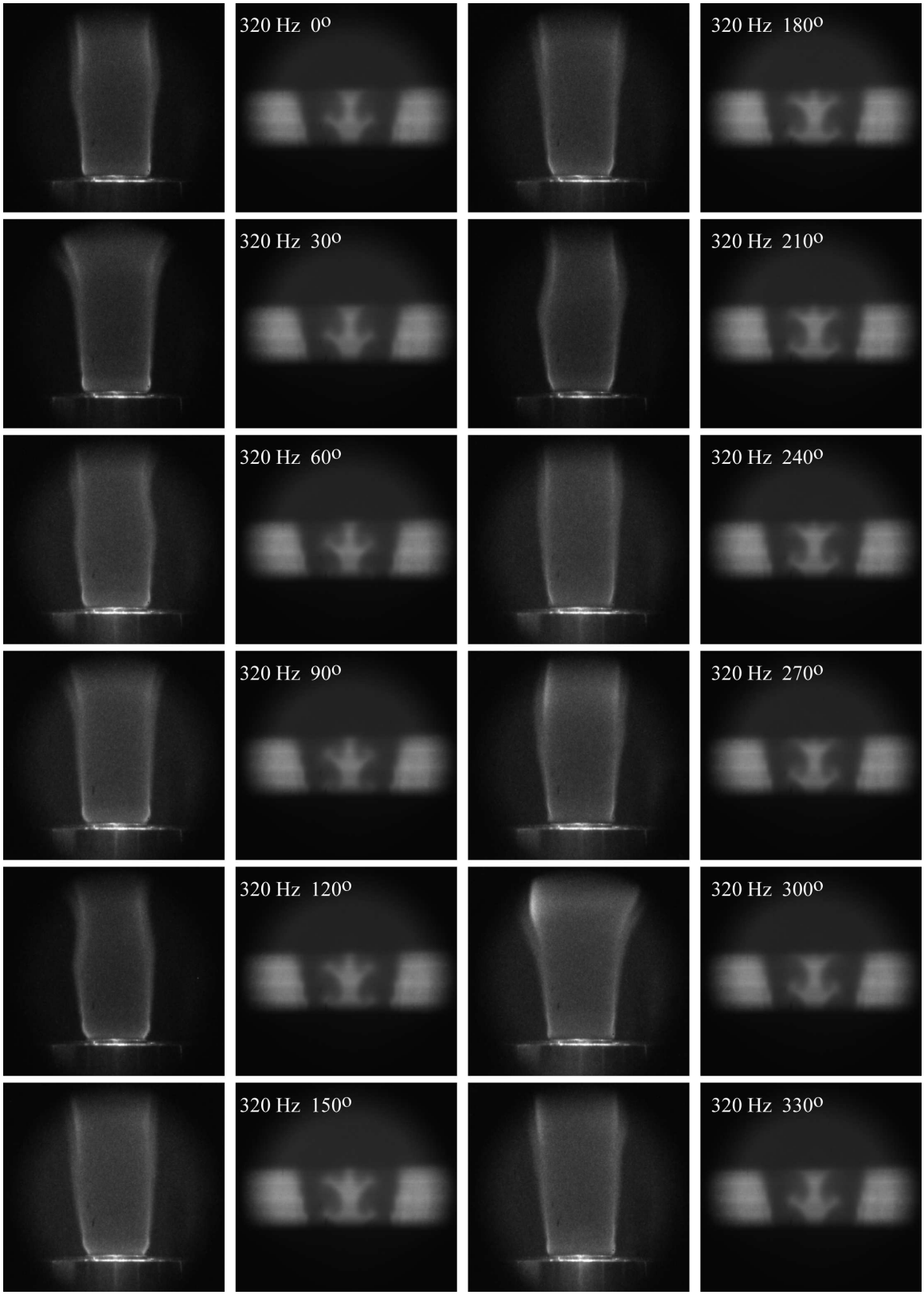
320 Hz 0°
320 Hz 180°
320 Hz 30°
320 Hz 210°
320 Hz 60°
320 Hz 240°
320 Hz 90°
320 Hz 270°
320 Hz 120°
320 Hz 300°
320 Hz 150°
320 Hz 330°

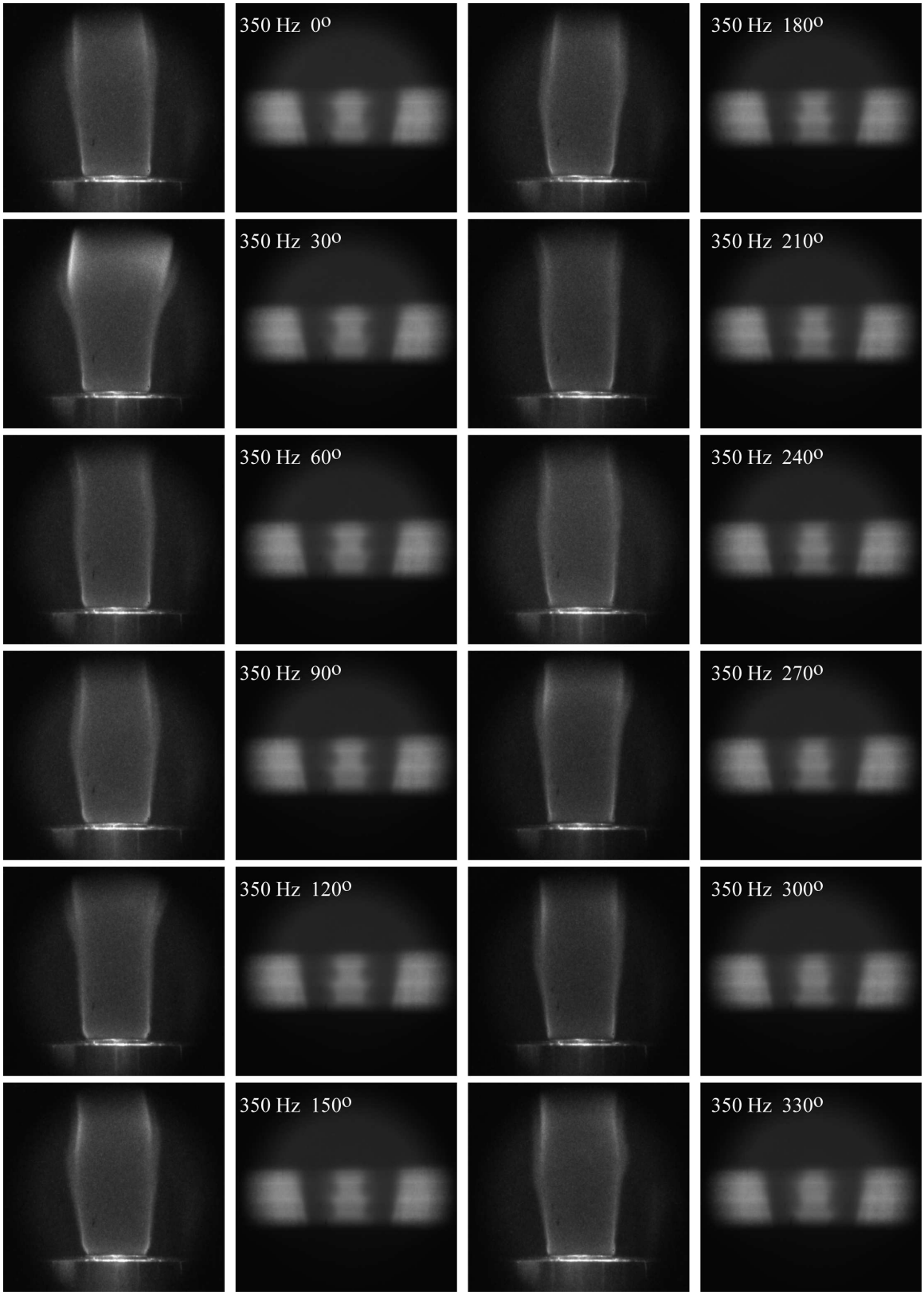
350 Hz 0°
350 Hz 180°
350 Hz 30°
350 Hz 210°
350 Hz 60°
350 Hz 240°
350 Hz 90°
350 Hz 270°
350 Hz 120°
350 Hz 300°
350 Hz 150°
350 Hz 330°

Appendix B- Temperature Maps

Appendix B.1 Flow Condition 1: Vr=1, U_{inner}=1.36 m/s

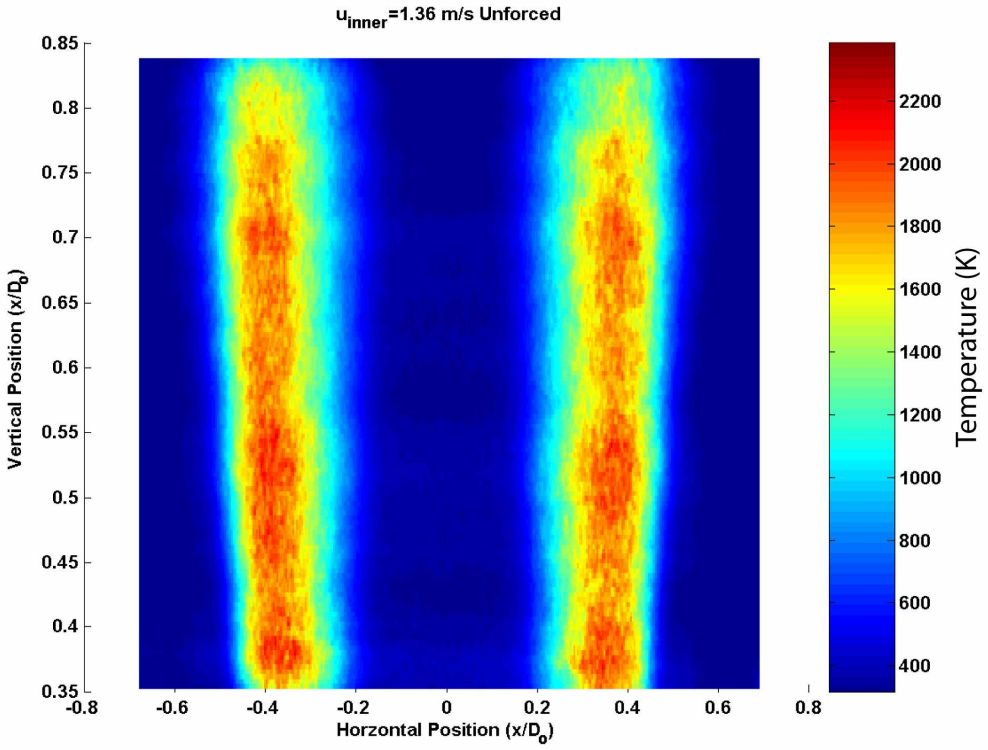

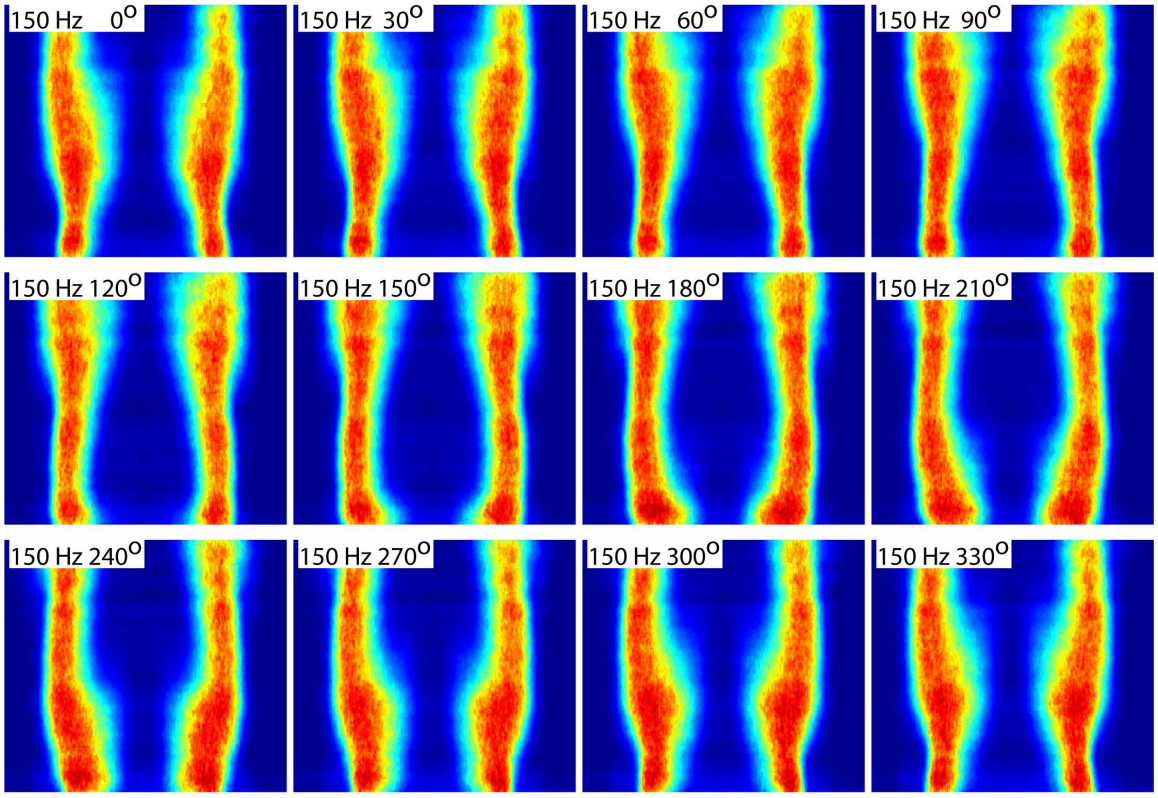

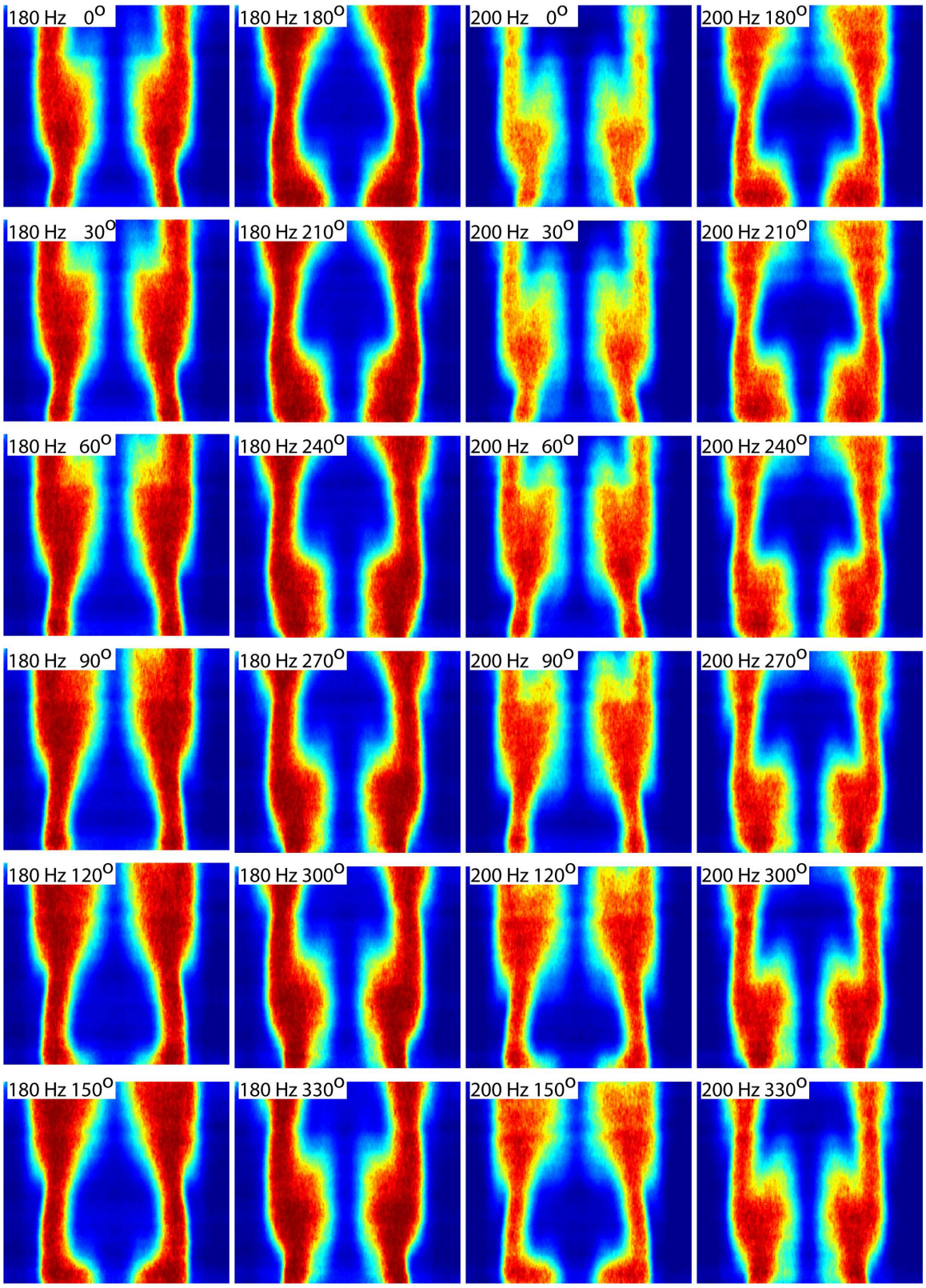
180 Hz 0°
180 Hz 180°
200 Hz 0°
200 Hz 180°
180 Hz 30°
180 Hz 210°
200 Hz 30°
200 Hz 210°
180 Hz 60°
180 Hz 240°
200 Hz 60°
200 Hz 240°
180 Hz 90°
180 Hz 270°
200 Hz 90°
200 Hz 270°
180 Hz 120°
180 Hz 300°
200 Hz 120°
200 Hz 300°
180 Hz 150°
180 Hz 330°
200 Hz 150°
200 Hz 330°

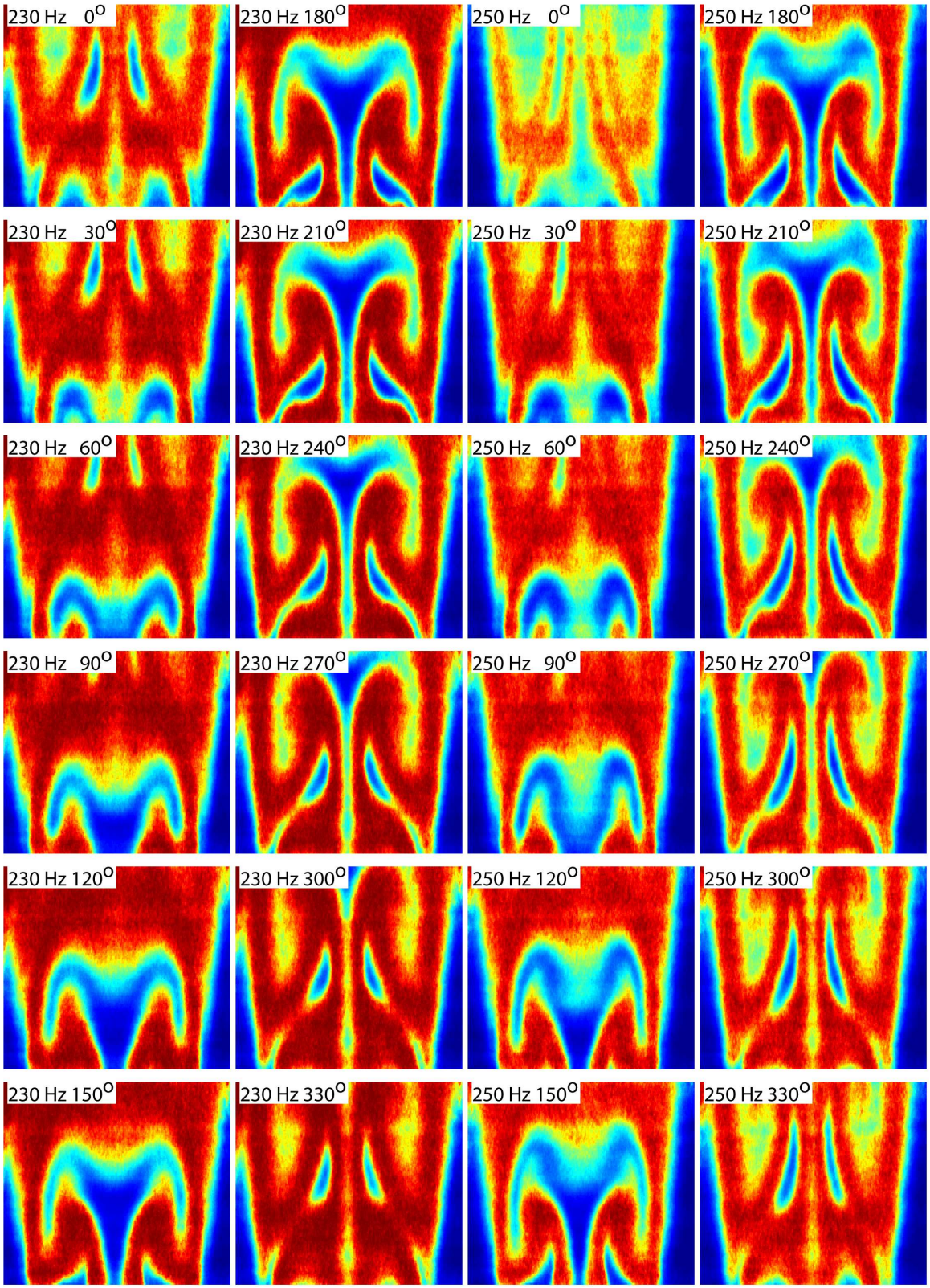
230 Hz 0°
230 Hz 180°
250 Hz 0°
250 Hz 180°
230 Hz 30°
230 Hz 210°
250 Hz 30°
250 Hz 210°
230 Hz 60°
230 Hz 240°
250 Hz 60°
250 Hz 240°
230 Hz 90°
230 Hz 270°
250 Hz 90°
250 Hz 270°
230 Hz 120°
230 Hz 300°
250 Hz 120°
250 Hz 300°
230 Hz 150°
230 Hz 330°
250 Hz 150°
250 Hz 330°

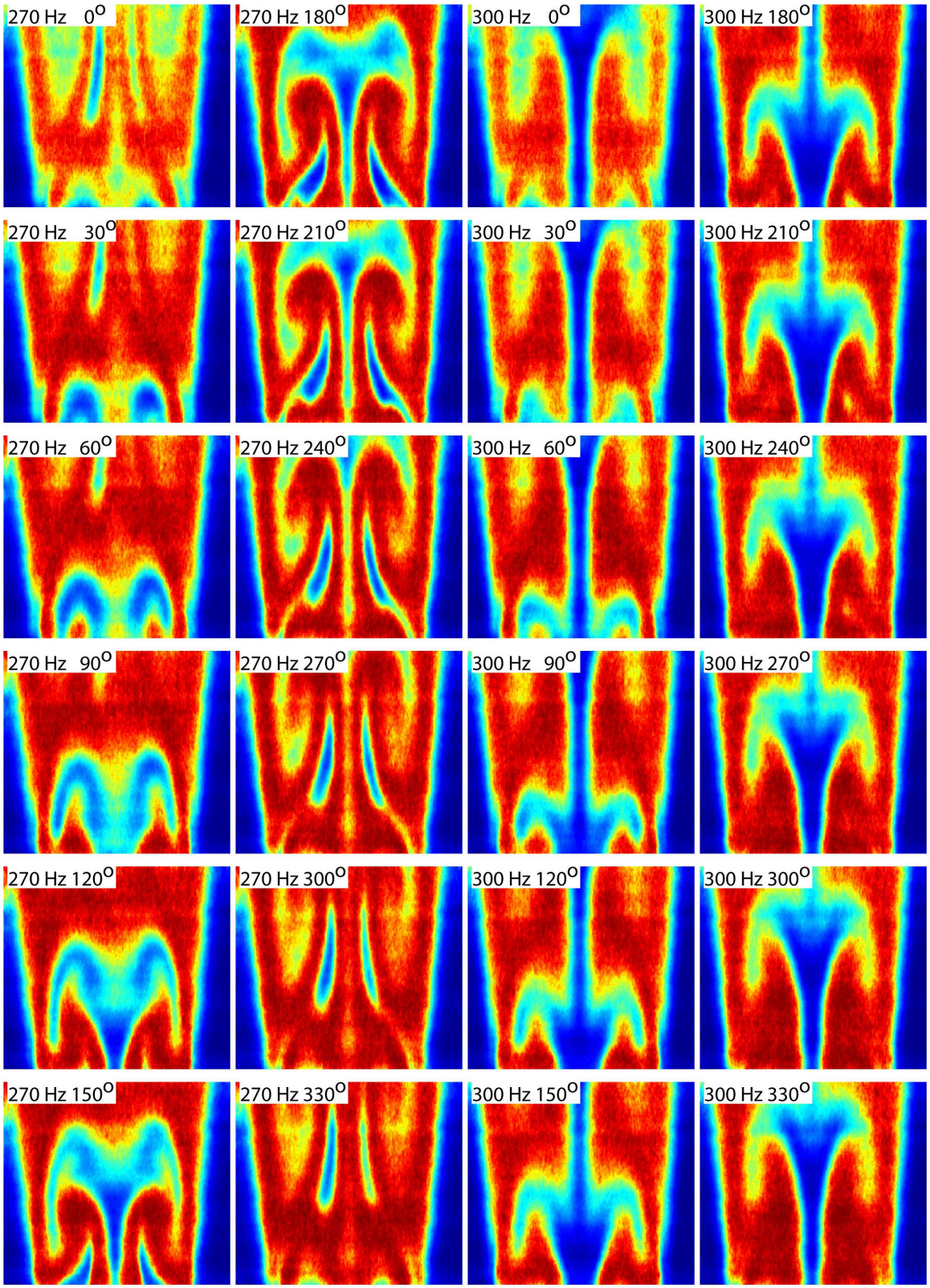
270 Hz 0°
270 Hz 180°
300 Hz 0°
300 Hz 180°
270 Hz 30°
270 Hz 210°
300 Hz 30°
300 Hz 210°
270 Hz 60°
270 Hz 240°
300 Hz 60°
300 Hz 240°
270 Hz 90°
270 Hz 270°
300 Hz 90°
300 Hz 270°
270 Hz 120°
270 Hz 300°
300 Hz 120°
300 Hz 300°
270 Hz 150°
270 Hz 330°
300 Hz 150°
300 Hz 330°

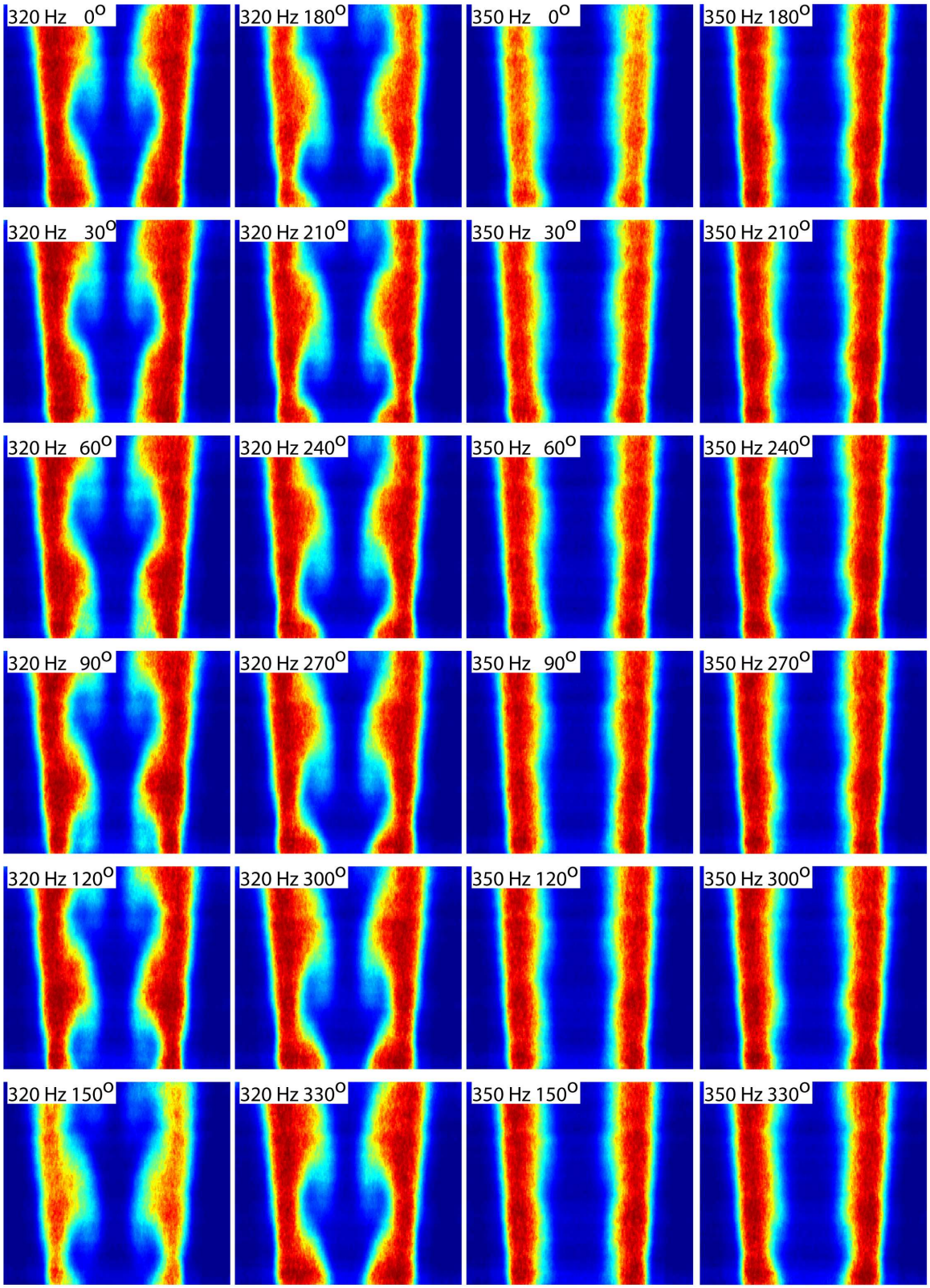
320 Hz 0°
320 Hz 180°
350 Hz 0°
350 Hz 180°
320 Hz 30°
320 Hz 210°
350 Hz 30°
350 Hz 210°
320 Hz 60°
320 Hz 240°
350 Hz 60°
350 Hz 240°
320 Hz 90°
320 Hz 270°
350 Hz 90°
350 Hz 270°
320 Hz 120°
320 Hz 300°
350 Hz 120°
350 Hz 300°
320 Hz 150°
320 Hz 330°
350 Hz 150°
350 Hz 330°

Appendix B.2 Flow Condition 2: Vr=1, Uinner=2.16 m/s

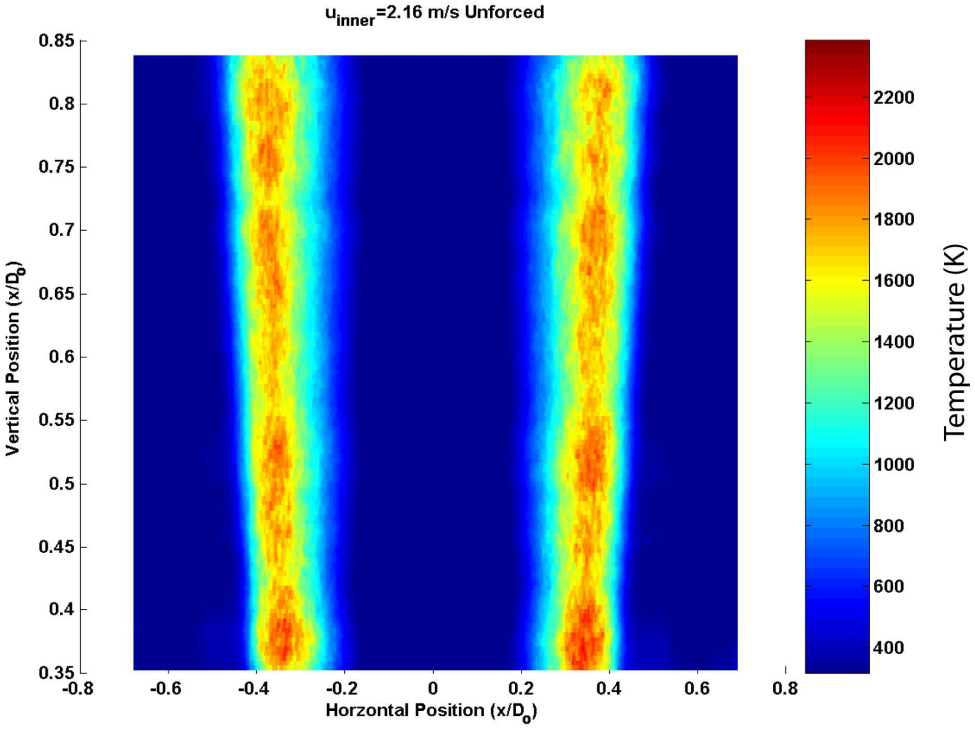

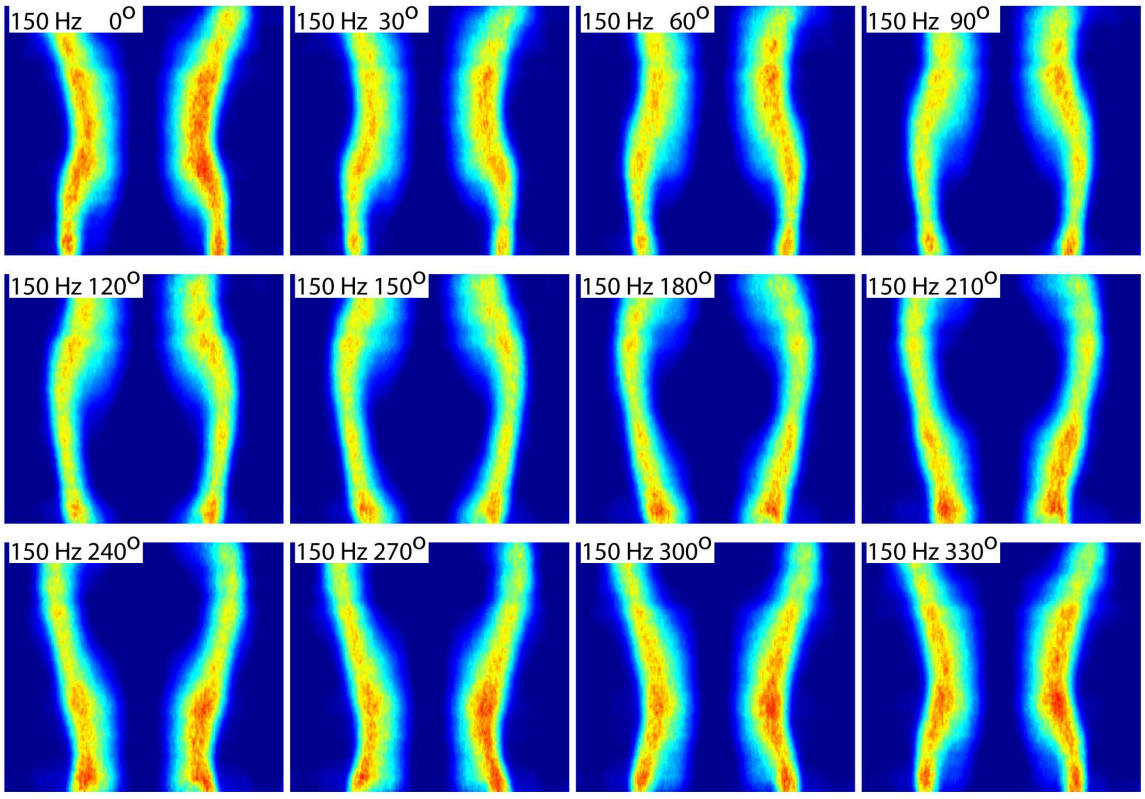

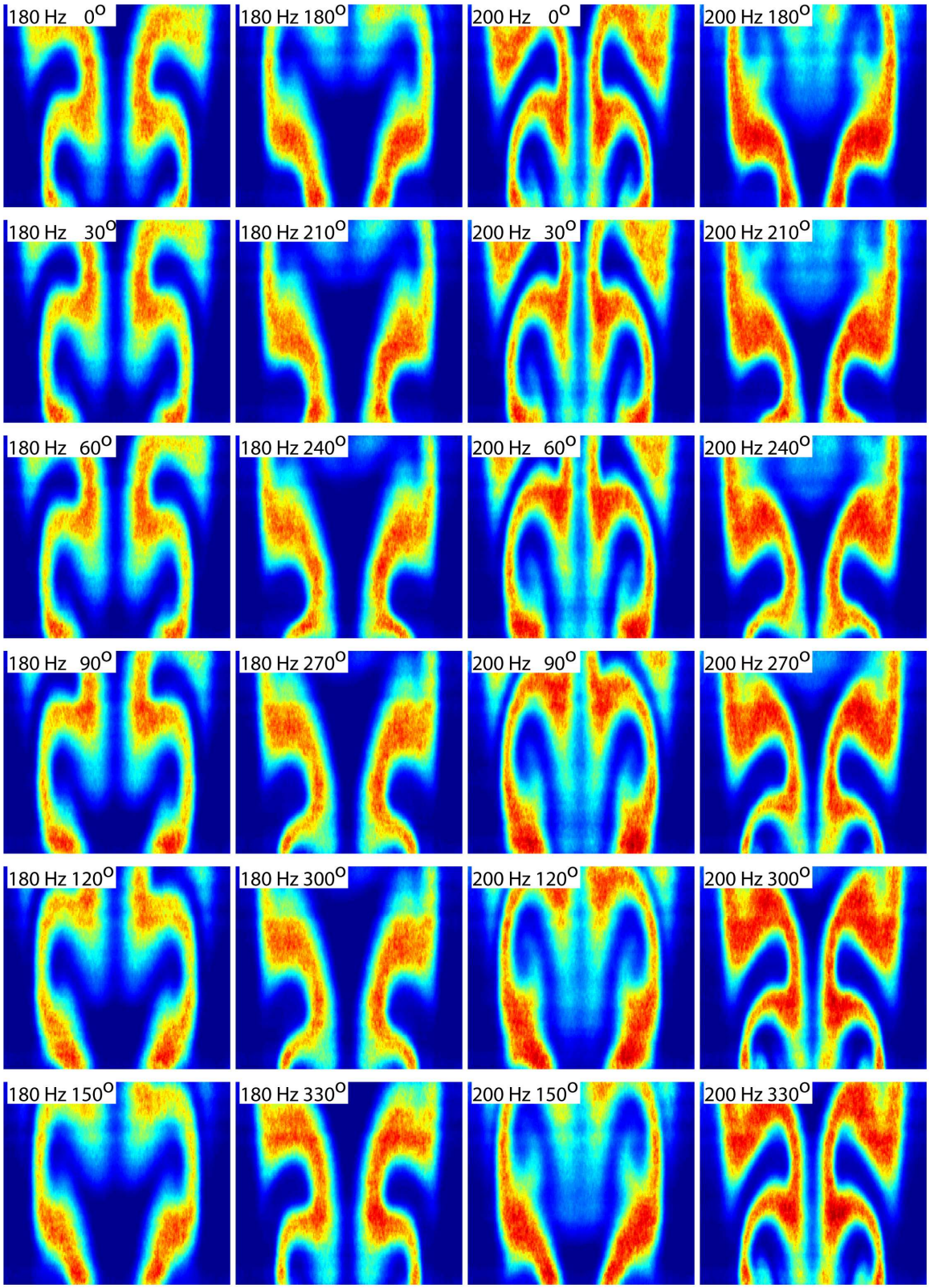
180 Hz 0°
180 Hz 180°
200 Hz 0°
200 Hz 180°
180 Hz 30°
180 Hz 210°
200 Hz 30°
200 Hz 210°
180 Hz 60°
180 Hz 240°
200 Hz 60°
200 Hz 240°
180 Hz 90°
180 Hz 270°
200 Hz 90°
200 Hz 270°
180 Hz 120°
180 Hz 300°
200 Hz 120°
200 Hz 300°
180 Hz 150°
180 Hz 330°
200 Hz 150°
200 Hz 330°

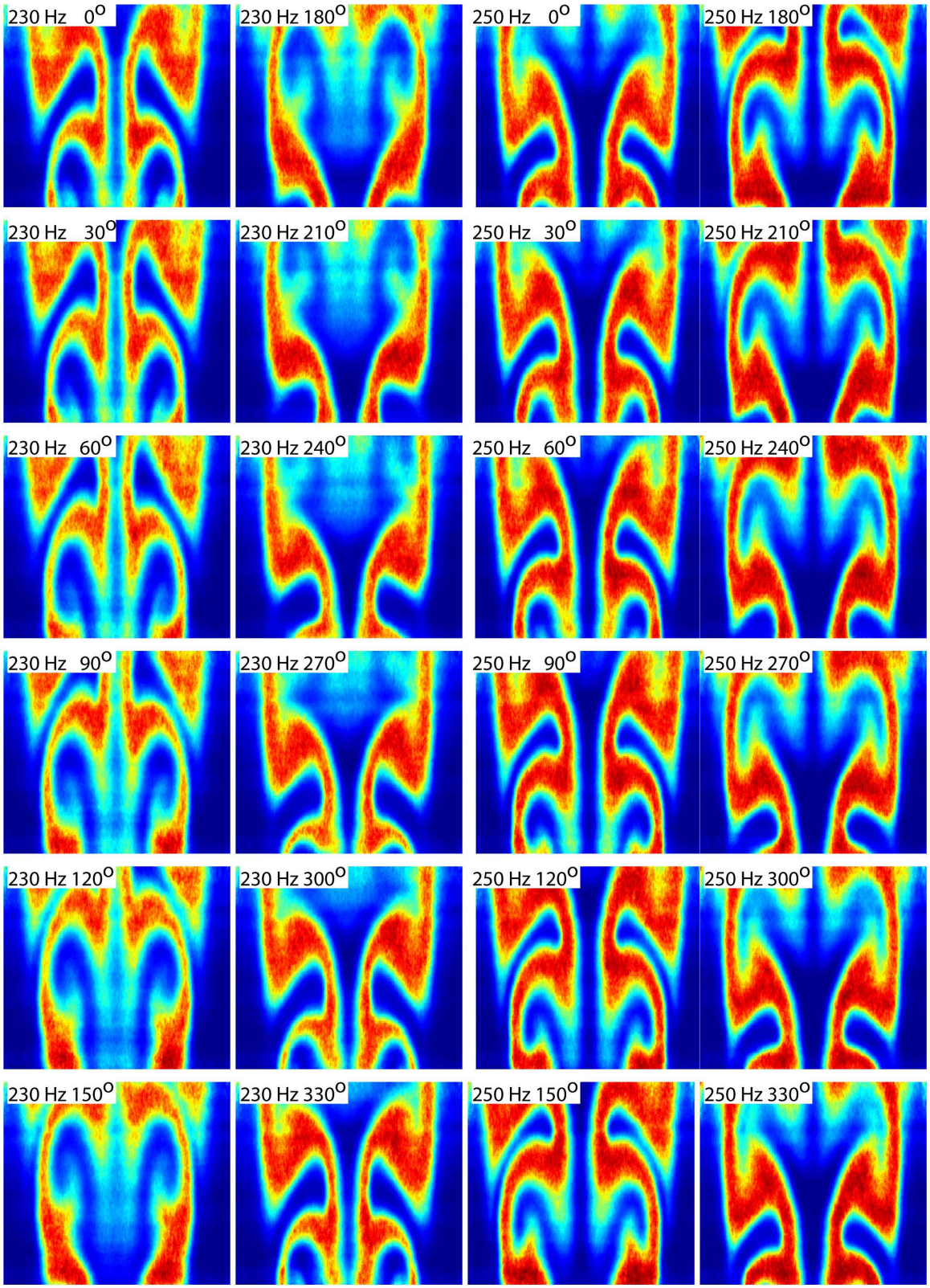
230 Hz 0°
230 Hz 180°
250 Hz 0°
250 Hz 180°
230 Hz 30°
230 Hz 210°
250 Hz 30°
250 Hz 210°
230 Hz 60°
230 Hz 240°
250 Hz 60°
250 Hz 240°
230 Hz 90°
230 Hz 270°
250 Hz 90°
250 Hz 270°
230 Hz 120°
230 Hz 300°
250 Hz 120°
250 Hz 300°
230 Hz 150°
230 Hz 330°
250 Hz 150°
250 Hz 330°

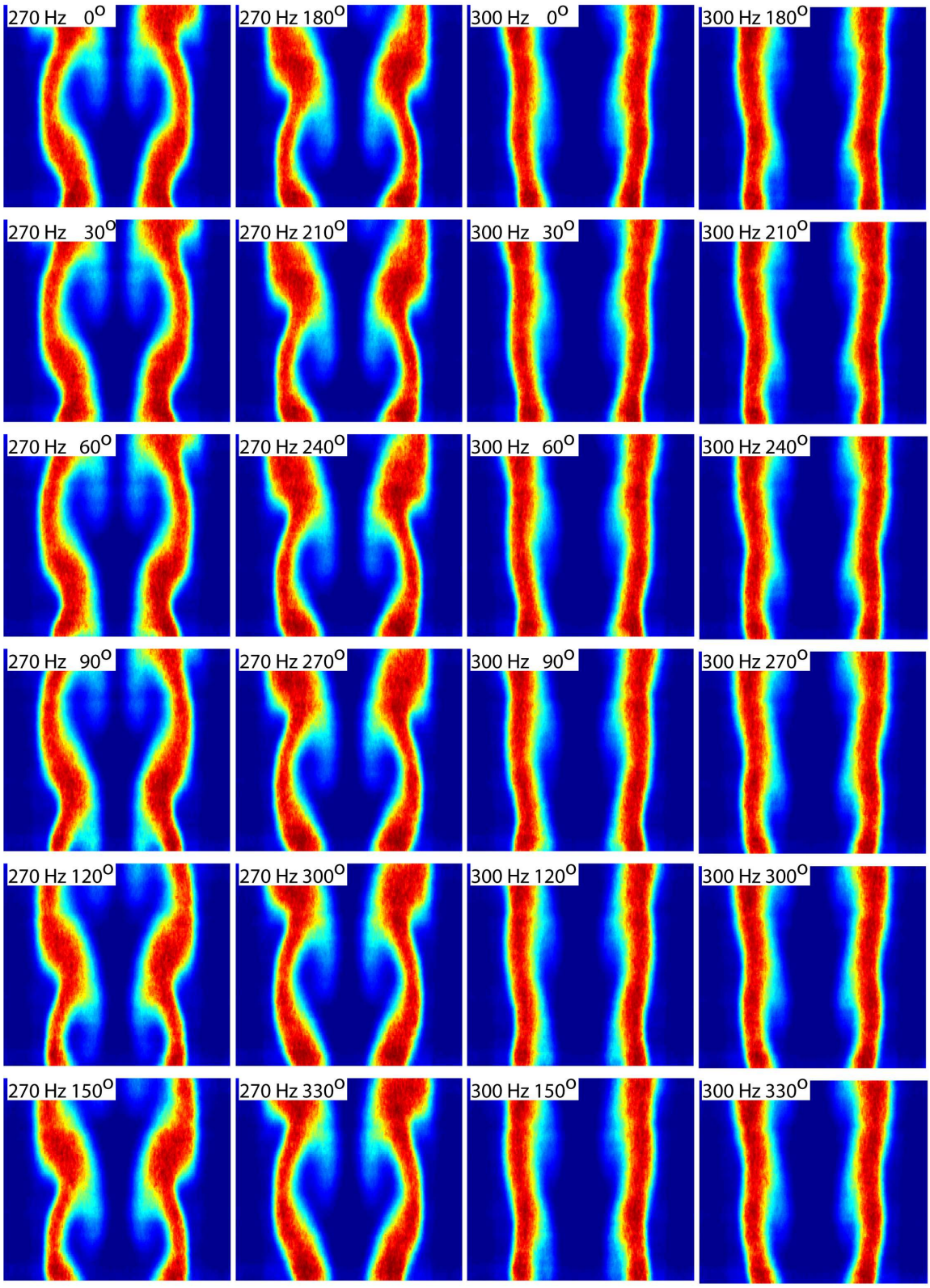
270 Hz 0°
270 Hz 180°
300 Hz 0°
300 Hz 180°
270 Hz 30°
270 Hz 210°
300 Hz 30°
300 Hz 210°
270 Hz 60°
270 Hz 240°
300 Hz 60°
300 Hz 240°
270 Hz 90°
270 Hz 270°
300 Hz 90°
300 Hz 270°
270 Hz 120°
270 Hz 300°
300 Hz 120°
300 Hz 300°
270 Hz 150°
270 Hz 330°
300 Hz 150°
300 Hz 330°

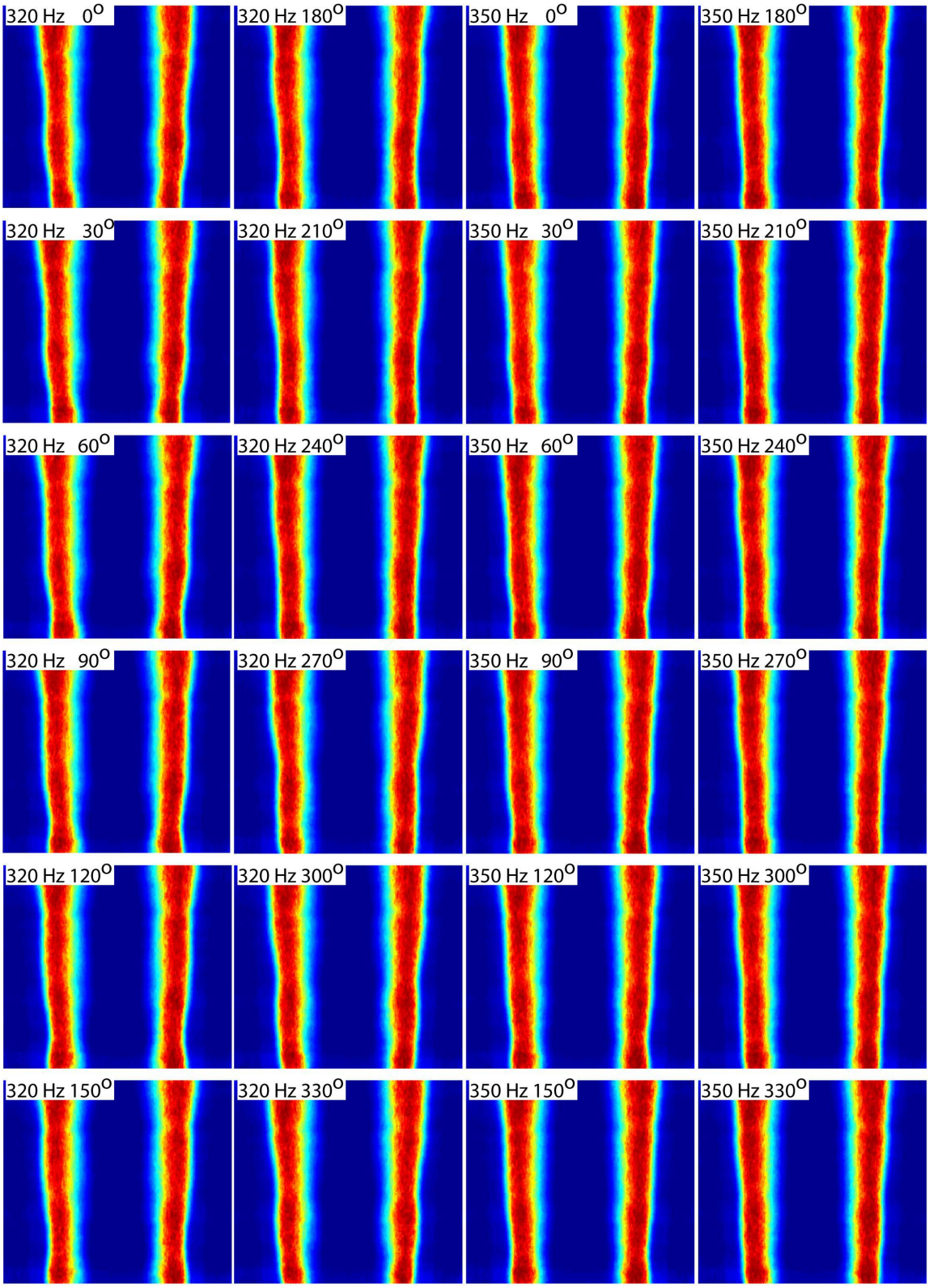
320 Hz 0°
320 Hz 180°
350 Hz 0°
350 Hz 180°
320 Hz 30°
320 Hz 210°
350 Hz 30°
350 Hz 210°
320 Hz 60°
320 Hz 240°
350 Hz 60°
350 Hz 240°
320 Hz 90°
320 Hz 270°
350 Hz 90°
350 Hz 270°
320 Hz 120°
320 Hz 300°
350 Hz 120°
350 Hz 300°
320 Hz 150°
320 Hz 330°
350 Hz 150°
350 Hz 330°

Appendix B.3 Flow Condition 3: Vr=2, Uinner=1.36 m/s

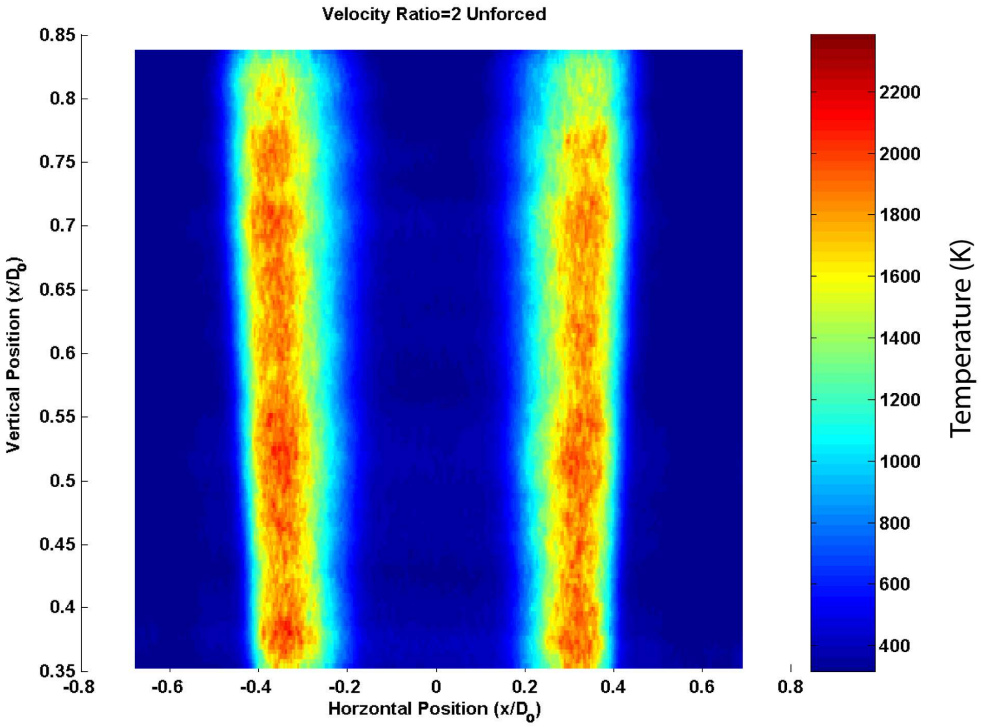

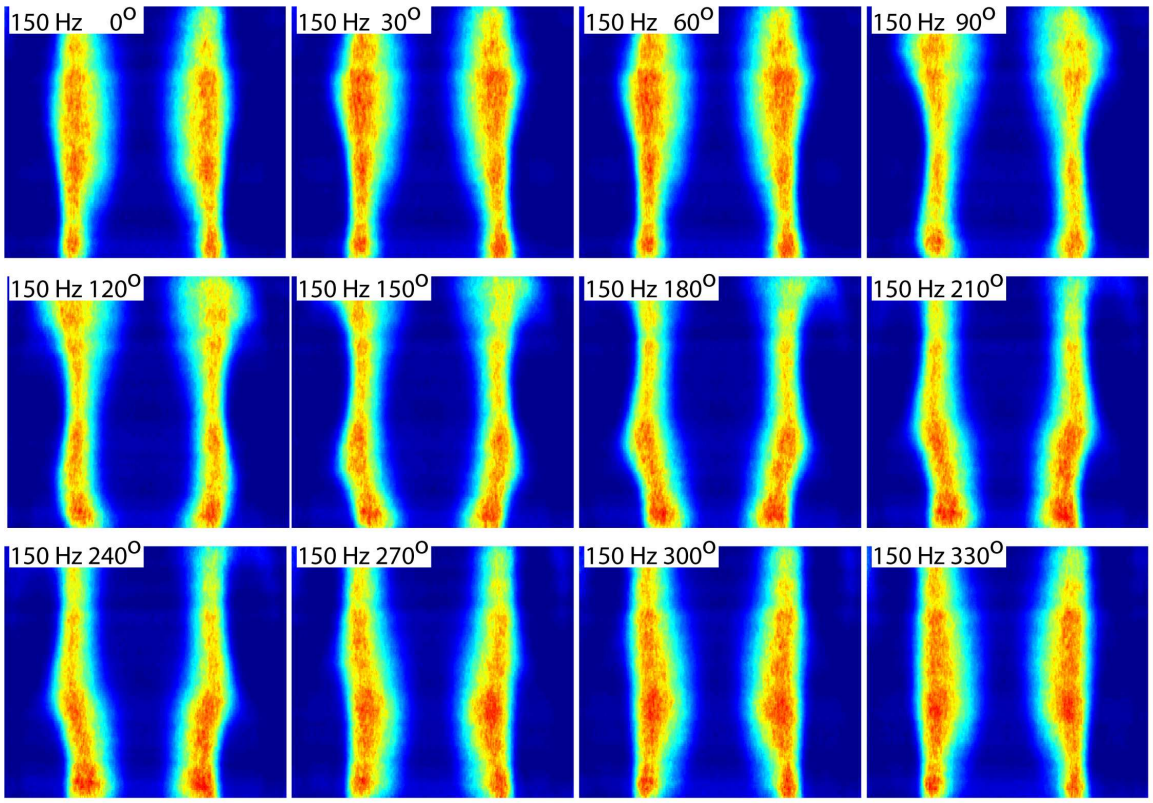

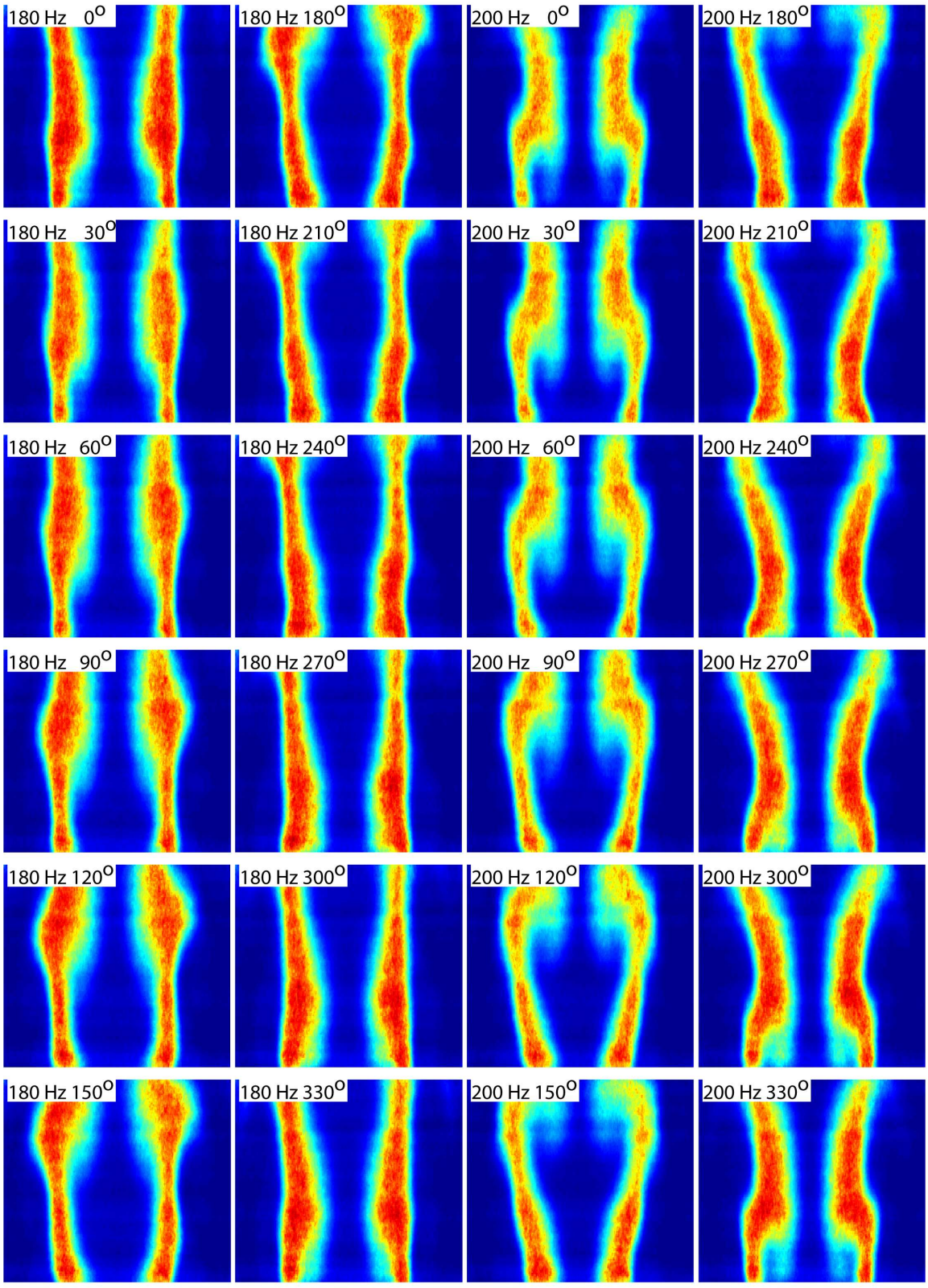
180 Hz 0°
180 Hz 180°
200 Hz 0°
200 Hz 180°
180 Hz 30°
180 Hz 210°
200 Hz 30°
200 Hz 210°
180 Hz 60°
180 Hz 240°
200 Hz 60°
200 Hz 240°
180 Hz 90°
180 Hz 270°
200 Hz 90°
200 Hz 270°
180 Hz 120°
180 Hz 300°
200 Hz 120°
200 Hz 300°
180 Hz 150°
180 Hz 330°
200 Hz 150°
200 Hz 330°

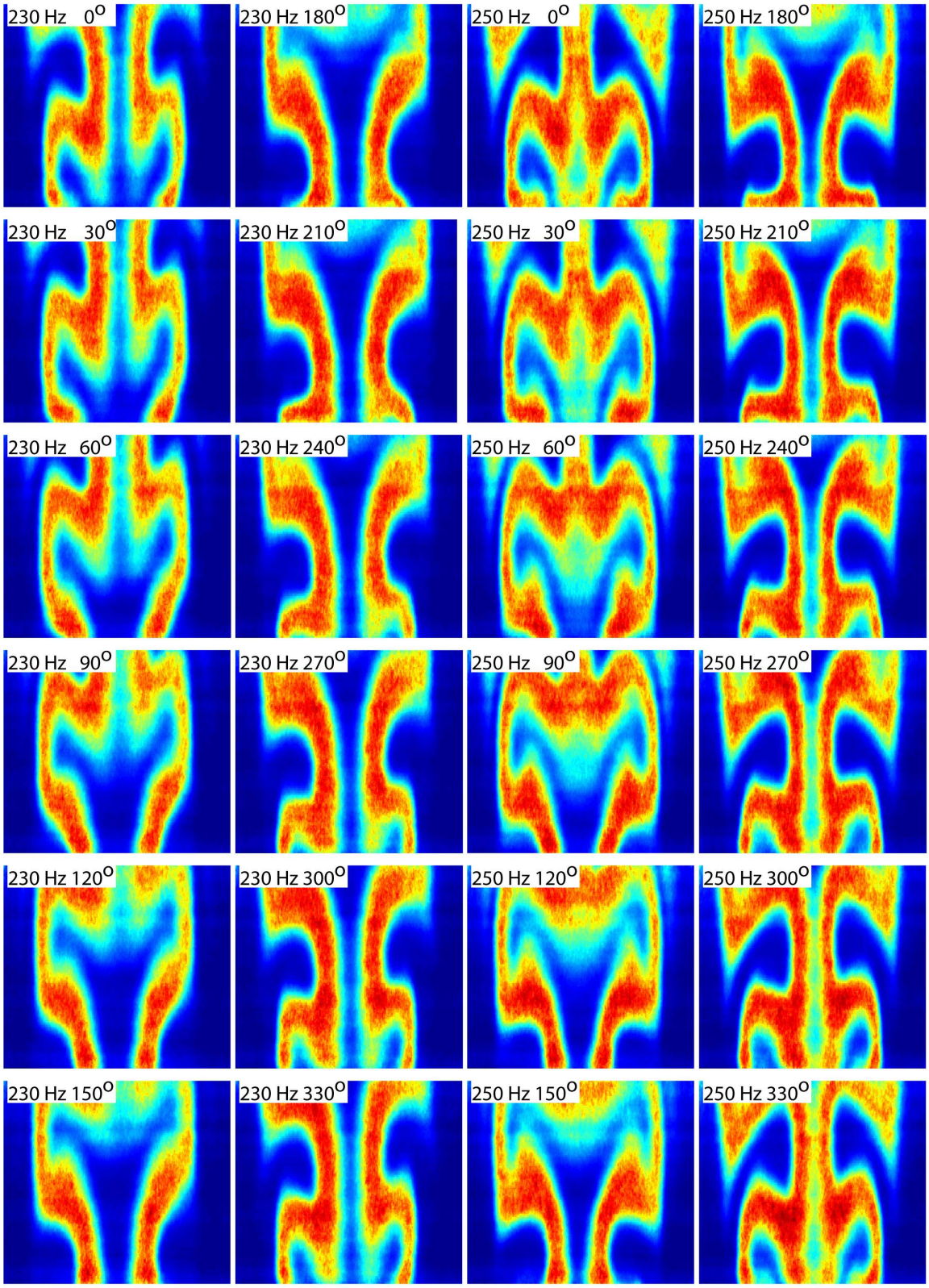
230 Hz 0°
230 Hz 180°
250 Hz 0°
250 Hz 180°
230 Hz 30°
230 Hz 210°
250 Hz 30°
250 Hz 210°
230 Hz 60°
230 Hz 240°
250 Hz 60°
250 Hz 240°
230 Hz 90°
230 Hz 270°
250 Hz 90°
250 Hz 270°
230 Hz 120°
230 Hz 300°
250 Hz 120°
250 Hz 300°
230 Hz 150°
230 Hz 330°
250 Hz 150°
250 Hz 330°

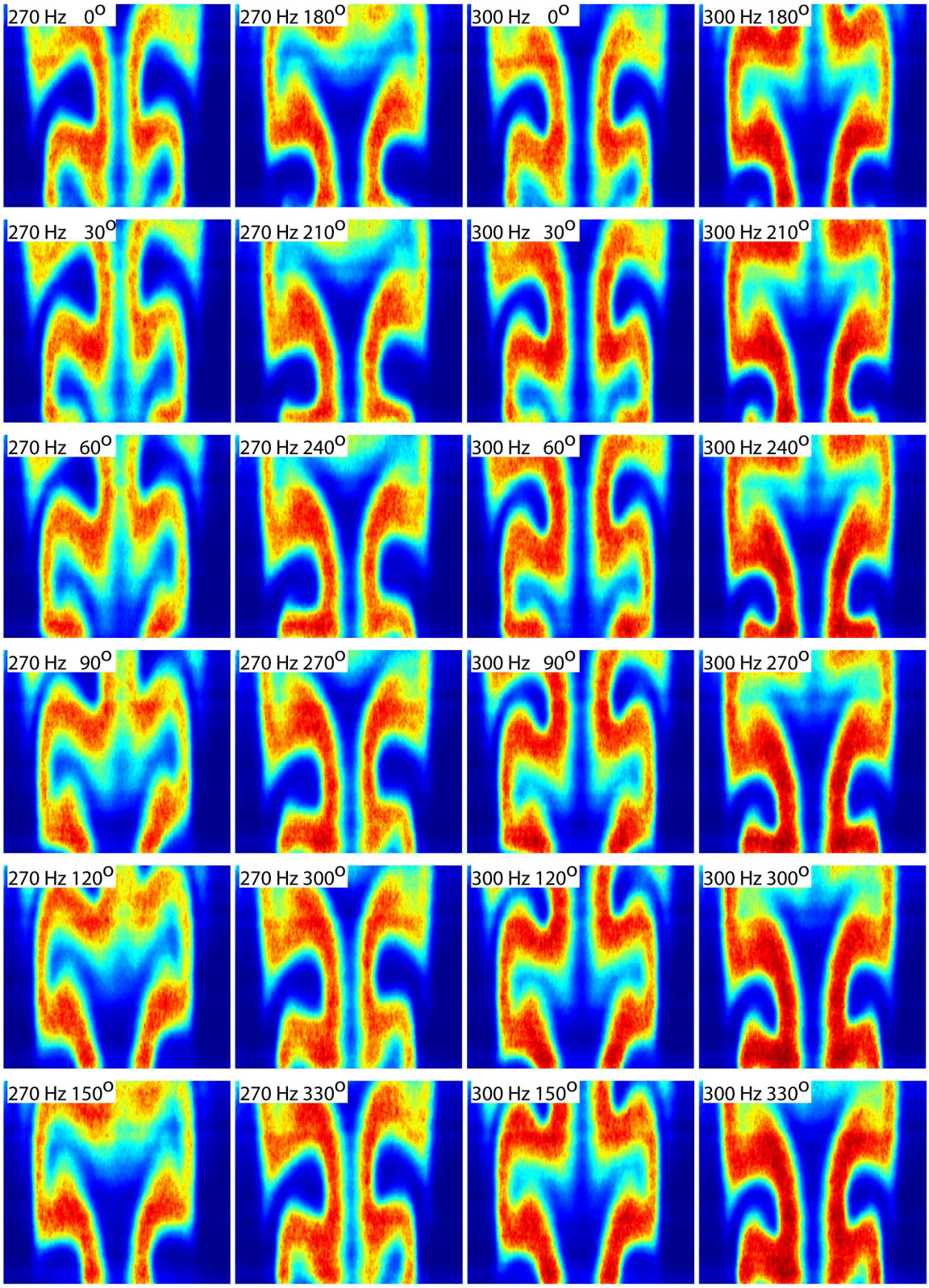
270 Hz 0°
270 Hz 180°
300 Hz 0°
300 Hz 180°
270 Hz 30°
270 Hz 210°
300 Hz 30°
300 Hz 210°
270 Hz 60°
270 Hz 240°
300 Hz 60°
300 Hz 240°
270 Hz 90°
270 Hz 270°
300 Hz 90°
300 Hz 270°
270 Hz 120°
270 Hz 300°
300 Hz 120°
300 Hz 300°
270 Hz 150°
270 Hz 330°
300 Hz 150°
300 Hz 330°

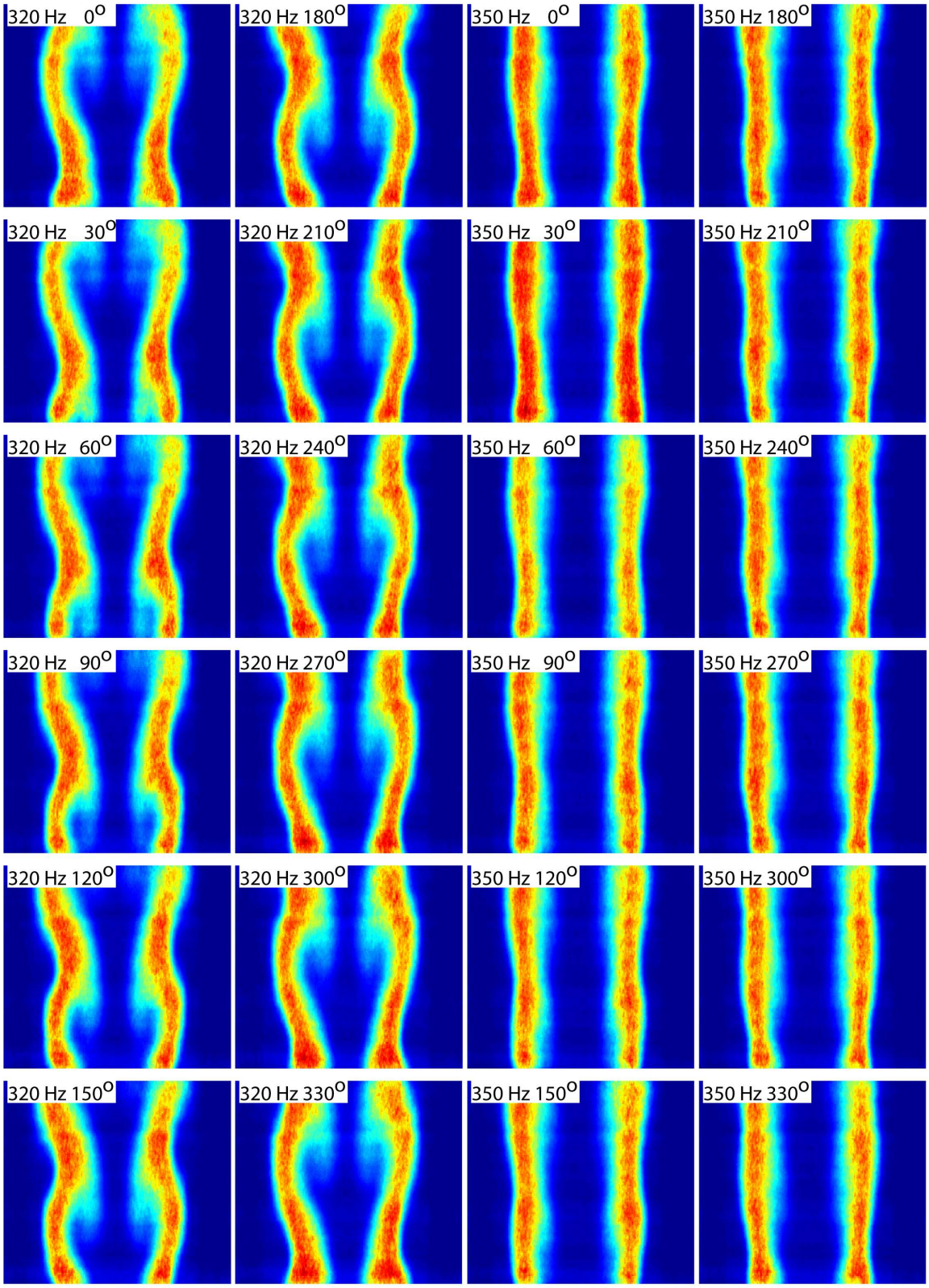
320 Hz 0°
320 Hz 180°
350 Hz 0°
350 Hz 180°
320 Hz 30°
320 Hz 210°
350 Hz 30°
350 Hz 210°
320 Hz 60°
320 Hz 240°
350 Hz 60°
350 Hz 240°
320 Hz 90°
320 Hz 270°
350 Hz 90°
350 Hz 270°
320 Hz 120°
320 Hz 300°
350 Hz 120°
350 Hz 300°
320 Hz 150°
320 Hz 330°
350 Hz 150°
350 Hz 330°

Appendix B.4 Flow Condition 4: Vr=0.5, Uinner=1.36 m/s

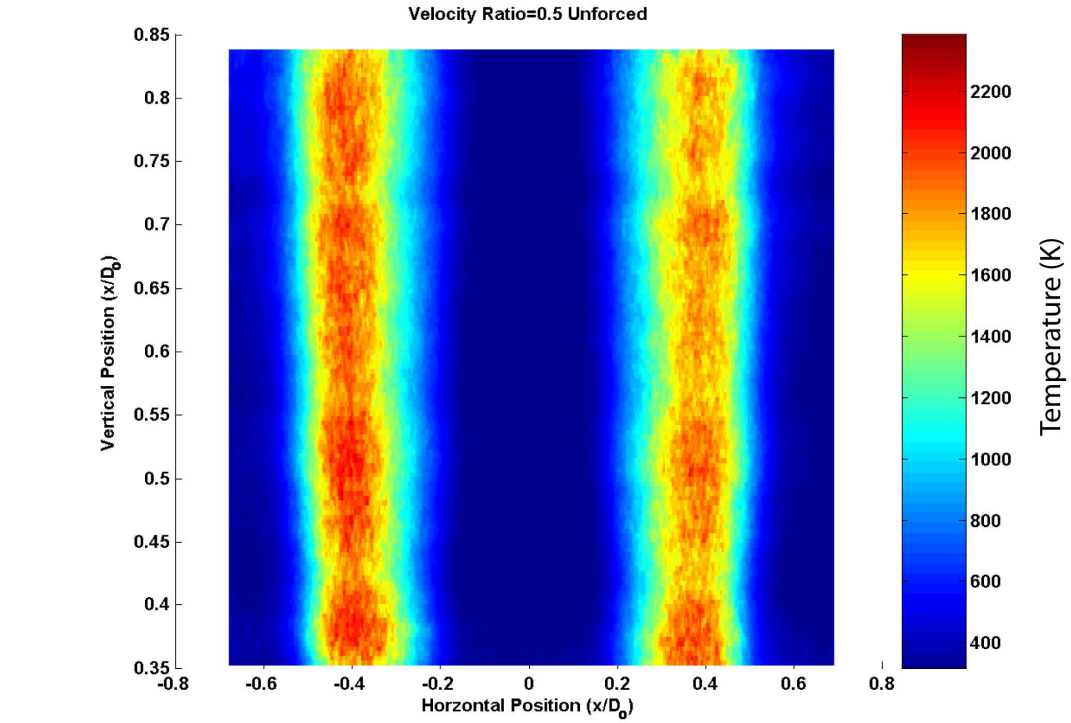

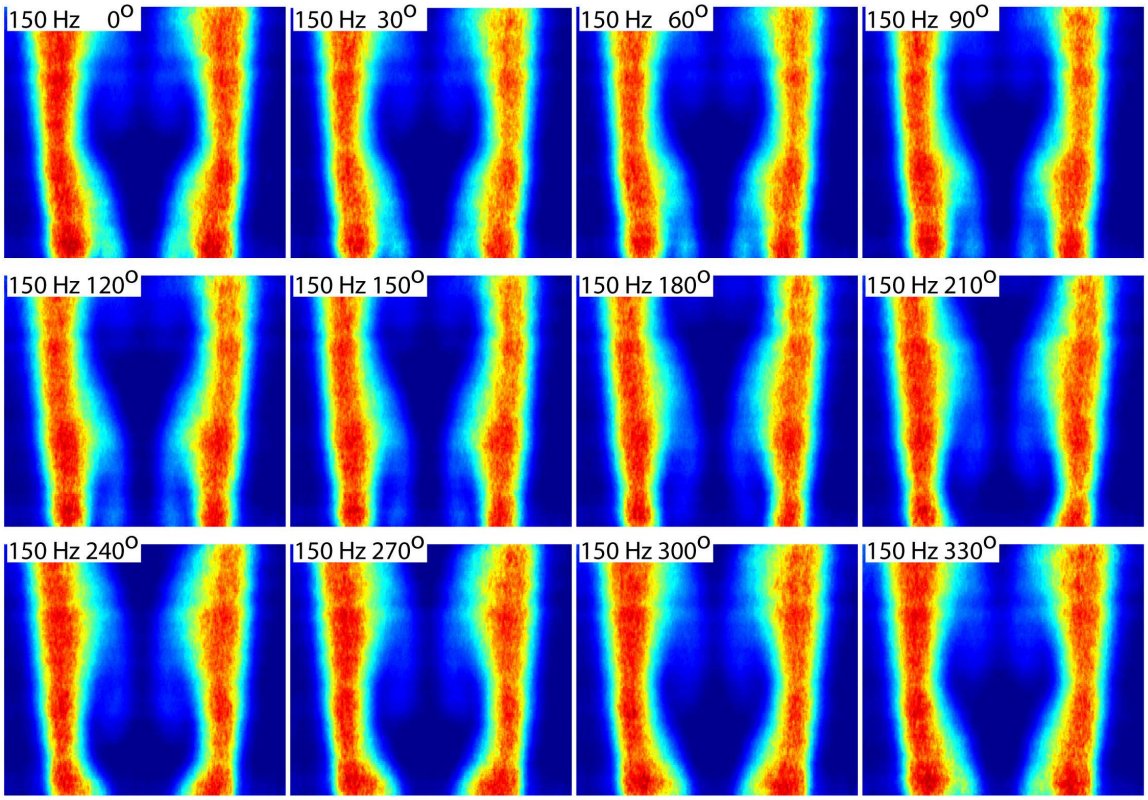

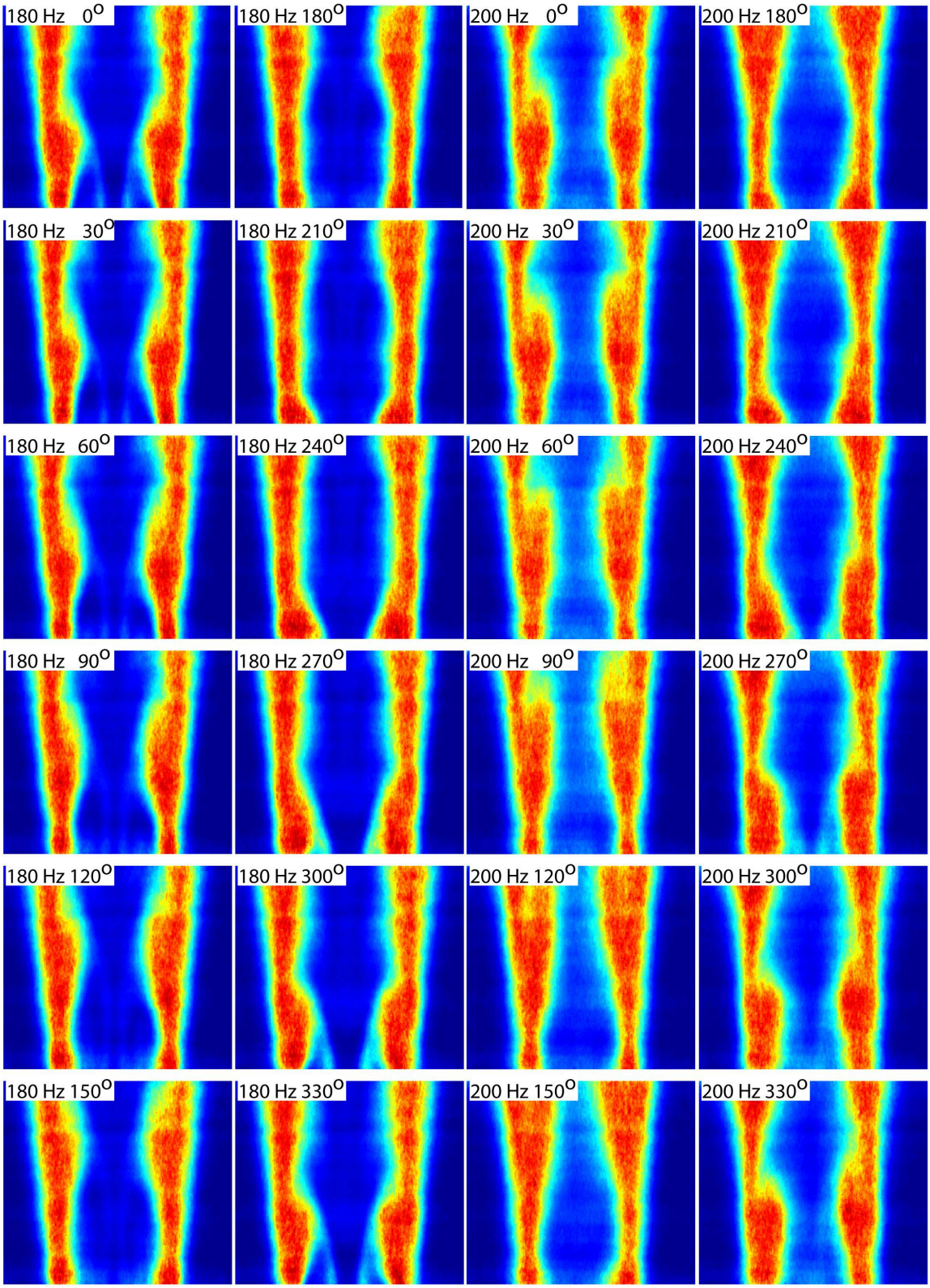
180 Hz 0°
180 Hz 180°
200 Hz 0°
200 Hz 180°
180 Hz 30°
180 Hz 210°
200 Hz 30°
200 Hz 210°
180 Hz 60°
180 Hz 240°
200 Hz 60°
200 Hz 240°
180 Hz 90°
180 Hz 270°
200 Hz 90°
200 Hz 270°
180 Hz 120°
180 Hz 300°
200 Hz 120°
200 Hz 300°
180 Hz 150°
180 Hz 330°
200 Hz 150°
200 Hz 330°

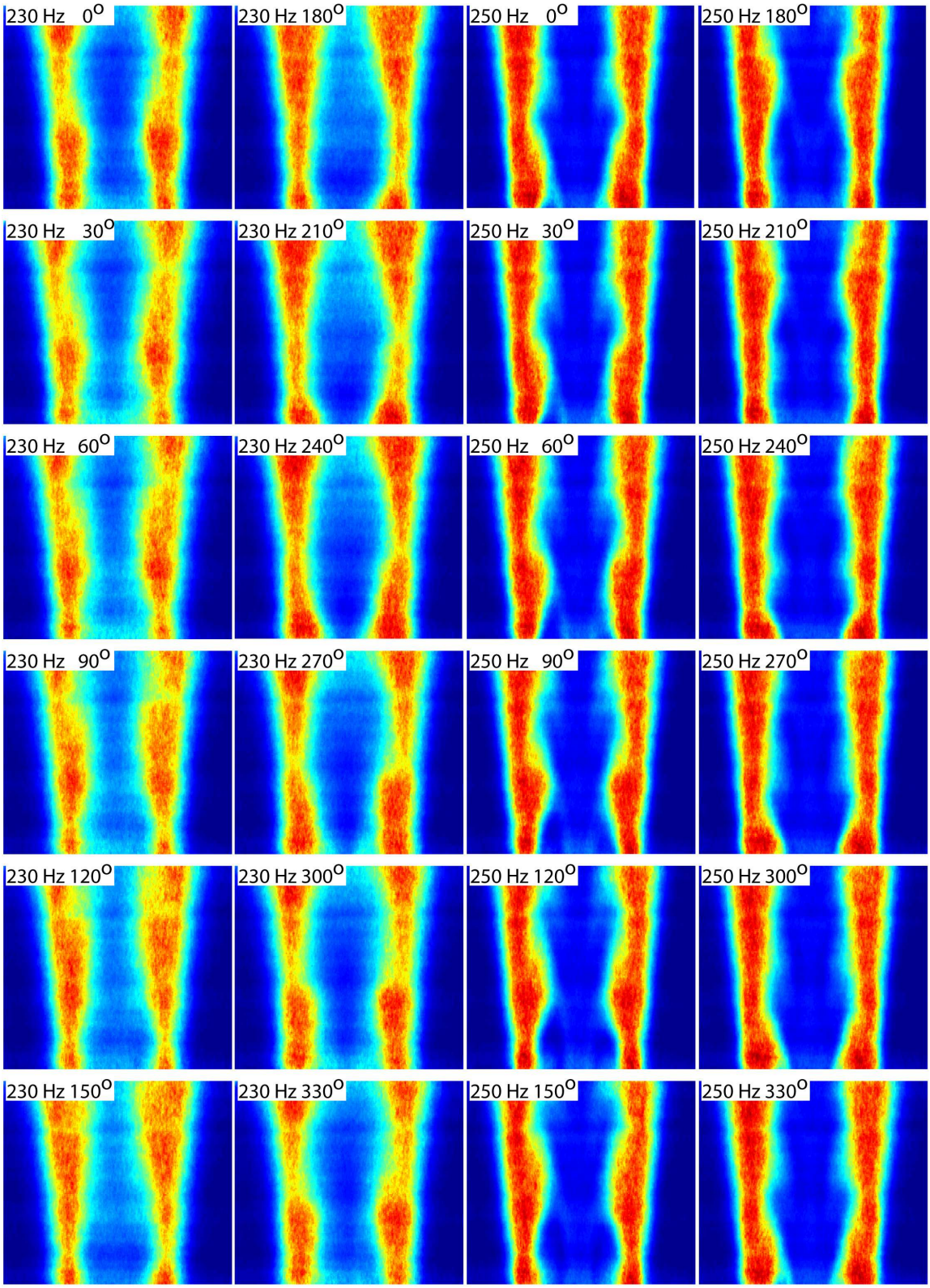
230 Hz 0°
230 Hz 180°
250 Hz 0°
250 Hz 180°
230 Hz 30°
230 Hz 210°
250 Hz 30°
250 Hz 210°
230 Hz 60°
230 Hz 240°
250 Hz 60°
250 Hz 240°
230 Hz 90°
230 Hz 270°
250 Hz 90°
250 Hz 270°
230 Hz 120°
230 Hz 300°
250 Hz 120°
250 Hz 300°
230 Hz 150°
230 Hz 330°
250 Hz 150°
250 Hz 330°

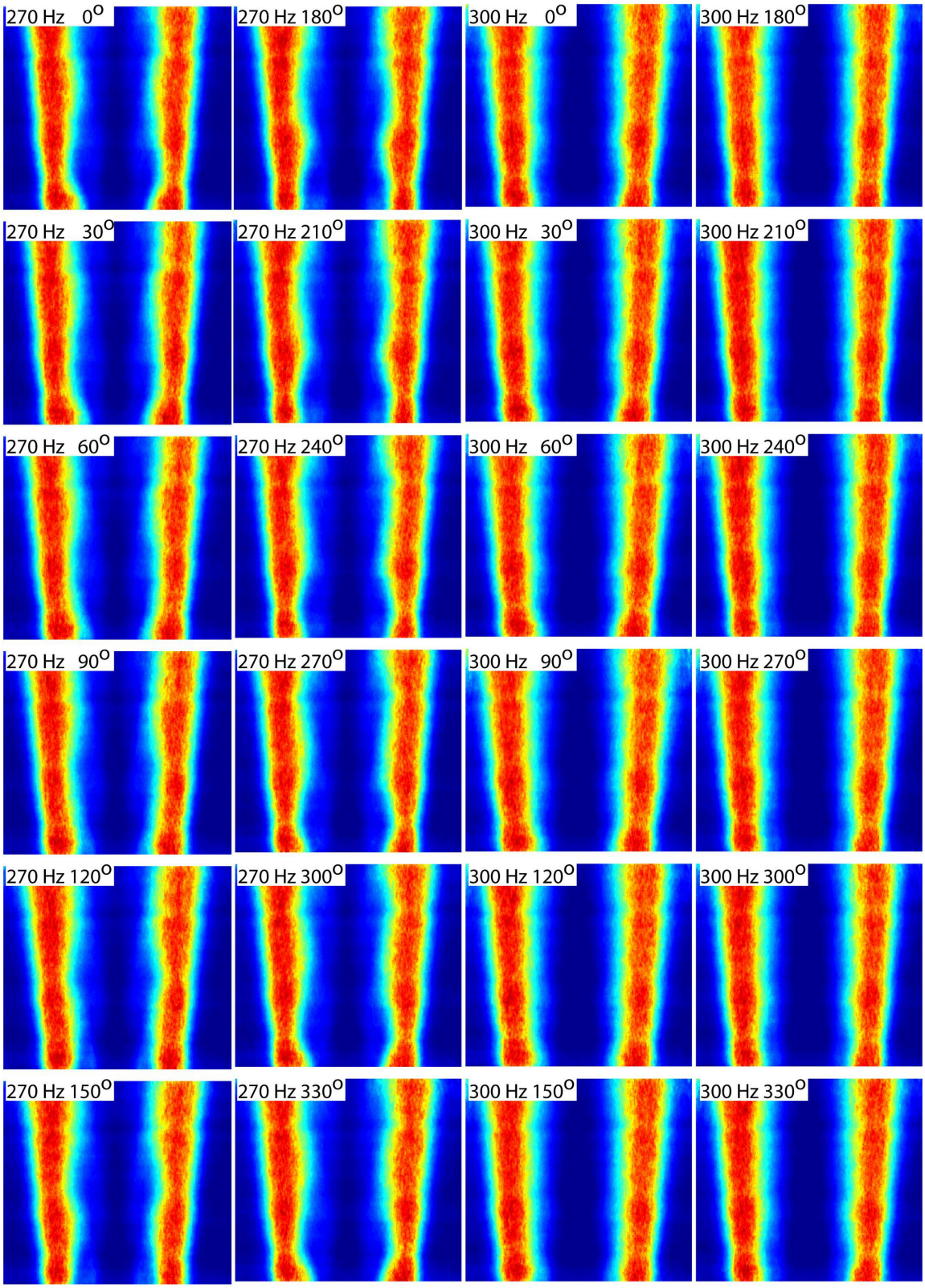
270 Hz 0°
270 Hz 180°
300 Hz 0°
300 Hz 180°
270 Hz 30°
270 Hz 210°
300 Hz 30°
300 Hz 210°
270 Hz 60°
270 Hz 240°
300 Hz 60°
300 Hz 240°
270 Hz 90°
270 Hz 270°
300 Hz 90°
300 Hz 270°
270 Hz 120°
270 Hz 300°
300 Hz 120°
300 Hz 300°
270 Hz 150°
270 Hz 330°
300 Hz 150°
300 Hz 330°

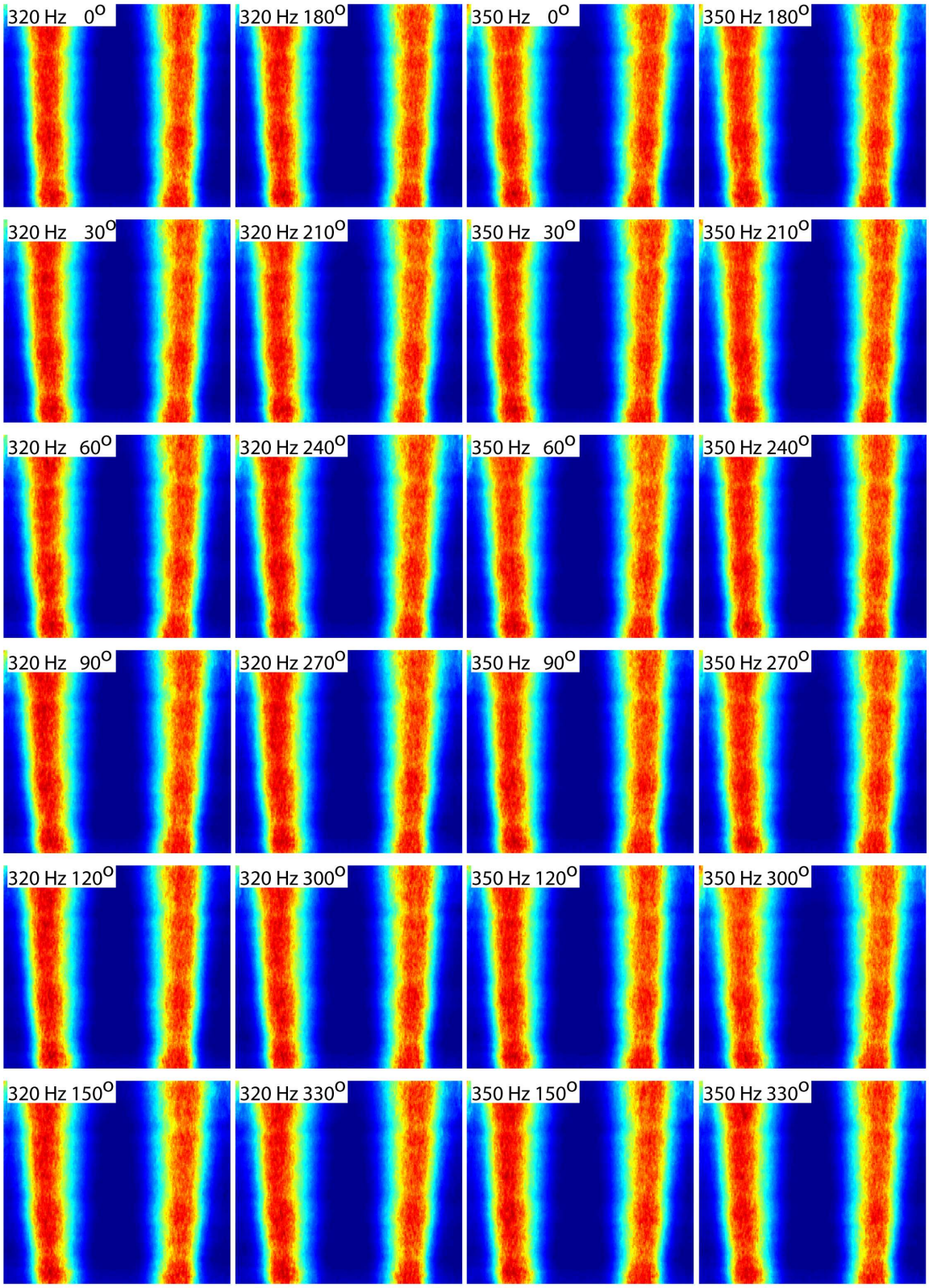
320 Hz 0°
320 Hz 180°
350 Hz 0°
350 Hz 180°
320 Hz 30°
320 Hz 210°
350 Hz 30°
350 Hz 210°
320 Hz 60°
320 Hz 240°
350 Hz 60°
350 Hz 240°
320 Hz 90°
320 Hz 270°
350 Hz 90°
350 Hz 270°
320 Hz 120°
320 Hz 300°
350 Hz 120°
350 Hz 300°
320 Hz 150°
320 Hz 330°
350 Hz 150°
350 Hz 330°

Appendix C- MathCad Code

Coflow Tube Geometry

$D_{inner} := 0.50in$ $D_{outter} := 1.00in$ $D_{between} := 0.75in$

$$A_{inner} := \pi \cdot \left(\frac{D_{inner}}{2} \right)^2 \qquad A_{outter} := \pi \cdot \left[\left(\frac{D_{outter}}{2} \right)^2 - \left(\frac{D_{between}}{2} \right)^2 \right]$$

Gas Properties H2 and CH4

$MW_{air} := 28.94 \frac{gm}{mole}$ $MW_{H2} := 2.00 \frac{gm}{mole}$ $MW_{CH4} := 16.00 \frac{gm}{mole}$ $T_{amb} := 300K$

$P_{amb} := 14.7psi$

$\gamma_{H2} := 1.41$ $\gamma_{CH4} := 1.31$ $\gamma_{air} := 1.40$

$R_{H2} := 4124 \frac{J}{kg \cdot K}$ $R_{CH4} := 518.3 \frac{J}{kg \cdot K}$ $R_{air} := 286.9 \frac{J}{kg \cdot K}$

$\rho amb_{H2} := 8.38 10^{-2} \frac{kg}{m^3}$ $\rho amb_{CH4} := 0.667 \frac{kg}{m^3}$ $\rho amb_{air} := 1.1614 \frac{kg}{m^3}$

$vel_{ratio} := 2$ Velocity Ratio air/fuel

Properties of Mixture

$$MW_{mix} := 0.62 MW_{H2} + 0.38 MW_{CH4}$$

$$\rho amb_{mix} := \left(\frac{MW_{mix}}{22.4 \frac{L}{mole}} \right) \cdot \frac{300K}{T_{amb}} \qquad \mu_{mix} := 1.1 \cdot 10^{-5} \frac{kg}{m \cdot s}$$

Oriface information

$D_{H2} := 0.007in$ $D_{CH4} := 0.010in$ $D_{air} := 0.020in$

$$A_{H2} := \pi \left(\frac{D_{H2}}{2} \right)^2 \qquad A_{CH4} := \pi \left(\frac{D_{CH4}}{2} \right)^2 \qquad A_{air} := \pi \left(\frac{D_{air}}{2} \right)^2$$

Isentropic Equation

$$mratio(Po, To, R, \gamma) := \begin{vmatrix} A \leftarrow \dfrac{Po}{\sqrt{To}} \\ B \leftarrow \sqrt{\dfrac{\gamma}{R}} \\ C \leftarrow \left(\dfrac{\gamma + 1}{2}\right)^{\frac{\gamma+1}{2\cdot(\gamma-1)}} \\ A \cdot B \cdot \left(C^{-1}\right) \end{vmatrix}$$

$$Po(\gamma, P_{amb}) := \begin{vmatrix} Z \leftarrow \left(\dfrac{2}{\gamma + 1}\right)^{\frac{\gamma}{\gamma-1}} \\ \dfrac{P_{amb}}{Z} \end{vmatrix}$$

Minimum Gauge Pressure

$$Pmin_{H2} := Po(\gamma_{H2}, P_{amb}) - P_{amb}$$

$$Pmin_{CH4} := Po(\gamma_{CH4}, P_{amb}) - P_{amb}$$

$$Pmin_{air} := Po(\gamma_{air}, P_{amb}) - P_{amb}$$

H2 Setting

$$Pg_{H2} := 20psi$$

$$Po_{H2} := Pg_{H2} + P_{amb}$$

$$mdot_{H2} := mratio(Po_{H2}, T_{amb}, R_{H2}, \gamma_{H2}) \cdot A_{H2}$$

At Nozzel

$$vdot_{H2} := \frac{mdot_{H2}}{\rho amb_{H2}}$$

$$vdot_{tot} := \frac{vdot_{H2}}{0.62}$$

$$vdot_{CH4} := vdot_{tot} \cdot 0.38$$

$$mdot_{CH4} := vdot_{CH4} \cdot \rho amb_{CH4}$$

$$vel_{exit} := \frac{vdot_{tot}}{A_{inner}}$$

$$Re_D := \frac{\left(vel_{exit} \cdot D_{inner} \cdot \rho amb_{mix}\right)}{\mu_{mix}}$$

CH4 and Air settings

$$Po_{gas}(mdot, A, To, \gamma, R) := \left| \begin{array}{l} Z \leftarrow \frac{mdot}{A} \\ Y \leftarrow \sqrt{\frac{\gamma}{R}} \\ X \leftarrow \left(\frac{\gamma + 1}{2}\right)^{\frac{\gamma+1}{2\cdot(\gamma-1)}} \\ \frac{Z \cdot X \cdot \sqrt{To}}{Y} \end{array} \right.$$

$$Po_{CH4} := Po_{gas}(mdot_{CH4}, A_{CH4}, T_{amb}, \gamma_{CH4}, R_{CH4})$$

$$Pg_{CH4} := Po_{CH4} - P_{amb} \qquad vel_{air} := vel_{exit} \cdot vel_{ratio}$$

$$vdot_{air} := vel_{air} \cdot A_{outter}$$

$$mdot_{air} := \frac{(vdot_{air} \cdot \rho amb_{air})}{2} \qquad \text{2 air inlets}$$

$$Po_{air} := Po_{gas}(mdot_{air}, A_{air}, T_{amb}, \gamma_{air}, R_{air})$$

$$Pg_{air} := Po_{air} - P_{amb}$$

Power Output

$$QM_{H2} := 242000 \frac{joule}{mole} \qquad Heat_{H2} := \frac{QM_{H2}}{MW_{H2}}$$

$$QM_{CH4} := 882000 \frac{J}{mole} \qquad Heat_{CH4} := \frac{QM_{CH4}}{MW_{CH4}}$$

$$Power := mdot_{H2} \cdot Heat_{H2} + mdot_{CH4} \cdot Heat_{CH4}$$

Values

$mdot_{H2} = 3.666 \times 10^{-6} \frac{kg}{s}$ $mdot_{CH4} = 1.788 \times 10^{-5} \frac{kg}{s}$

$vdot_{H2} = 4.374 \times 10^{-5} \frac{m^3}{s}$ $vdot_{tot} = 7.056 \times 10^{-5} \frac{m^3}{s}$

$Re_D = 210.14$ $vel_{exit} = 0.557 \frac{m}{s}$

$mdot_{air} = 1.434 \times 10^{-4} \frac{kg}{s}$

$vdot_{CH4} = 2.681 \times 10^{-5} \frac{m^3}{s}$

$vel_{air} = 1.114 \frac{m}{s}$

Gauge Pressures

$Pmin_{H2} = 13.215 psi$ $Pmin_{CH4} = 12.326 psi$ $Pmin_{air} = 13.126 psi$

$Pg_{H2} = 20 psi$ $Pg_{CH4} = 15.468 psi$ $Pg_{air} = 29.267 psi$

Heat

$Heat_{CH4} = 5.513 \times 10^{7} \frac{J}{kg}$ $Heat_{H2} = 1.21 \times 10^{8} \frac{J}{kg}$ $Power = 1.429 kW$

Appendix D-Matlab Code

```
% This code averages the calibration images and generates the
% temperature maps for each image.  Then the code averages the
% temperature maps to generate the standard error image for each phase
% of each frequency.  This code specifically processes flow condition
% #1 and #2.  The code for #3 and #4 are similar, just with a different
% naming scheme.

clear all
close all
clc
format long

N2=zeros(131,351); %sets up the N2 matrix
He=N2; %setting up the He matrix
imlim=[230,360,125,475];

for i=1:50;
        if i<10
            C='000';
        else
            C='00' ;
        end

I=imread(strcat('E:\Eddys_data\022205\ambient\ambient_',C,num2str(i),'.
bmp')); %reads the file
    I=im2double(I); %Converts the image from an indexed
                    %picture to intensity map
    I=I(imlim(1):imlim(2),imlim(3):imlim(4));
    %Dust filtering
    [numb Int]=imhist(I); %Making a histogram distribution
    [numb Y]=max(numb(20:225,1)); %Finding the median of the histogram
                                  %distribution while ignoring the points
                                   %with intensities in the first and
                                 %last few histogram bins
    N2median=Int(Y+19); %The median of the intensity distribution
    I=I.*(I<.70)+N2median*(I>=.70); %filtering signals over .70
                         %assuming they are dust)and replacing them with
                         %the median from the intensity distribution
    N2=N2+I; %adding the images together

I2=imread(strcat('E:\Eddys_data\022205\helium\helium_',C,num2str(i),'.b
mp'));
    I2=im2double(I2);
    I2=I2(imlim(1):imlim(2),imlim(3):imlim(4));
    %Dust filtering
    I2=I2.*(I2<.70)+N2median*(I2>=.70);
       %filtering signals over .70 (assuming they are dust)and
       %replacing them with the median from the ambient intensity
       %distribution.  This
       %also assumes dust is only present only in low temperature areas
   He=He+I2; %adding the images together

end
```

```
N2_10=N2/50;
He_10=He/50;

Idiff=N2_10-He_10;
Do=1;
xx=linspace(-.679,.688,size(He_10,2));
xx=xx/Do;
yy=linspace(.353,.838,size(He_10,1));
yy=yy/Do;
%
freq=[150,180,200,230,250,270,300,320,350];
phase=[0,30,60,90,120,150,180,210,240,270,300,330];
velocity=[1,2];

%  freq=[250];
%  phase=[300];
%  velocity=[2];
 velocityA=[1.36,2.16];

for i=1:length(velocity);
    for l=1:50;
        if l<10;
            C='000';
        else
            C='00';
        end
        %unforced images

I=imread(strcat('E:\Eddys_data\bump_data\velocity\velocity_',...
num2str(velocity(i)),'\unforced\unforced_',C,num2str(l),'.bmp'));
        I=im2double(I);
        I=I(imlim(1):imlim(2),imlim(3):imlim(4));
        I=I.*(I<.70)+N2_10.*(I>=.70);
        Tamb=300; %assuming room Temperature

        Idel=I-He_10;
        Idelta=Idel.*(Idel>0)+.00392156863.*(Idel<.00392156863);
                %Replacing intensitys that lead to a negative number
        T=Tamb*((Idiff)./(Idelta));
        T=T.*(T<=2350)+2350.*(T>2350);
                %Limiting the temperature
        Tbig(:,:,l)=T;
    end

%Temperature map

        Tmean=mean(Tbig,3);
        mojo2=flipud(Tmean);
        surface(xx,yy,mojo2,...
            'FaceColor','texturemap',...
            'EdgeColor','none',...
            'CDataMapping','scaled');
        caxis([300 2400])
       set(gca,'FontWeight','Bold')
       xlabel('Horzontal Position (x/D_o)')
       ylabel('Vertical Position (x/D_o)')
```

```
       title(['u_i_n_n_e_r=',num2str(velocityA(i)),' m/s',...
          ' Unforced'])
       colorbar('FontWeight','Bold')

saveas(gcf,strcat('E:\Eddys_data\tiff_data\velocity\unforced_vel_',...
            num2str(velocity(i))),'tif')
       close

%error map

       stdD=(std(Tbig,1,3))/sqrt(50);
       mojo3=flipud(stdD);

       surface(xx,yy,mojo3,...
            'FaceColor','texturemap',...
            'EdgeColor','none',...
            'CDataMapping','scaled');
       caxis([0 100])
       set(gca,'FontWeight','Bold')
       xlabel('Horzontal Position (x/D_o)')
       ylabel('Vertical Position (x/D_o)')
       title(['u_i_n_n_e_r=',num2str(velocityA(i)),' m/s',...
          ' Unforced Standard Error'])
       colorbar('FontWeight','Bold')

saveas(gcf,strcat('E:\Eddys_data\tiff_data\velocity\unforced_vel_',...
          num2str(velocity(i)),'_std'),'tif')
close

    for j=1:length(freq);
        for k=1:length(phase);
            for l=1:50;
                if l<10;
                    C='000';
                else
                    C='00';
                end
                %forced images

I=imread(strcat('E:\Eddys_data\bump_data\velocity\velocity_',...
num2str(velocity(i)),'\',num2str(freq(j)),'\',num2str(freq(j)),...
'hz_1_1_',num2str(velocity(i)),'_',num2str(phase(k)),'_',C,...
num2str(l),'.bmp'));
                I=im2double(I);
                I=I(imlim(1):imlim(2),imlim(3):imlim(4));
                I=I.*(I<.70)+N2_10.*(I>=.70);
                Tamb=300; %assuming room Temperature

                Idel=I-He_10;

Idelta=Idel.*(Idel>0)+.00392156863.*(Idel<.00392156863);

                T=Tamb*((Idiff)./(Idelta));
                T=T.*(T<=2400)+2400.*(T>2400);
                Tbig(:,:,l)=T;
            end
```

```
%Temperature map

            Tmean=mean(Tbig,3);
            mojo2=flipud(Tmean);
            surface(xx,yy,mojo2,...
                'FaceColor','texturemap',...
                'EdgeColor','none',...
                'CDataMapping','scaled');
            caxis([300 2400])
            set(gca,'FontWeight','Bold')
            xlabel('Horzontal Position (x/D_o)')
            ylabel('Vertical Position (x/D_o)')
            title(['u_i_n_n_e_r=',num2str(velocityA(i)),' m/s',...
                ' Frequency= ',num2str(freq(j)),' Hz',' ...
                  phase= ',num2str(phase(k)),'^o']),...
                  colorbar('FontWeight','Bold')

saveas(gcf,strcat('E:\Eddys_data\tiff_data\velocity\vel_',...

num2str(velocity(i)),'_',num2str(freq(j)),'Hz_',num2str(phase(k))),'tif
')
close

%error map

            stdD=(std(Tbig,1,3))/sqrt(50);
            mojo3=flipud(stdD);
            surface(xx,yy,mojo3,...
                'FaceColor','texturemap',...
                'EdgeColor','none',...
                'CDataMapping','scaled');
            caxis([0 100])
            set(gca,'FontWeight','Bold')
            xlabel('Horzontal Position (x/D_o)')
            ylabel('Vertical Position (x/D_o)')
            title(['u_i_n_n_e_r=',num2str(velocityA(i)), 'm/s',...
                ' Frequency= ',num2str(freq(j)),' Hz',' phase=
',num2str(phase(k)),'^o Standard Error'])
            colorbar('FontWeight','Bold')

saveas(gcf,strcat('E:\Eddys_data\tiff_data\velocity\vel_',...
num2str(velocity(i)),'_',num2str(freq(j)),'Hz_',...
num2str(phase(k)),'_std'),'tif')
            close
        end
    end
end

disp('done with this')
```

Appendix E: Pixel Replacement Percentages

Flow Condition #1

Frequency (Hz) \ Phase	0	30	60	90	120	150	180	210	240	270	300	330
150	3.8%	4.6%	4.6%	4.7%	3.6%	4.3%	5.2%	4.7%	5.4%	4.9%	5.4%	5.0%
180	11.7%	13.4%	15.4%	17.2%	17.4%	18.2%	18.4%	18.4%	17.3%	16.9%	17.0%	17.3%
200	2.3%	3.4%	7.6%	7.2%	8.8%	7.9%	8.9%	8.8%	9.0%	9.1%	10.5%	9.6%
230	23.8%	31.4%	34.7%	35.5%	37.4%	35.9%	33.1%	32.4%	34.6%	37.0%	42.7%	46.2%
250	5.7%	21.5%	21.4%	23.0%	24.3%	20.7%	20.0%	17.7%	20.2%	22.9%	26.2%	26.9%
270	12.0%	24.4%	25.1%	25.7%	27.3%	26.1%	23.3%	24.5%	29.0%	32.7%	34.2%	35.6%
300	10.9%	15.7%	22.8%	21.7%	22.2%	21.6%	21.8%	21.5%	22.2%	23.6%	24.5%	25.6%
320	13.6%	14.2%	13.2%	12.8%	12.4%	2.6%	5.9%	9.1%	10.7%	11.5%	12.3%	13.0%
350	3.2%	7.8%	9.4%	10.2%	10.4%	11.0%	11.0%	11.5%	11.2%	11.6%	11.8%	11.7%

Flow Condition #2

Frequency (Hz) \ Phase	0	30	60	90	120	150	180	210	240	270	300	330
150	1.4%	0.7%	0.7%	0.6%	0.5%	0.5%	0.6%	0.8%	1.0%	1.0%	1.0%	1.1%
180	2.1%	2.2%	1.9%	2.1%	2.2%	2.2%	2.1%	2.0%	2.2%	2.4%	2.4%	3.3%
200	3.9%	3.3%	3.7%	4.3%	4.6%	3.7%	4.0%	3.6%	3.9%	4.5%	6.3%	6.6%
230	6.3%	5.8%	4.5%	5.1%	5.5%	6.4%	5.8%	5.1%	4.9%	5.8%	6.3%	7.6%
250	7.6%	8.6%	9.3%	10.6%	11.7%	12.0%	11.6%	11.6%	11.3%	9.4%	9.3%	11.8%
270	8.8%	8.4%	8.1%	7.5%	6.8%	6.6%	7.1%	8.1%	8.8%	9.3%	9.7%	10.1%
300	7.5%	7.7%	7.7%	7.9%	7.8%	7.8%	8.0%	8.0%	7.8%	7.7%	8.0%	8.0%
320	8.5%	8.6%	8.8%	9.0%	9.1%	8.7%	8.8%	9.3%	9.6%	9.0%	9.2%	9.0%
350	9.4%	9.1%	9.7%	9.9%	9.5%	10.0%	9.9%	9.9%	10.0%	10.2%	10.0%	10.3%

Flow Condition #3

Frequency (Hz)	Phase											
	0	30	60	90	120	150	180	210	240	270	300	330
150	1.4%	1.8%	1.8%	1.1%	1.3%	1.3%	1.3%	1.5%	1.5%	1.6%	1.8%	1.9%
180	2.6%	3.5%	3.5%	4.0%	3.9%	4.0%	3.4%	3.9%	4.0%	4.3%	4.7%	4.9%
200	1.4%	1.4%	1.5%	1.8%	2.1%	2.4%	2.6%	2.8%	3.3%	3.7%	3.8%	4.3%
230	3.3%	3.3%	3.6%	4.1%	4.4%	4.0%	4.1%	5.1%	4.6%	5.9%	6.8%	6.4%
250	5.3%	4.8%	5.5%	6.7%	6.4%	5.1%	5.7%	6.8%	7.2%	8.7%	8.7%	7.9%
270	3.6%	3.3%	3.4%	3.7%	4.4%	4.6%	4.1%	4.2%	4.7%	5.5%	5.3%	6.8%
300	3.7%	5.5%	6.3%	7.1%	7.2%	7.5%	7.9%	8.6%	9.4%	9.7%	10.5%	11.5%
320	2.1%	1.9%	2.0%	2.2%	2.5%	2.6%	2.7%	2.8%	2.7%	3.1%	3.1%	3.3%
350	3.0%	4.4%	1.4%	2.3%	2.2%	2.4%	2.5%	2.2%	2.3%	2.3%	2.0%	2.3%

Flow Condition #4

Frequency (Hz)	Phase											
	0	30	60	90	120	150	180	210	240	270	300	330
150	4.0%	4.0%	4.3%	4.8%	4.2%	4.4%	4.6%	4.8%	5.2%	5.6%	6.1%	6.1%
180	5.2%	5.6%	5.3%	5.4%	5.0%	5.6%	5.9%	6.2%	6.0%	6.3%	6.1%	6.0%
200	5.5%	5.4%	5.5%	6.4%	6.2%	6.2%	6.6%	6.5%	6.4%	6.4%	6.5%	5.3%
230	4.0%	4.0%	3.8%	4.0%	4.2%	4.6%	5.1%	5.7%	4.9%	4.7%	4.3%	4.3%
250	6.1%	6.4%	5.8%	5.7%	5.5%	5.4%	5.8%	6.2%	6.1%	6.4%	6.8%	6.6%
270	6.1%	6.2%	6.3%	6.7%	6.3%	6.5%	6.5%	6.0%	6.2%	6.4%	6.5%	6.1%
300	7.0%	7.0%	7.6%	7.1%	7.2%	6.9%	7.6%	7.4%	7.1%	7.0%	7.2%	7.4%
320	7.5%	7.2%	7.6%	6.9%	7.5%	7.2%	7.3%	7.9%	7.7%	7.3%	7.7%	7.9%
350	7.8%	7.4%	7.3%	7.5%	7.9%	7.8%	7.7%	7.1%	8.0%	7.3%	7.4%	7.1%

References

[1] McManus, K. R., Poinsot, T., and Candel, S. M., "A review of active control of combustion instabilities," *Prog. Energy Combust. Sci.*, vol. 19, pp. 1-29, 1993.

[2] Gutmark, E., Parr, T. P., Hanson-Parr, D. M., and Schadow, K. C., "On the role of large and small-scale structures in combustion control," *Combust. Sci. Technol.*, vol. 66, pp. 107-126, 1989.

[3] Schadow, K. C., Gutmark, E., Wilson, K. J., Parr, D. M., Mahan, V. A., and Ferrell, G. B., "Effect of shear-flow dynamics in combustion processes," *Combust. Sci. Technol.*, vol. 54, pp. 103-116, 1987.

[4] Pang, B., Cipolla, S., and Yu, K., "Oscillatory heat release associated with periodic vortices in dump combustor," presented at 41st Aerospace Sciences Meeting and Exhibit, Reno, Nevada, 2003.

[5] Albers, B. W. and Agrawal, A. K., "Schlieren analysis of an oscillating gas-jet diffusion flame," *Combust. Flame*, vol. 119, pp. 84-94, 1999.

[6] Dunn-Rankin, D. and Weinberg, F., "Location of the schlieren image in premixed flames: Axially symmetrical refractive index fields," *Combust. Flame*, vol. 113, pp. 303-311, 1998.

[7] Davis, M. R. and Rerkshanandana, P., "Schlieren measurement of turbulent structure in a diffusion flame," *Exp. Therm. Fluid Sci.*, vol. 6, pp. 402-416, 1993.

[8] Ishino, Y., Yamaguchi, S., and Ohiwa, N., "An experimental study on vortex-flame interaction of a spark-ignited flame with coherent structure in a plane premixed shear flow," *Energy*, vol. 30, pp. 323-336, 2005.

[9] Yu, K., "Combustion enhancement of a premixed flame by acoustic forcing with emphasis on role of large-scale vortical structures," presented at 29th Aerospace Sciences Meeting, Reno, Nevada, 1991.

[10] Grumer, J., "Schlieren and direct photographic studies of the turbulent flame structure," *Jet Propulsion*, vol. 26, pp. 481-482, 1956.

[11] McManus, K. R., Vandsburger, U., and Bowman, C. T., "Combustor performance enhancement through direct shear-layer excitation," *Combust. Flame*, vol. 82, pp. 75-92, 1990.

[12] Bernier, D., Lacas, F., and Candel, S., "Instability mechanisms in a premixed prevaporized combustor," *J. Propul. Power*, vol. 20, pp. 648-656, 2004.

[13] Pun, W., Palm, S. L., and Culick, F. E. C., "Combustion dynamics of an acoustically forced flame," *Combust. Sci. Technol.*, vol. 175, pp. 499-521, 2003.

[14] Hardalupas, Y. and Orain, M., "Local measurements of the time-dependent heat release rate and equivalence ratio using chemiluminescent emission from a flame," *Combust. Flame*, vol. 139, pp. 188-207, 2004.

[15] Kojima, J., Ikeda, Y., and Nakajima, T., "Basic aspects of OH(A), CH(A), and C-2(d) chemiluminescence in the reaction zone of laminar methane-air premixed flames," *Combust. Flame*, vol. 140, pp. 34-45, 2005.

[16] Köhse-Hoinghaus, K. and Jeffries, J. B., *Applied Combustion Diagnostics*. New York: Taylor & Francis, 2002.

[17] Zhao, F. Q. and Hiroyasu, H., "The applications of laser Rayleigh-scattering to combustion diagnostics," *Prog. Energy Combust. Sci.*, vol. 19, pp. 447-485, 1993.

[18] Winant, C. D. and Browand, F. K., "Vortex pairing - mechanism of turbulent mixing layer growth at moderate Reynolds-number," *J. Fluid Mech.*, vol. 63, pp. 237-255, 1974.

[19] Meyer, T. R., Dutton, J. C., and Lucht, R. P., "Vortex interaction and mixing in a driven gaseous axisymmetric jet," *Phys. Fluids*, vol. 11, pp. 3401-3415, 1999.

[20] Samaniego, J.-M. and Mantel, T., "Fundamental mechanisms in premixed turbulent flame propagation via flame-vortex interactions: Part I: Experiment," *Combust. Flame*, vol. 118, pp. 537-556, 1999.

[21] Mueller, C. J., Driscoll, J. F., Reuss, D. L., Drake, M. C., and Rosalik, M. E., "Vorticity generation and attenuation as vortices convect through a premixed flame," *Combust. Flame*, vol. 112, pp. 342-358, 1998.

[22] Bai, T., Cheng, X. C., Daniel, B. R., Jagoda, J. I., and Zinn, B. T., "Vortex shedding and periodic combustion processes in a Rijke type pulse combustor," *Combust. Sci. Technol.*, vol. 94, pp. 245-258, 1993.

[23] You, Y. H., Lee, D. K., and Shin, H. D., "Visual investigation of a vortex ring interacting with a nonpremixed flame," *Combust. Sci. Technol.*, vol. 139, pp. 365-383, 1998.

[24] Louch, D. S. and Bray, K. N. C., "Vorticity in unsteady premixed flames: Vortex pair-premixed flame interactions under imposed body forces and various degrees of heat release and laminar flame thickness," *Combust. Flame*, vol. 125, pp. 1279-1309, 2001.

[25] Jackson, T. L., Macaraeg, M. G., and Hussaini, M. Y., "The role of acoustics in flame vortex interactions," *J. Fluid Mech.*, vol. 254, pp. 579-603, 1993.

[26] Dhanak, M. R., Dowling, A. P., and Si, C., "Coherent vortex model for surface pressure fluctuations induced by the wall region of a turbulent boundary layer," *Phys. Fluids*, vol. 9, pp. 2716-2731, 1997.

[27] Matveev, K. I. and Culick, F. E. C., "A model for combustion instability involving vortex shedding," *Combust. Sci. Technol.*, vol. 175, pp. 1059-1083, 2003.

[28] Najm, H. N., Knio, O. M., Paul, P. H., and Wyckoff, P. S., "Response of stoichiometric and rich premixed methane-air flames to unsteady strain rate and curvature," *Combust. Theory Model.*, vol. 3, pp. 709-726, 1999.

[29] Renard, P. H., Thevenin, D., Rolon, J. C., and Candel, S., "Dynamics of flame/vortex interactions," *Prog. Energy Combust. Sci.*, vol. 26, pp. 225-282, 2000.

[30] Culick, F., Heitor, M. V., and Whitelaw, J. H. E., *Unsteady Combustion*. Norwell: Kluwer Academic Publishers, 1996.

[31] Lieuwen, T., "Theoretical investigation of unsteady flow interactions with a premixed planar flame," *J. Fluid Mech.*, vol. 435, pp. 289-303, 2001.

[32] Fleifil, M., Annaswamy, A. M., Ghoneim, Z. A., and Ghoniem, A. F., "Response of a laminar premixed flame to flow oscillations: A kinematic model and thermoacoustic instability results," *Combustion and Flame*, vol. 106, pp. 487-510, 1996.

[33] Dowling, A. P., "The calculation of thermoacoustic oscillations," *J. Sound Vibr.*, vol. 180, pp. 557-581, 1995.

[34] Dowling, A. P., "Nonlinear self-excited oscillations of a ducted flame," *J. Fluid Mech.*, vol. 346, pp. 271-290, 1997.

[35] Lieuwen, T., "Modeling premixed combustion-acoustic wave interactions: A review," *J. Propul. Power*, vol. 19, pp. 765-781, 2003.

[36] Schuller, T., Durox, D., and Candel, S., "Self-induced combustion oscillations of laminar premixed flames stabilized on annular burners," *Combust. Flame*, vol. 135, pp. 525-537, 2003.

[37] Eckbreth, A. C., *Laser Diagnostics for Combustion Temperature and Species*, vol. 3, 2 ed. Amsterdam: Gordon and Breach Publishers, 1996.

[38] Miles, R. B., Lempert, W. R., and Forkey, J. N., "Laser Rayleigh scattering," *Meas. Sci. Technol.*, vol. 12, pp. R33-R51, 2001.

[39] Gardiner, W. C., Hidaka, Y., and Tanzawa, T., "Refractivity of combustion gases," *Combust. Flame*, vol. 40, pp. 213-219, 1981.

[40] Espey, C., Dec, J. E., Litzinger, T. A., and Santavicca, D. A., "Planar laser Rayleigh scattering for quantitative vapor-fuel imaging in a diesel jet," *Combust. Flame*, vol. 109, pp. 65-86, 1997.

[41] Dibble, R. W. and Hollenbach, R. E., "Laser Rayleigh thermometry in turbulent flames," *Proc. Combust. Symp. Vol. 18*, pp. 1489-1499, 1981.

[42] Masri, A. R., Dibble, R. W., and Barlow, R. S., "The structure of turbulent nonpremixed flames revealed by Raman-Rayleigh-LIF measurements," *Prog. Energy Combust. Sci.*, vol. 22, pp. 307-362, 1996.

[43] Orth, A., Sick, V., Wolfrum, J., Maly, R. R., and Zahn, M., "Simultaneous 2D single-shot imaging of OH concentrations and temperature field in an SI engine simulator," *Proc. Combust. Symp. Vol. 25*, pp. 143-150, 1994.

[44] Shirinzadeh, B., Hillard, M. E., Balla, R. J., Waitz, I. A., Anders, J. B., and Exton, R. J., "Planar Rayleigh-scattering results in helium air mixing experiments in a Mach-6 wind-tunnel," *Appl. Optics*, vol. 31, pp. 6529-6534, 1992.

[45] Gruber, M. R., Nejad, A. S., Chen, T. H., and Dutton, J. C., "Transverse injection from circular and elliptic nozzles into a supersonic crossflow," *J. Propul. Power*, vol. 16, pp. 449-457, 2000.

[46] Long, M. B., Levin, P. S., and Fourguette, D. C., "Simultaneous two-dimensional mapping of species concentration and temperature in turbulent flames," *Opt. Lett.*, vol. 10, pp. 267-269, 1985.

[47] Bergmann, V., Meier, W., Wolff, D., and Stricker, W., "Application of spontaneous Raman and Rayleigh scattering and 2D LIF for the characterization of a turbulent CH4/H-2/N-2 jet diffusion flame," *Appl. Phys. B-Lasers Opt.*, vol. 66, pp. 489-502, 1998.

[48] Su, L. K. and Clemens, N. T., "Planar measurements of the full three-dimensional scalar dissipation rate in gas-phase turbulent flows," *Exp. Fluids*, vol. 27, pp. 507-521, 1999.

[49] Everest, D. A., Driscoll, J. F., Dahm, W. J. A., and Feikema, D. A., "Images of the 2-Dimensional field and temperature-gradients to quantify mixing rates within a non-premixed turbulent jet flame," *Combust. Flame*, vol. 101, pp. 58-68, 1995.

[50] Böckle, S., Kazenwadel, J., Kunzelmann, T., and Schulz, C., "Laser-diagnostic multi-species imaging in strongly swirling natural gas flames," *Appl. Phys. B-Lasers Opt.*, vol. 71, pp. 741-746, 2000.

[51] Durox, D., Baillot, F., Searby, G., and Boyer, L., "On the shape of flames under strong acoustic forcing: a mean flow controlled by an oscillating flow," *J. Fluid Mech.*, vol. 350, pp. 295-310, 1997.

[52] Glassman, I., *Combustion*, 3 ed. New York: Academic Press, 1996.

[53] *Maryland Weather*. Updated hourly. Baltimore Sun. 1 April 2005 <http://www.marylandweather.com/news/weather/site/>